

ACID SUSPENDS THE CIRCADIAN CLOCK IN HYPOXIA THROUGH INHIBITION OF MTOR

Zandra E. Walton

A DISSERTATION

in

Cell and Molecular Biology

Presented to the Faculties of the University of Pennsylvania

in

Partial Fulfillment of the Requirements for the

Degree of Doctor of Philosophy

2018

Supervisor of Dissertation

---

Chi Van Dang, MD-PhD

Professor, The Wistar Institute  
Adjunct Professor of Medicine, Perelman School of Medicine

Graduate Group Chairperson

---

Daniel Kessler, PhD, Associate Professor of Cell and Developmental Biology, Perelman School of Medicine

Dissertation Committee

Todd Ridky, MD-PhD, Assistant Professor of Dermatology, Perelman School of Medicine

Celeste Simon, PhD, Professor of Cell and Developmental Biology, Perelman School of Medicine; Director, Abramson Family Cancer Research Institute

Brian Keith, PhD, Dean of Biomedical Studies, The Wistar Institute

John Hogenesch, PhD, Professor of Pediatrics, Cincinnati Children's Medical Center

ACID SUSPENDS THE CIRCADIAN CLOCK IN HYPOXIA THROUGH INHIBITION OF MTOR  
COPYRIGHT

2018

Zandra Elene Walton

This work is licensed under the  
Creative Commons Attribution-  
NonCommercial-ShareAlike 3.0  
License

To view a copy of this license, visit

<https://creativecommons.org/licenses/by-nc-sa/3.0/us/>

Portions of this work have been accepted (Walton et al., 2018b) or may be submitted for consideration for journal publication so do or may subsequently appear in part or in full in publications elsewhere.

## ACKNOWLEDGMENTS

This work was supported by NIH/NCI grants F30CA200347 (ZEW), T32CA9140-39 (ZEW), R01CA051497 (CVD), and R01CA57341 (CVD) and the Patel Scholar Award (ZEW).

For the RNA-sequencing experiment, the Next Generation Sequencing Core at the University of Pennsylvania made the libraries and sequenced the reads. Dr. Lin Zhang aligned the raw data to the genome, annotated the reads, and processed the data to reported fragments per kilobase of transcript per million mapped reads. Rebekah C. Brooks assisted with further processing and presentation of this expression data as described in the Methods. Lin Zhang additionally assisted with upload of raw and processed data to the public repository Gene Expression Omnibus.

I thank Dr. James C. Alwine for illuminating discussions and his prior virology work that gave insight into our observations. I additionally thank Dr. Yongjun Yu and Tobi Maguire in the Alwine Lab for collaboration on the CMV studies and for helpful immunofluorescence protocol suggestions, respectively.

I thank Chirag H. Patel and Dr. Jonathan D. Powell for performing the murine T cell studies presented in the Results section in collaboration with our studies.

Drs. Arig Ibrahim-Hashim and Robert Gillies performed the immunohistochemistry staining and analyses of tumors hosted by control and bicarbonate-treated mice using tissue specimens from previous studies conducted by them and their colleagues Dr.

Pedro Enriques-Navas, Veronica Estrella, and Dr. Robert Gatenby. Arig Ibrahim-Hashim and Robert Gillies additionally generously provided PANC02 pancreatic tumor blocks for the immunohistochemical staining of CAIX and pS6 performed by Dr. Tianying Jiang and imaged by me.

Tianying Jiang and I further collaborated for P493 xenograft formation and tissue processing with Tianying subsequently performing the immunohistochemistry and immunofluorescence with imaging and quantification assistance from Frederick Keeney and James Hayden in the Wistar Imaging Core.

I thank Malini Riddle, Dr. Alessandra Porcu, and Dr. David K. Welsh for performing the single-cell luminescence imaging and analyses in collaboration with our studies.

I thank Feven Tameire and Dr. Constantinos Koumenis for instruction in polysome profiling and collaboration in executing and interpreting this experiment. I thank the Wistar Genomics Core for Tape Station analysis as part of this work.

Drs. Brett L. Ecker and Ashani T. Weeraratna performed additional T cell experiments to assist with responding to reviewers' questions.

I thank Dr. Celeste Simon for use of her microscope for live-cell imaging, many helpful suggestions and reagents, and formative instruction while a rotation student in her lab. I thank Dr. Bo Li for his plasmid from which I cloned the *PGK1 HRE* and his excellent teaching during my time in the Simon Lab.

I thank Dr. Todd Ridky for serving as chair of my thesis committee and co-advisor for my F30 fellowship, his helpful comments, and his continuous support.

I thank Dr. John Hogenesch for the U2OS *Arntl*::dLUC and U2OS *Per2*::dLUC cell lines, his useful suggestions, and his valuable perspectives.

I thank Dr. Brian Keith for feedback on this project through review of grant proposal drafts and perceptive questions following presentation of this work in seminars or thesis committee meetings.

We thank Dr. David Sabatini for discussion and reagents as noted in the Methods.

I thank Dr. Don Ayer for MDA-MB-231 cells.

I thank Dr. Karin Eisinger, Dr. Malay Haldar, and the Wistar Imaging Core for my use of their microscopes. I thank Dr. Andrea Stout in the University of Pennsylvania Cell and Developmental Biology Microscopy Core for assistance with T cell confocal imaging.

I thank Nam Woo Cho and Dr. Roger Greenberg for excellent training as a rotation student in the Greenberg Lab and a gift of U2OS parental cells.

I thank Maggie Krall, Dr. Skip Brass, and the MD-PhD program for their guidance and support.

I thank AFCRI and Cancer Biology faculty and students for insightful feedback at seminars over the years.

I thank Dang Lab members, especially Dr. Brian Altman for his generous instruction and useful advice both as a rotation student and afterwards, Dr. Zachary Stine for excellent guidance in assembly of grant proposals and much helpful feedback, Dr. Annie Hsieh for inspiring conversations and suggestions, Rebekah Brooks as mentioned above and for likewise beneficial conversations, Dr. Tianying Jiang for generous collaboration as mentioned above, and Dr. Adam Wolpaw for wise suggestions on approaches and interpretations. I thank other Dang Lab members Dr. Yan Xiang, Dr. Xue Zhang, and Patricia Brafford for assistance with studies not appearing here or otherwise helpful support.

I thank Chi for his brilliance, unwavering optimism, enthusiasm, trust, patience, approachability, thorough support, and the example he sets with his integrity, honesty, and generosity. I consider myself extremely fortunate to have been able to learn from Chi these past four years.

I thank my parents for their unconditional love. I thank my siblings, Eddie, Linus, Beatrice, and Caroline, for serving during these years as friends and distractions—as travel buddies, cheering marathon fans, sailing mates, long-run partners, hosts abroad and domestically—and as inspirations through their passion for their own fields of endeavor.

I thank friends—in and outside this program, Amherst and non-Amherst, runners and non-runners—for suggestions, perspective, encouragement, and laughs.

I thank Mehrzad for somehow still being my biggest supporter and cause for a smile even when on protracted “non-optional vacation” over 5,600 miles away.

Collaborators were supported by NIH/NCI grants R01CA157846 (JCA); R01AI077610, R01AI091481 (JDP); R01CA077575, U54CA193489 (RG); P30CA010815, R01CA174746 (ATW); Veterans Affairs Merit Award I01BX001146 (DKW); the Bloomberg-Kimmel Institute of Cancer Immunotherapy (JDP); and the Tissue Core Facility at the H. Lee Moffitt Cancer Center & Research Institute (an NCI designated Comprehensive Cancer Center, P30-CA076292).

## ABSTRACT

### ACID SUSPENDS THE CIRCADIAN CLOCK IN HYPOXIA THROUGH INHIBITION OF MTOR

Zandra E. Walton

Chi Van Dang

Recent reports indicate hypoxia influences the circadian clock through the transcriptional activities of hypoxia inducible factors (HIFs) at clock genes. Unexpectedly, we uncover a profound disruption of the circadian clock and diurnal transcriptome when hypoxic cells are permitted to acidify, recapitulating the tumor microenvironment. Buffering against acidification or inhibiting lactic acid production fully rescues circadian oscillation. Acidification of several human and murine cell lines, as well as primary murine T cells, suppresses mechanistic target of rapamycin complex 1 (mTORC1) signaling, a key regulator of translation in response to metabolic status. We find acid drives peripheral redistribution of normally perinuclear lysosomes away from perinuclear RHEB, inhibiting activity of lysosome-bound mTOR. Restoring mTORC1 signaling and the translation it governs rescues clock oscillation, revealing a model in which acid produced during the cellular metabolic response to hypoxia suppresses the circadian clock through diminished translation of clock constituents.

## TABLE OF CONTENTS

<b>ACKNOWLEDGMENTS.....</b>	<b>III</b>
<b>ABSTRACT .....</b>	<b>VIII</b>
<b>LIST OF TABLES .....</b>	<b>X</b>
<b>LIST OF FIGURES .....</b>	<b>XI</b>
<b>CHAPTER 1 - INTRODUCTION.....</b>	<b>1</b>
<b>CHAPTER 2 - RESULTS.....</b>	<b>15</b>
<b>CHAPTER 3 – CONCLUSIONS AND FUTURE DIRECTIONS .....</b>	<b>75</b>
<b>CHAPTER 4 – MATERIALS AND METHODS .....</b>	<b>121</b>
<b>APPENDIX .....</b>	<b>171</b>
<b>BIBLIOGRAPHY .....</b>	<b>191</b>

## LIST OF TABLES

### Appendix

Table 1 - Reagents and Resources.....	171
Table 2 - qPCR primers and DsiRNA oligos .....	186

## LIST OF FIGURES

### Chapter 1 - Introduction

Box 1.....	2
Box 2.....	3
Box 3.....	4
Box 4.....	7
Box 5.....	8
Box 6.....	10
Box 7.....	13

### Chapter 2 - Results

Figure 1.....	17
Supporting Figure 1.....	20
Figure 2.....	26
Supporting Figure 2.....	28
Figure 3.....	32
Supporting Figure 3.....	34
Figure 4.....	39
Supporting Figure 4.....	42
Figure 5.....	48
Supporting Figure 5.....	51
Figure 6.....	57
Supporting Figure 6.....	60
Figure 7.....	68
Supporting Figure 7.....	71

### Chapter 3 – Discussion and Future Directions

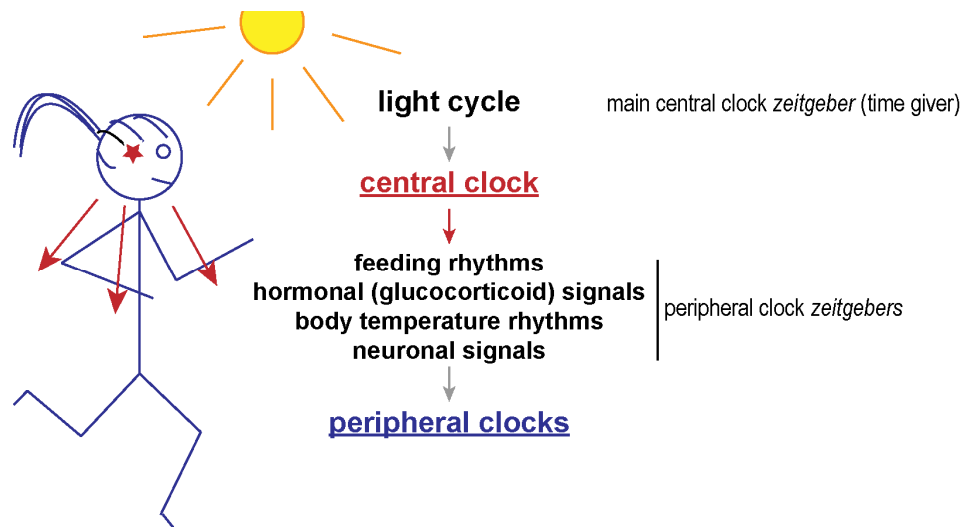
Figure 8.....	86
Figure 9.....	88
Figure 10.....	91
Figure 11.....	96
Figure 12.....	106
Figure 13.....	110
Figure 14.....	116

## CHAPTER 1 - Introduction

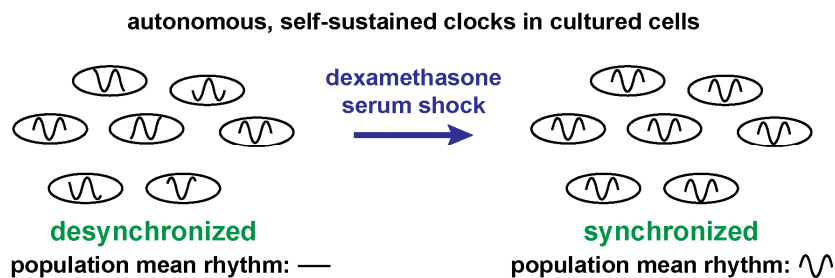
Some prokaryotes and nearly every eukaryote possess a form of a circadian clock (Dibner and Schibler, 2015). This convergent evolution, as well as the frequent ubiquity of such clocks within the various tissues of an organism, reflects the evolutionary fitness endowed by the ability to temporally align biological processes with the day-night cycle (Rosbash, 2009). In mammals, although clocks are hierarchically orchestrated, with a central hypothalamic clock sending synchronizing stimuli to peripheral clocks throughout the body, each peripheral clock, found in virtually every cell, is autonomous and capable of self-sustaining oscillation (Box 1) (Dibner et al., 2010). The molecular basis for these clocks is a series of interlocking negative feedback loops that take 24 hours to play out (Box 2) (Partch et al., 2014). In the core loop, the clock circadian regulator (CLOCK) and brain and muscle ARNT-Like 1 (BMAL1) heterodimer drives the expression of many E-box containing genes throughout the genome, including transcripts encoding its own inhibitors, the period (PER) and cryptochrome (CRY) proteins. This, together with reinforcing secondary loops, generates oscillating clock transcription factor activities and ultimately circadian rhythmicity of thousands of transcripts in a given tissue, particularly those with metabolic roles (Bass, 2012; Koike et al., 2012; Pizarro et al., 2013; Takahashi, 2017; Zhang et al., 2014). Subsequent oscillations in protein levels, enzymatic activities, metabolites, and cellular processes follow (Box 3) (Janich et al., 2015; Krishnaiah et al., 2017; Panda, 2016).

### Box 1 – Hierarchically organized circadian clocks anticipatorily time physiology

Circadian clocks allow organisms to anticipate cyclical (daily) events and coordinate physiologic processes with optimal timing (Bass and Takahashi, 2010). In mammals, clocks in the suprachiasmatic nucleus of the hypothalamus constitute a central pacemaker tuned to the appropriate phase by retina-sensed light relayed via the retinohypothalamic tract. Through neuronal and hormonal (e.g. glucocorticoid) outputs, rhythmic control of behaviors such as eating, and other signaling pathways, the central clock synchronizes the oscillation of autonomous peripheral clocks found in nearly every cell (Dibner and Schibler, 2015; Dibner et al., 2010).

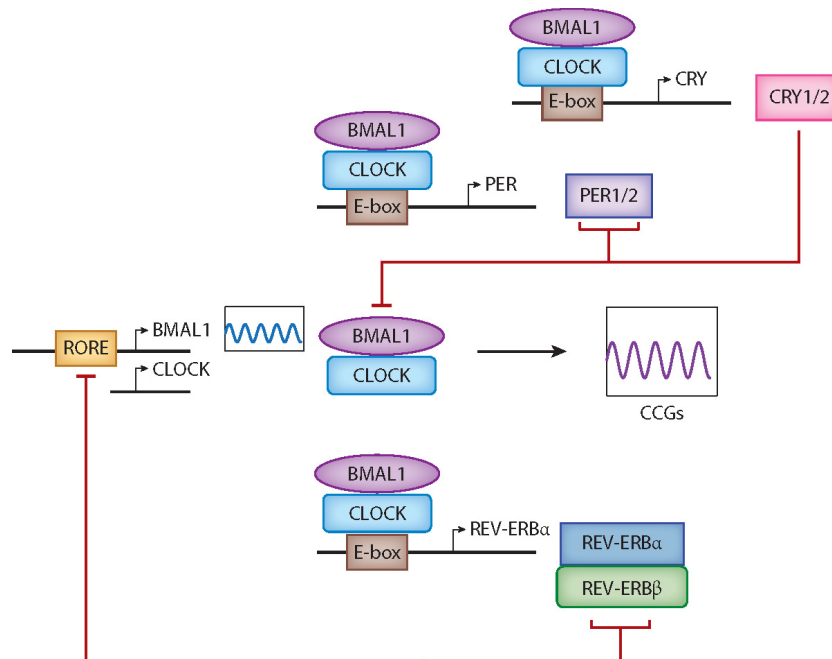


These cellular peripheral clocks can sustain oscillation outside the body, observance of which is aided by synchronizing a population of cultured cells with dexamethasone and serum *in vitro* (Balsalobre et al., 2000).



## Box 2 – Molecular mechanism of the mammalian circadian clock

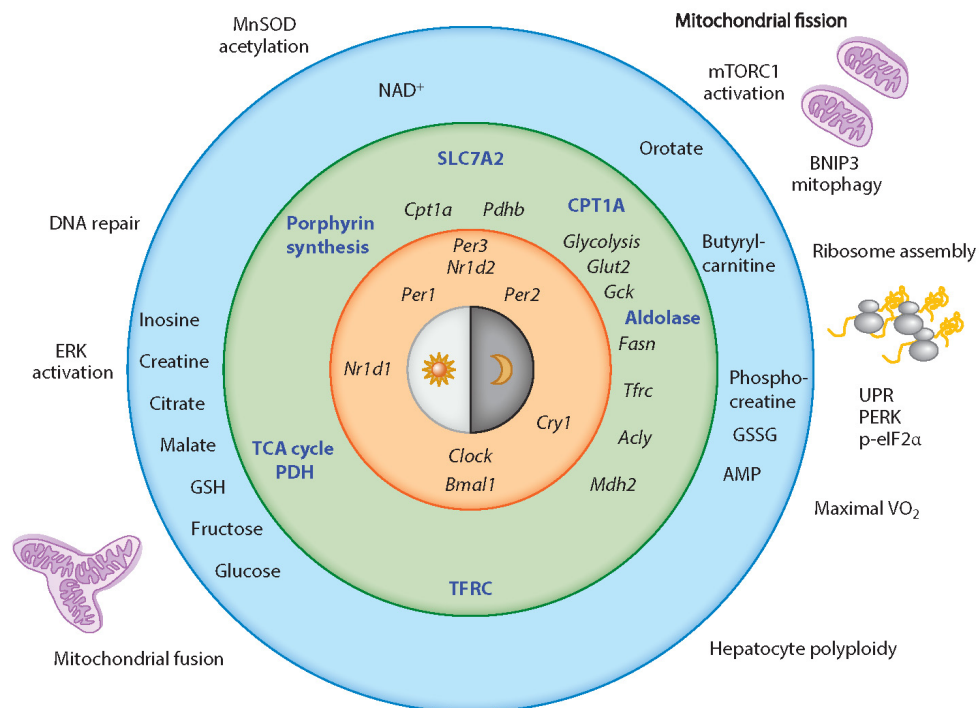
The mechanistic basis for both central and peripheral clocks is an interlocking network of feedback loops centered on the heterodimer CLOCK-BMAL1 (Partch et al., 2014). CLOCK-BMAL1 drives the expression of many genes containing E-box consensus sequences in their regulatory regions. Among these target genes are those encoding period (PER) and cryptochrome (CRY) proteins, which feedback to inhibit CLOCK-BMAL1 posttranslationally, forming the core negative feedback loop. A second negative feedback loop arises from CLOCK-BMAL1–mediated transcription of genes encoding REV-ERB proteins, which bind the RORE motif in the promoter for BMAL1 and negatively regulate its transcription. Together these feedback loops cause circadian oscillation of CLOCK-BMAL1 activity and, consequently, directly or indirectly, the circadian expression of thousands of downstream clock-controlled genes (CCGs) in a given tissue type.



Adapted with permission from Walton, Z. et al. (2018). Circadian Clock's Cancer Connections. Annual Review of Cancer Biology 2,133-153.

### Box 3 – Clocks optimally time metabolism

In the mouse liver, the core circadian clock (orange circle) oscillates in synchrony with the day-night cycle (innermost circle) and drives rhythmic expression of many genes involved in metabolic pathways (green circle) to appropriately time their transcription (black font) and subsequent translation (blue font). As a result, metabolites oscillate around the clock (blue circle), supporting (and also a consequence of) rhythmic cellular processes (outer area) optimally timed to anticipate demand. In addition to providing evolutionary fitness by timing metabolic activities to coincide with daily patterns in substrate (food) availability and product need, clocks also permit temporal segregation of otherwise incompatible processes (Eckel-Mahan and Sassone-Corsi, 2013; Feng and Lazar, 2012; Huang et al., 2011). Whether peripheral clocks continue to cycle normally and exert temporal constraint under metabolic or oncogenic stress, however, is largely unknown.



Abbreviations: AMP, adenosine monophosphate, BNIP3, BCL2 interacting protein 3; CPT1A, carnitine palmitoyltransferase 1A; ERK, extracellular signal-regulated kinase (a.k.a. MAPK); GSH, glutathione; GSSG, oxidized glutathione (glutathione disulfide); MnSOD, manganese-dependent superoxide dismutase (a.k.a. superoxide dismutase 2); NAD<sup>+</sup>, oxidized nicotinamide adenine dinucleotide; mTORC1, mechanistic target of rapamycin complex 1; PDH, pyruvate dehydrogenase; p-eIF2 $\alpha$ , phosphorylated eukaryotic translation initiation factor 2A; PERK, PRKR-like endoplasmic reticulum kinase; SLC7A2, solute carrier family 7 member 2 (a.k.a. cationic amino acid transporter 2); TCA cycle, tricarboxylic acid cycle; UPR, unfolded protein response; VO<sub>2</sub>, rate of oxygen consumption. Gene names: *Acly*, ATP citrate lyase; *Fasn*, fatty-acid synthase; *Gck*, glucokinase; *Glut2*, glucose transporter type 2 (a.k.a. *Slc2a2*); *Mdh2*, malate dehydrogenase 2; *Nr1d1*, *Nr1d2*, genes encoding REV-ERB $\alpha$  and REV-ERB $\beta$  proteins; *Pdhb*, pyruvate dehydrogenase beta (a component of the PDH complex); *Per1*, *Per2*, *Per3*, period genes; *Tfrc*, transferrin receptor encoding TFR1 (a.k.a. TFRC).

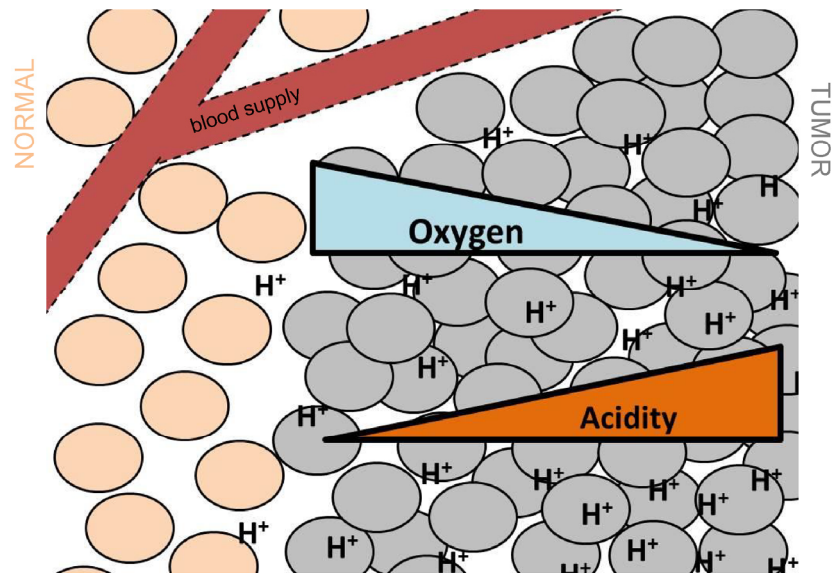
Adapted with permission from Walton, Z. et al. (2018). Circadian Clock's Cancer Connections. Annual Review of Cancer Biology 2,133-153. (figure credit: CV Dang)

Despite their physiological benefit, such extensive daily transcriptional-translational mobilizations, as well as the temporal constraints imposed by a clock, might pose a liability for cells during stress (Woelfle et al., 2004; Xu et al., 2013). Intriguingly, links have been uncovered between circadian disruption and cancer, with circadian disruption (e.g. night shift work) associated with increased incidence of certain cancers and deregulation of clock network components noted in some human malignancies and observed to accelerate tumorigenesis in mice (Kettner et al., 2016; Papagiannakopoulos et al., 2016; Shostak, 2017; Walton et al., 2018a). Recently, we identified that the oncogene *MYC* blunts oscillation of the molecular clock (Altman et al., 2015). Given that regulation of metabolism is a key clock function, we wondered if metabolic stress inherent to cancer might trigger circadian perturbations in cancer.

Exquisitely low oxygen tensions are common in solid tumors owing to outstripping of perfusion offered by abnormal tumor vasculature (Carmeliet and Jain, 2011; Gallagher et al., 2008; Gillies et al., 2002) (Box 4). As oxygen is required for energy-producing oxidative phosphorylation among other enzymatic activities, this poses a substantial challenge for tumor cells (Nakazawa et al., 2016). Hypoxia stabilizes hypoxia inducible factor alpha subunits (HIFs), allowing them to carry out a transcriptional program that profoundly alters metabolism to cope with the low oxygen tensions (Box 5) (Semenza, 2013). Resulting upregulation of glycolytic enzymes and simultaneous deflection of carbon away from the tricarboxylic acid (TCA) cycle cause a substantially elevated flux of glucose to lactic acid, acidifying the tumor microenvironment (Box 6) (Divakaruni et al., 2014).

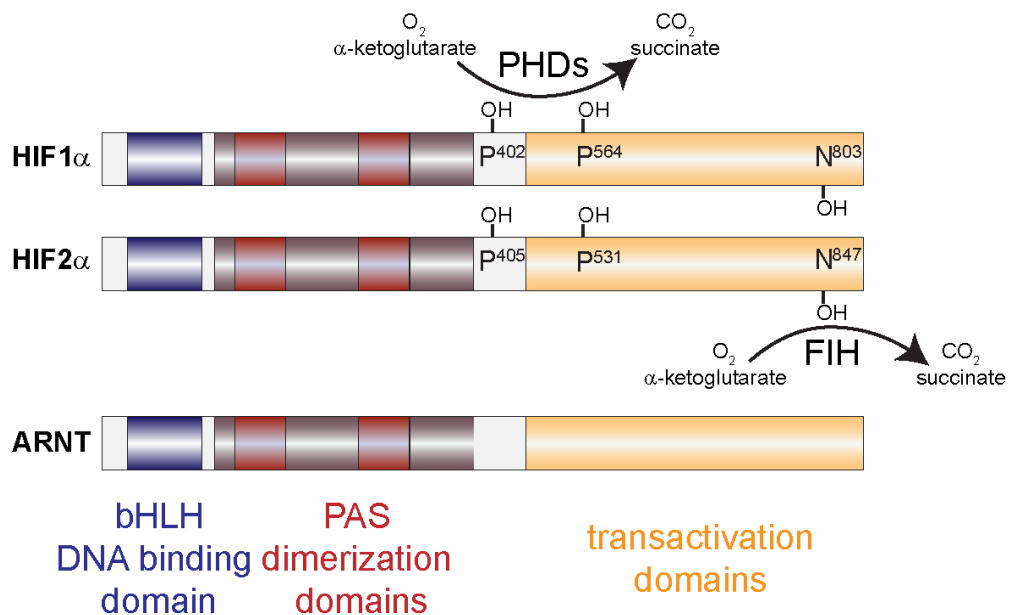
#### Box 4 – Tumor hypoxia

Solid tumors often exhibit hypoxic regions due to high metabolic activity of cancer cells and insufficient or abnormal angiogenesis in tumors (Carmeliet and Jain, 2011). The metabolic changes that ensue in response to low oxygen tensions cause this hypoxic stress to frequently be coupled to pH stress (Box 5, Box 6) (Gallagher et al., 2008; Gillies et al., 2002; Sattler et al., 2007; Song C.W., 2006). Necrotic tumor regions seemingly evince the severe end of a spectrum of such metabolic stress (Manzoor et al., 2008).



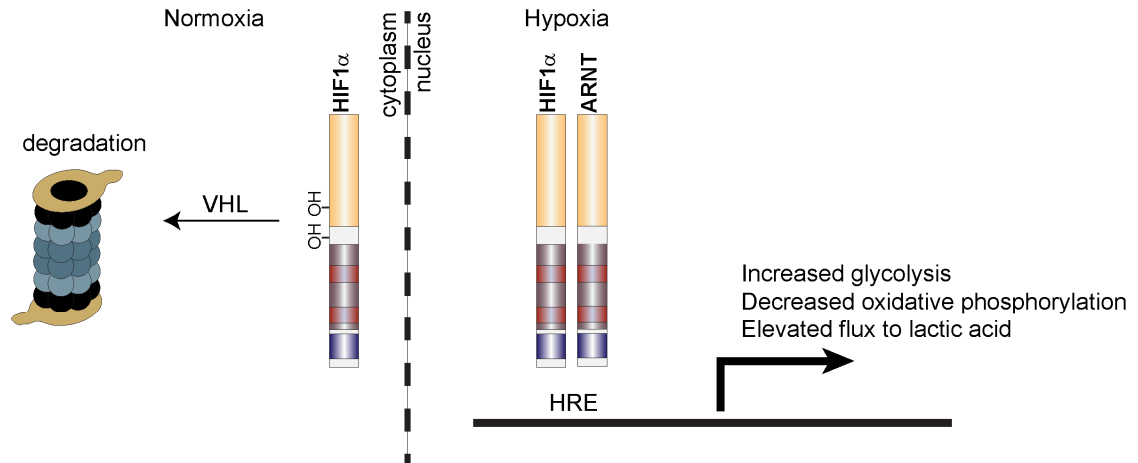
## Box 5 – Hypoxia inducible factors mediate the transcriptional response to low oxygen

Hypoxia inducible factor (HIF) transcription factors are silenced in normoxia (oxygen-replete conditions) as a consequence of oxygen ( $O_2$ )-dependent hydroxylation events (Keith et al., 2011; Schofield and Ratcliffe, 2004). HIF alpha subunit (HIF1 $\alpha$ , HIF2 $\alpha$ ) hydroxylation by prolyl-hydroxylases (PHD1, PHD2, or PHD3) leads to recognition by the E3 ubiquitin ligase complex component von Hippel-Lindau (VHL) and rapid proteasomal degradation. Factor inhibiting HIF (FIH) cooperates to block HIF signaling through transactivation-inhibiting hydroxylation of a C-terminal asparagine.



Hypoxia diminishes PHD and FIH activity largely through substrate ( $O_2$ ) limitation. Once thus stabilized, HIF alpha subunits translocate to the nucleus and dimerize with constitutively expressed ARNT (HIF1 $\beta$ ) to transcriptionally activate hypoxia-response element (HRE)-containing genes that aid survival in low oxygen (Majmundar et al., 2010; Semenza, 2007). In addition to these well-described profound metabolic

rewirings by HIF (Xie and Simon, 2017), we wondered if hypoxic signaling might also alter the circadian clock to direct cooperative confrontation of the hypoxic stress given the clock's central role in homeostatic metabolism.



PHDs = prolyl hydroxylases; bHLH = basic helix-loop-helix; PAS = PER-ARNT-SIM; P= proline; N = asparagine; OH = hydroxyl group; others as in text.

Elements of figures adapted from Keith, B. et al. (2011). HIF1 $\alpha$  and HIF2 $\alpha$ : sibling rivalry in hypoxic tumour growth and progression. *Nature Reviews Cancer* 12, 9-22., and Adams, J. (2004). The proteasome: a suitable antineoplastic target. *Nature Reviews Cancer* 4, 349-60.

#### **Box 6 – HIF-mediated metabolic rewiring increases acid production through elevated glycolytic flux**

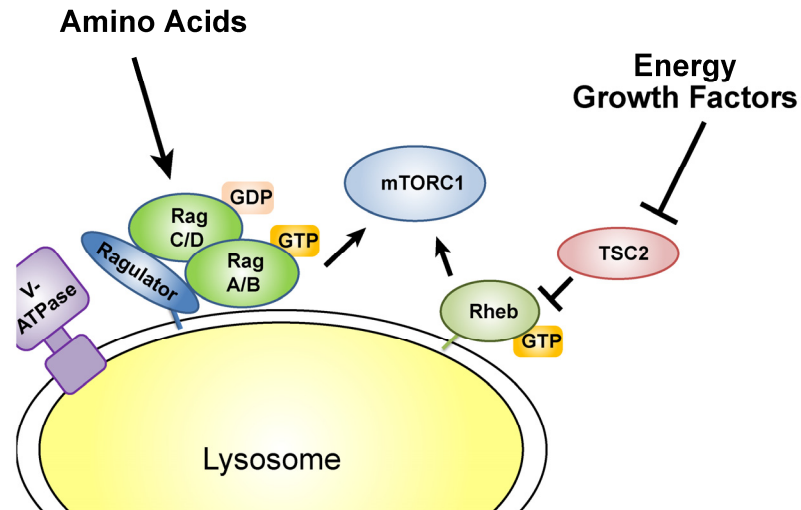
Mitochondrial metabolism (oxidative phosphorylation) slows in hypoxia. To compensate, HIF1 $\alpha$  spurs anaerobic glycolysis, greatly elevating flux of glucose to lactate through upregulation of genes encoding a glucose transporter (GLUT1), glycolytic enzymes, lactate dehydrogenase A (LDHA), and an inhibitor of pyruvate tricarboxylic acid (TCA) cycle entry, pyruvate dehydrogenase kinase 1 (PDK1) (all in orange font below) (Kim et al., 2006). Conversion of pyruvate to lactate by LDH enzymes cycles NADH back to NAD<sup>+</sup>, allowing high glycolytic flux to continue. Proton (acid) production increases in hypoxia because of this shift to acid-generating glycolysis to meet ATP demands in place of more proton-neutral full oxidation of glucose to CO<sub>2</sub> (see detailed H<sup>+</sup> accounting in reference (Divakaruni et al., 2014)).



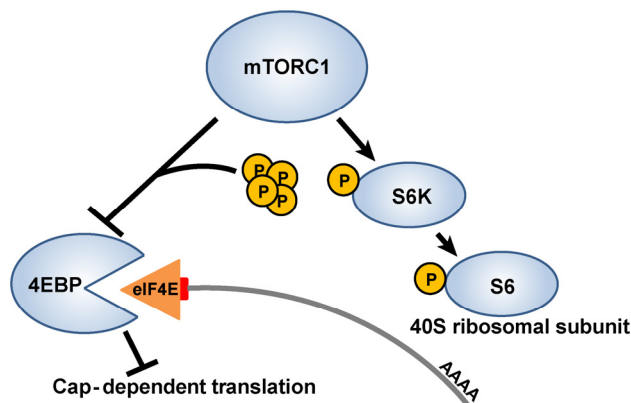
We wondered if hypoxia might additionally rewire clock-controlled metabolism to meet the hypoxic challenge. Indeed, recent papers have shown HIFs to be capable of influencing various clock transcripts in a cell-type-dependent manner (Adamovich et al., 2017; Peek et al., 2017; Wu et al., 2017). Here, we report a more profound suspension of the circadian clock and the diurnal transcriptome when hypoxic cells are permitted to acidify their environment in a manner recapitulating the tumor microenvironment (Chapter 2 Figure 1A). Pursuing the underlying clock-suppressive mechanism reveals a previously undescribed means by which low pH potently inhibits the key regulator of cellular metabolism mechanistic target of rapamycin complex 1 (mTORC1) (Box 7) and gives functional significance to a long-recognized phenomenon of lysosome spatial scattering in low pH previously of unknown consequence (Heuser, 1989). We find this mechanism of acid-mediated suppression of mTORC1 to be shared by T cells in addition to the multiple tumor cell lines tested, suggesting tumor acidity is posed to facilitate tumorigenesis through immunomodulation as well as stress-adaptation-driven circadian suppression.

#### **Box 7 – mTOR senses stress signals to appropriately time anabolic processes**

mTOR complex 1 (mTORC1), a multi-protein assembly composed in part by the kinase mTOR, regulates cell growth, matching anabolic processes to periods of substrate sufficiency and growth-affirmative humoral signals (Saxton and Sabatini, 2017). Such coordination emerges from multiple parameters indicative of suitability for growth converging on two populations of GTP-binding proteins immediately upstream of mTORC1, Ras-related GTP-binding (RAG) and Ras homolog enriched in brain (RHEB) proteins. Sensors for arginine, leucine, and methionine signal amino acid sufficiency to lysosome-localized RAG heterodimers through a series of protein interactions that ultimately control RAG nucleotide binding states (Gu et al., 2017; Saxton et al., 2016; Wang et al., 2015; Wolfson et al., 2016; Wolfson and Sabatini, 2017). Correct GTP/GDP loading of RAG proteins recruits mTORC1 to the lysosomal surface where it is believed a population of RHEB resides allowing activation of mTOR kinase by RHEB (Sancak et al., 2010). RHEB is GTP-bound and thus capable of activating amino-acid-recruited mTOR so long as the tuberous sclerosis complex (TSC), which contains TSC2, the GTPase-activating protein (GAP) for RHEB, is spatially disengaged from RHEB in response to growth factors (e.g. signals relayed through phosphatidylinositol 3-kinase (PI3K) and mitogen-activated protein kinase (MAPK) signaling) (Menon et al., 2014) and kept inactive through absence of TSC2-activating stress signals (e.g. energy insufficiency sensed by adenosine monophosphate (AMP)-sensitive AMP kinase (AMPK)) (Dibble and Manning, 2013).



Active mTORC1 positively regulates translation through mTOR phosphorylation of downstream substrates (Nandagopal and Roux, 2015; Thoreen et al., 2012). Phosphorylation of ribosomal S6 kinase (S6K) stimulates S6K phosphorylation of ribosomal protein S6, a component of the 40S ribosomal subunit, driving cell growth through debated mechanisms (Meyuhas, 2015). mTOR also phosphorylates inhibitory binding partners of the eukaryotic initiation factor 4E (eIF4E), the 4EBP proteins, preventing their engagement with eIF4E and thereby releasing suppression of cap-dependent translation. mTORC1 thus senses stress and reserves energy-costly translation and downstream biosynthetic processes for periods in which reserves of energy and building blocks can support these demands.



## CHAPTER 2 - Results

### Hypoxia suspends the clock through acid

To explore the effect of hypoxia on the clock, we utilized the U2OS *Arntl*::dLUC circadian reporter cell line, a human osteosarcoma line in which luciferase expression is driven by the promoter for *Arntl*, the gene encoding BMAL1 (Zhang et al., 2009). We avoided assessing bioluminescence, an O<sub>2</sub>-dependent reaction, in low oxygen tensions by periodically harvesting lysate from cells grown in hypoxia or normoxia over a timecourse for assay of luciferase activity in normoxia. We found that hypoxia significantly suppressed the circadian oscillation of this reporter (1B, S1A). This disruption was readily reversible upon reoxygenation (S1A), consistent with a possible role for HIFs. Indeed, stabilization of HIF with dimethyloxallylglycine (DMOG) (1C, 1D) or desferrioxamine (DFX) (S1B), inhibitors of the prolyl hydroxylases that mediate HIF degradation, was sufficient to reversibly disrupt oscillation of the *Arntl* reporter and a *Per2* promoter-reporter in normoxic cells monitored continuously by a luminometer. Knockdown of *HIF1A* and *EPAS1* (HIF-2 $\alpha$ ) restored oscillation of the *Arntl* reporter in DMOG, confirming that HIFs mediate disruption of circadian oscillation in hypoxia (1E).

Intriguingly, the ability of DMOG to disrupt the clock depended highly on the buffering capacity of the media. Hypoxia or DMOG, via HIF, greatly increases flux of glucose to lactic acid. Buffering against acidification fully preserved clock reporter oscillation in DMOG-treated live cells (1F, 1G). pH did not affect the luciferase reaction, as identical results were seen in lysates collected and assayed in neutral pH (S1C, S1D). Analogous results were seen in low oxygen tensions, with the clock suppressed reversibly in low buffer media but temporarily protected from disruption in more highly buffered media until later time points when acid overwhelmed the buffering capacity

(S1E). Acidification of low buffer media upon HIF stabilization (1F, S1E) was anticipated given that HIF drives acid-generating glycolytic flux through induction of glycolysis enzymes and lactate dehydrogenase A (*LDHA*) (Chapter 1, Box 6). Surprising, however, was that pH commensurate with that found in solid tumors (Gallagher et al., 2008) was sufficient to reversibly disrupt the circadian clock (1I, S1F). Correspondingly, knockdown of HIFs rescued clock oscillation (1E) in association with normalization of HIF $\alpha$ -responsive glycolytic mRNAs (S1K, S1L) and pH (1H). Further, titration with a highly specific chemical inhibitor of LDHA (Boudreau et al., 2016) rescued clock oscillation (1J) in proportion to normalization of pH (1K). Application of the inhibitor in the presence of acidic media failed to rescue clock oscillation (1J, K), consistent with rescue through on-target reduction in acid production.

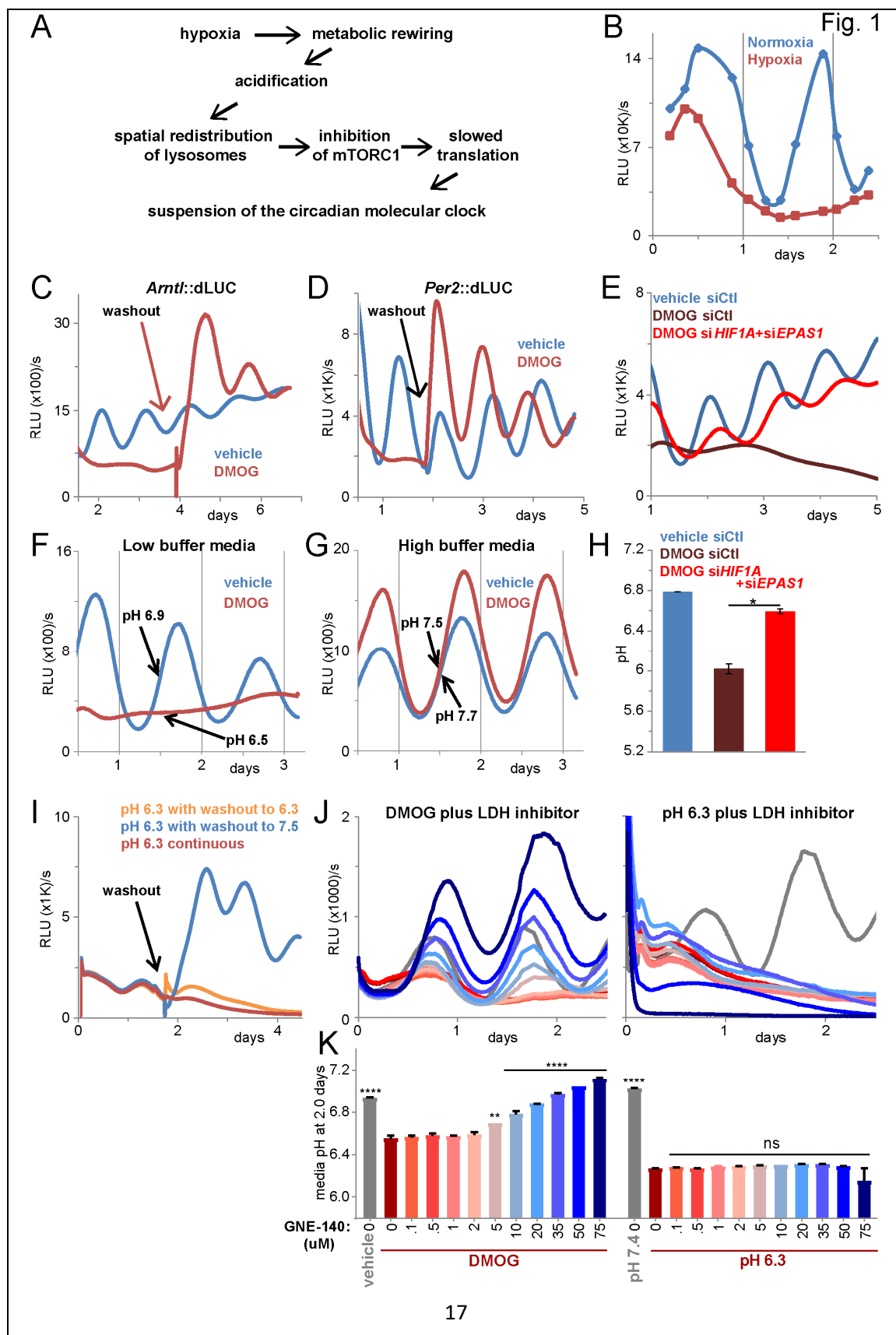


**Figure 1 – Hypoxic metabolism suspends the circadian clock through generation of acid**

**A.** Summary of findings in this report. **B.** Lysate luciferase activity (relative light units (RLU)) of U2OS cells stably expressing the *Arntl*::dLUC circadian clock reporter grown in normoxia or hypoxia (1% O<sub>2</sub>) for 57 hours. RE of 2, 1-3 BR each. **C.** Continuous luminescence monitoring of U2OS *Arntl*::dLUC cells treated with 750 uM DMOG or vehicle. DMOG washout at 4 days. RE of >5. **D.** Cells stably expressing the *Per2*::dLUC reporter treated with 1 mM DMOG as in C. Washout of vehicle/DMOG at 1.7 days. RE of 2, 1-3 BR. **E.** Luminescence monitoring of U2OS *Arntl*::dLUC cells treated with non-targeting control (siCtl) siRNA or siRNA against both HIF alpha subunits (*HIF1A*, *EPAS1*) prior to exposure to vehicle or 750 uM DMOG. Mean of 3 BR. RE of 3. **F./G.** Luminescence monitoring of U2OS *Arntl*::dLUC cells treated with 1 mM DMOG or vehicle in low (F) or high (G) buffer media. Mean of 2 BR. RE of >5. Indicated mean media pH after 1.5 days for 2 BR treated in parallel (standard error of the mean (SEM) <0.05). **H.** Media pH after 4 days of DMOG treatment in low buffer media following siRNA treatment as in E. Mean pH of 2 BR ± SEM. T-test (unpaired, two-tailed, unequal variances) \*p≤0.05. **I.** Luminescence monitoring of U2OS *Arntl*::dLUC cells grown in triplicate in media of pH 6.3. After 1.5 days, media of two plates was exchanged for media of pH 7.5 (washout) or 6.3 (mock washout). RE of >3. **J./K.** Luminescence monitoring (J) and media pH after 2 days (K) of U2OS *Arntl*::dLUC cells treated with vehicle or 750 uM DMOG (left) or pH 7.4 or pH 6.3 media (right) and the indicated concentration of GNE-140 (color-coded as in K). Mean of 2 BR (+/- SEM in K). Ordinary one-way ANOVA with Dunnett's multiple comparison test comparing all means to respective control (DMOG or pH 6.3 condition with 0 uM

GNE-140) \*\* $p \leq 0.01$ , \*\*\*\* $p \leq 0.0001$ , ns =  $p > 0.05$ . RE of 3. All cells B-K synchronized (see Methods) at time 0. RE = representative experiment. BR = biological replicates. See also Figure S1.

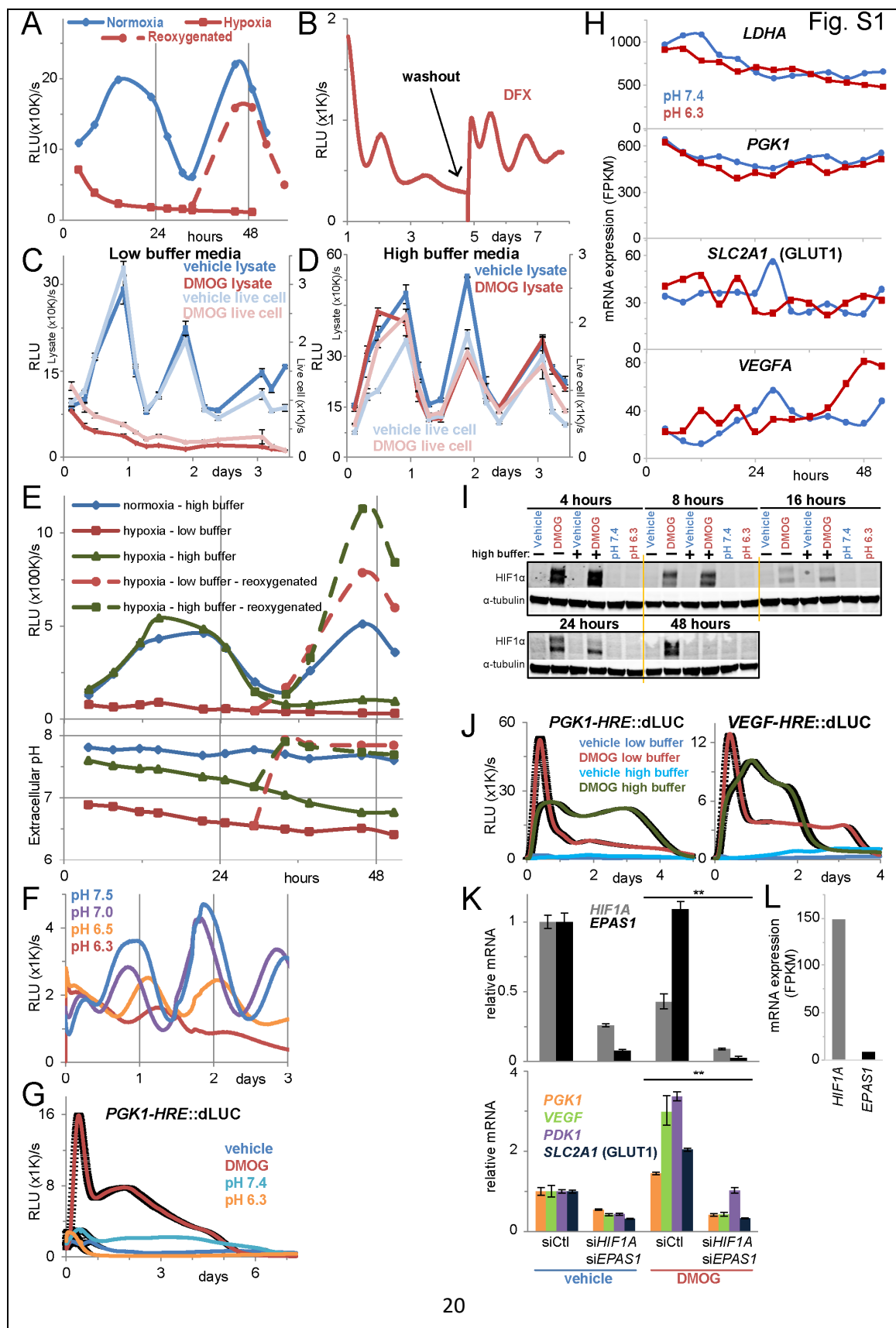


**Figure S1. Acid produced by HIF-mediated metabolism disrupts oscillation of the molecular circadian clock. Related to Figure 1.**

**A.** Luciferase activity of lysate collected periodically from U2OS *Arntl*::dLUC cells synchronized (with dexamethasone and media change) and grown in normoxia or hypoxia (1% O<sub>2</sub>, media pre-deoxygenated) for up to 57 hours. After 33 hours some cells were removed from hypoxia and their media exchanged for normoxic media. Luminescence plotted as relative light units (RLU). Representative experiment of 2. **B.** Real-time luminescence monitoring of U2OS *Arntl*::dLUC cells synchronized and treated with 18.75 uM desferrioxamine (DFX). After 4.7 days, DFX-containing media was exchanged for fresh media. Representative experiment of >5. **C./D.** Luciferase activity of lysate and luminescence of live cells immediately prior to lysate harvest of U2OS *Arntl*::dLUC cells synchronized and treated with 1mM DMOG or vehicle for up to 3.5 days in low (C) or high (D) buffer media. Data presented as mean of cells plated in triplicate  $\pm$  standard error of the mean (SEM). Representative experiments of two each with biological triplicates. **E. Upper panel:** Luciferase activity of lysate collected periodically from U2OS *Arntl*::dLUC cells synchronized and grown in normoxic high buffer or hypoxic (1% O<sub>2</sub>, media pre-deoxygenated) low or high buffer conditions for up to 51 hours. After 29 hours some cells were removed from hypoxia and their media exchanged for normoxic high buffer media. Data presented as mean of technical duplicates  $\pm$  standard deviation (SD) (but error bars generally too small to see). Representative experiment of 2. **Lower panel:** pH of media across timecourse. **F.** Real-time luminescence monitoring of U2OS *Arntl*::dLUC cells synchronized and grown in media of initial pH of 7.5, 7.0, 6.5, and 6.3. Representative experiment of 2 each with 1-2 biological replicates. Note the data shown for pH 6.3 appear also in

Figure 1H as the data were divided between these figures for clarity. **G.** Real-time luminescence monitoring of U2OS cells stably expressing a hypoxia response element (HRE) reporter derived from the HRE of *PGK1* (*PGK1-HRE::dLUC*) synchronized and treated with media pH 7.4 or 6.3 or 300  $\mu$ M DMOG or vehicle in low buffer conditions. Data presented as the mean of cells plated in triplicate  $\pm$  SEM error bars. **H.** Expression of the hypoxia inducible factor (HIF)-responsive genes lactate dehydrogenase A (*LDHA*), phosphoglycerate kinase 1 (*PGK1*), solute carrier family 2 member 1 (*SLC2A1*, GLUT1), and vascular endothelial growth factor A (*VEGFA*) in U2OS *Arntl::dLUC* cells in acidic (pH 6.3) and neutral (pH 7.4) media over a 52-hour timecourse as determined by RNA-sequencing (RNA-seq) of RNA collected every 4 hours. Reported as fragments per kilobase of transcript per million mapped reads (FPKM). **I.** Immunoblot for HIF1 $\alpha$  using lysate collected periodically from U2OS *Arntl::dLUC* cells treated with 1 mM DMOG in low or high buffer media or media of pH 7.4 or 6.3 (in parallel to Fig 2B-D). **J.** Real-time luminescence monitoring of U2OS cells stably expressing *PGK1-HRE::dLUC* or a reporter derived from the HRE of *VEGF* (*VEGF-HRE::dLUC*) synchronized and treated with 1mM DMOG or vehicle in low or high buffer media. Data presented as mean of  $\geq 2$  plates  $\pm$  SEM error bars. Representative experiment of  $\geq 2$  per reporter. **K.** Relative expression of HIF $\alpha$  subunits (upper) and HIF-responsive genes (lower) in U2OS *Arntl::dLUC* cells following treatment with non-targeting control (siCtl) siRNA or siRNA against both HIF1 $\alpha$  subunits (*HIF1A*, *EPAS1*) prior to synchronization and DMOG (787.5  $\mu$ M) treatment as in 1E and 1H. 10 nM siRNA each condition (5 nM each when two siRNA). qPCR of RNA collected 14 hours after DMOG or vehicle treatment, with expression normalized to respective target expression in the siCtl vehicle condition. Data presented as mean

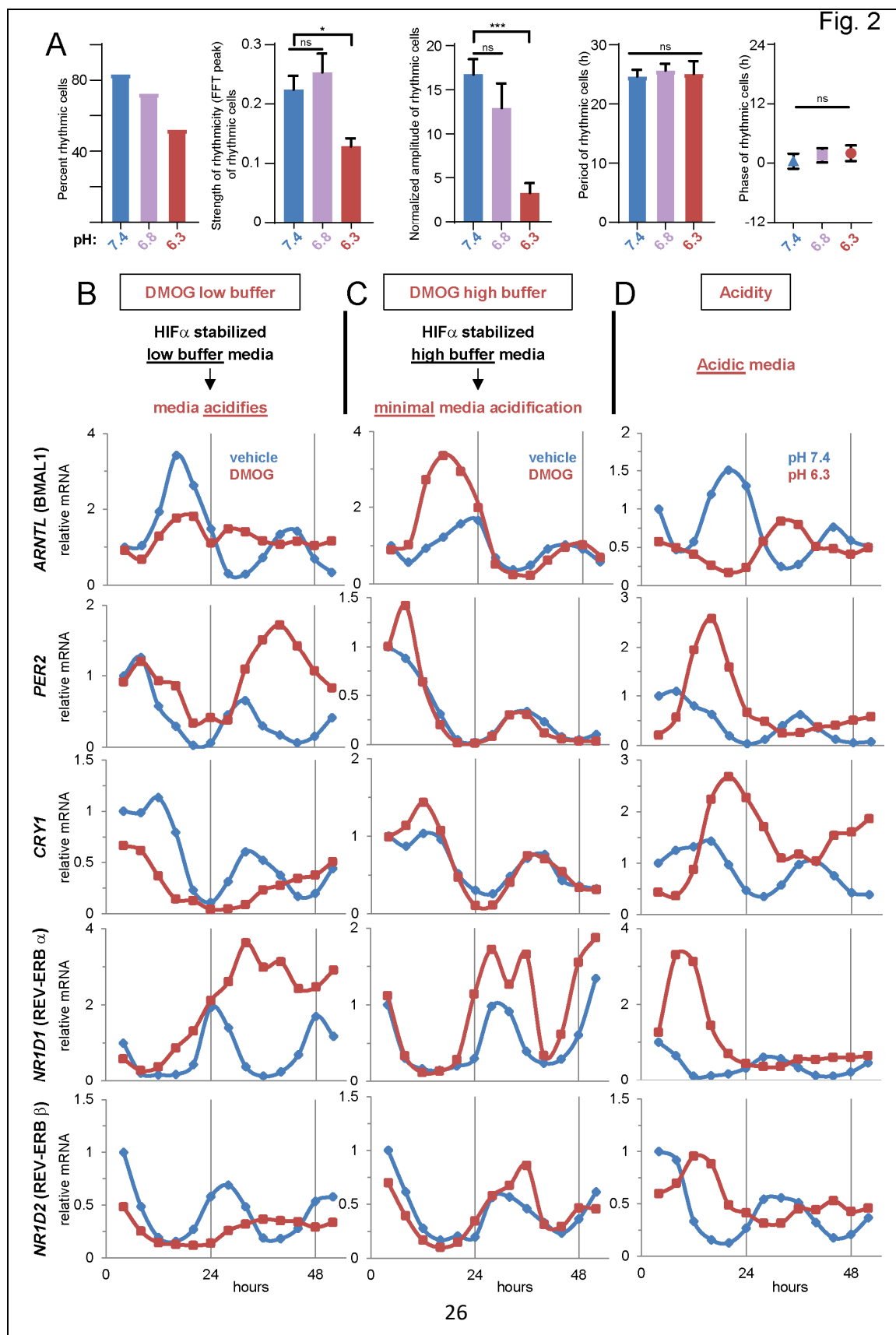
of technical triplicates  $\pm$  SEM. T-tests of individual genes (unpaired, two-tailed, unequal variance),  $**p<0.01$  each. L. Expression of genes encoding HIF $\alpha$  subunits in U2OS *Arntl*::dLUC cells after 4 hours in media of pH 7.4 as determined by RNA-seq.

Importantly, acid failed to stabilize HIF1 $\alpha$  (S1I), activate a reporter of HIF transcription (S1G), or induce HIF-responsive genes (S1H). Although highly buffered media does shorten the duration of high HIF-stability (S1I), destabilization of HIF does not account for the ability of highly buffered media to rescue the clock, as HIF is transcriptionally active in highly buffered media (S1J). Moreover, for the first 32 hours, induction of pyruvate dehydrogenase kinase 1 (*PDK1*) in response to DMOG or hypoxia is comparable in both low and highly buffered media (S2A)—indicating robust HIF activity across this interval in all buffer conditions—however vastly different effects are seen on the clock (S2B, S2C). This discordance between HIF transcriptional activity and clock oscillation stands in contrast to the high concordance between media pH (S2D) and clock oscillation (S2B, S2C). Hence, clock disruption by hypoxia is an indirect consequence of HIF transcriptional abilities mediated by acid.

## Disruption of the clock network by acid is extensive

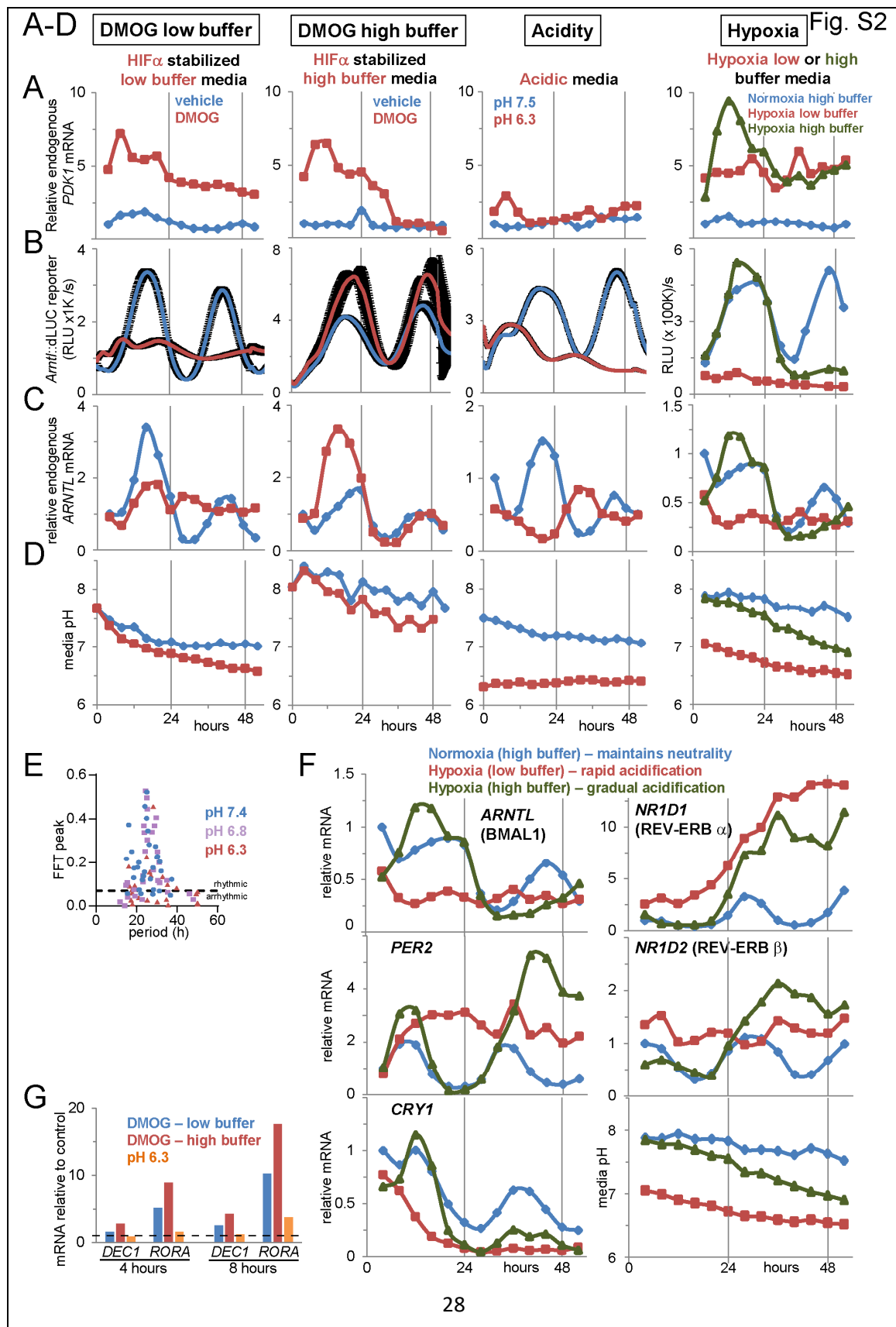
Single-cell luminescence imaging (Welsh et al., 2005; Welsh et al., 2004) revealed acid severely dampened amplitude without significant alteration of period or phase, indicating low pH caused disruption not through loss of coherence of the cell population but through suppression of the molecular oscillator (2A, S2E). To fully characterize this acid-mediated clock perturbation in hypoxia, we stabilized HIF with DMOG in media of high or low buffering capacity and assessed transcript levels of components of the core clock every 4 hours over a 52-hour timecourse (2B-C). Cells grown in neutral (pH 7.4) or acidic (pH 6.3) media were similarly probed (2D). The expression of endogenous *ARNTL* revealed by these timecourses faithfully matched the luminescence detected from the *Arntl::dLUC* reporter (S2B, S2C). These timecourses evinced that HIF-induced acidification disrupted the normal circadian oscillation of all members of the core clock assessed, causing loss of both the 24-hour periodicity of these genes and the antiphasic relationship between *ARNTL* and its targets (*PER*, *CRY*, *NR1D1*, and *NR1D2*) (2B). Highly buffered media rescued these distortions (2C, S2D). Acidic media was sufficient to disrupt the clock network (2D) with kinetics that outpaced that in response to gradual HIF-mediated acidification (2B, S2D). Like DMOG, hypoxia severely disrupted the clock in low buffer, halting oscillation of all assessed core clock components (S2F). In agreement with luciferase-reporter results (S1E), buffered media preserved hypoxic clock oscillation for 24-28 hours, after which oscillation diminished as the media acidified (S2F). Intriguingly, some components of accessory loops of the clock (*BHLHE40* (DEC1), *RORA*) remained induced by HIF in buffered media (S2G), indicating that their induction was insufficient for clock perturbation.

Fig. 2



**Figure 2 – Acidification is both necessary and sufficient to disrupt the clock network.**

**A.** Rhythmicity, amplitude, period, and phase as a function of media pH as determined by single-cell luminescence imaging of U2OS *Arntl*::dLUC cells. Mean  $\pm$  SEM of  $\geq 25$  analyzed cells (13-25 rhythmic) each pH. ANOVA with post-hoc Dunnett's comparing to control pH 7.4. \* $p < 0.05$ , \*\*\* $p < 0.001$ , ns= $p > 0.05$  **B./C.** Expression of endogenous core clock components assessed by qPCR over a 52-hour timecourse in synchronized U2OS *Arntl*::dLUC cells treated with 1 mM DMOG or vehicle in low (A) or high (B) buffer media. **D.** Expression similarly probed in parallel in cells treated with neutral (pH 7.4) or acidic (pH 6.3) media. See also Figure S2.



**Figure S2. Low pH mediates suppression of the endogenous clock network in hypoxia. Related to Figure 2**

**A.** Expression of the HIF-responsive gene pyruvate dehydrogenase kinase (*PDK1*) during the timecourses shown in Fig 2B-D as well as in a similar timecourse obtained in hypoxia (S2F, described below) as determined by qPCR and normalized to the respective control (e.g. vehicle, pH 7.4, normoxia) 4 h time point. **B.** Real-time luminescence monitoring of U2OS *Arntl::dLUC* cells treated in parallel to the endogenous RNA timecourses in Fig. 2B-D. Mean of cells plated in triplicate or duplicate  $\pm$  SEM error bars. Data from the hypoxic timecourse shown in S1E are also shown again here for completeness of comparisons. **C.** Endogenous *ARNTL* expression (previously depicted in Fig. 2B-D or appearing in S2F) is shown to highlight that the luciferase reporter shown in B closely mirrors these endogenous transcript levels. **D.** Media pH over the same timecourses as C (and Fig. 2B-D). **E.** Scatterplot of normalized fast Fourier transform (FFT) peak (descriptive parameter of variance of periodic data indicative of strength of rhythmicity) vs. period for individual cells analyzed by single-cell luminescence imaging (n= 30, 29, 25 for pH 7.4, 6.8, 6.3, respectively). Cells above the annotated FFT=0.07 threshold were scored rhythmic as cells with a period ( $\tau$ ) clearly outside the circadian range ( $\tau < 15$  h,  $\tau > 35$  h) tended to have a FFT peak value  $< 0.07$ . Cells with FFT peak  $< 0.07$  were scored arrhythmic. Percent rhythmic cells reported in Figure 2A is the percent of cells analyzed with FFT peak  $\geq 0.07$ . See Methods. **F.** Expression of constituents of the endogenous core clock over a 52-hour timecourse in U2OS *Arntl::dLUC* cells synchronized and grown in normoxic high buffer or hypoxic (1% O<sub>2</sub>, media pre-deoxygenated) low or high buffer conditions for 52 hours. Total RNA was collected every 4 hours and expression was

assessed by qPCR and normalized to that at 4 h in normoxia. Media pH during this timecourse (shown also in D) shown here to highlight the correlation between acidification and suppression of circadian oscillation of transcripts. **G.** Expression of *DEC1* (*BHLHE40*) and *RORA* during 1 mM DMOG treatment or upon exposure to acidic (pH 6.3) media relative to control (vehicle or pH 7.4) conditions at 4 or 8 hours after synchronization and exposure. Representative experiment of at least two independent experiments.

Given the extensive clock disruption in acid, we suspected the circadian transcriptome might be impacted. RNA-sequencing (RNA-seq) over the 52-hour timecourses revealed virtually identical expression profiles of the core clock as measured by qPCR, confirming the reliability of RNA-seq to address this question (S3A). Using ARSER, a statistical test of circadian rhythmicity (Yang and Su, 2010), we interrogated protein-coding transcripts and identified 1206 robustly circadian transcripts in neutral pH ( $p < 0.05$ , false discovery rate (FDR)  $< 0.2$ ) (3A, 3B). As expected, among significantly circadian transcripts were those encoding the core clock, secondary feedback loops (e.g. *NR1D1*, *NR1D2*), clock output regulators (*DBP*, *TEF*), and clock paralogs (e.g. *NPAS2*) (3C, S3C). These 1206 genes illustrate the robust cell autonomous circadian transcriptome (3A). Not surprisingly, the cell cycle and circadian clock topped the enriched pathways (3D), with many additional functional categories represented including aspects of metabolism, DNA repair, gene expression, and protein modification.

By contrast, less than 8% as many transcripts in cells exposed to acidic media met statistical significance for circadian oscillation (3B, S3B). Nearly all the 1206 robustly circadian genes lost oscillation in acidic media (3A), including members of the core clock (3C, S3C). Additionally, of the 86 transcripts deemed circadian in acid, many appeared only weakly so (S3B) and all but 12 were not circadian at pH 7.4, illustrating that few strongly oscillating transcripts retained their circadian profile in acid (S3B). Thus, acid profoundly suppresses both the core clock and circadian transcriptome. Further, acid induced ( $\log_2 > 1$ ,  $n = 571$ ) and suppressed ( $\log_2 < -1$ ,  $n=859$ ) many transcripts (3E-G), particularly those involved in the unfolded protein response or the cell cycle, respectively (S3D). Together these findings reveal a multifaceted cellular response to acid, which suppresses the circadian clock and activates stress responses.

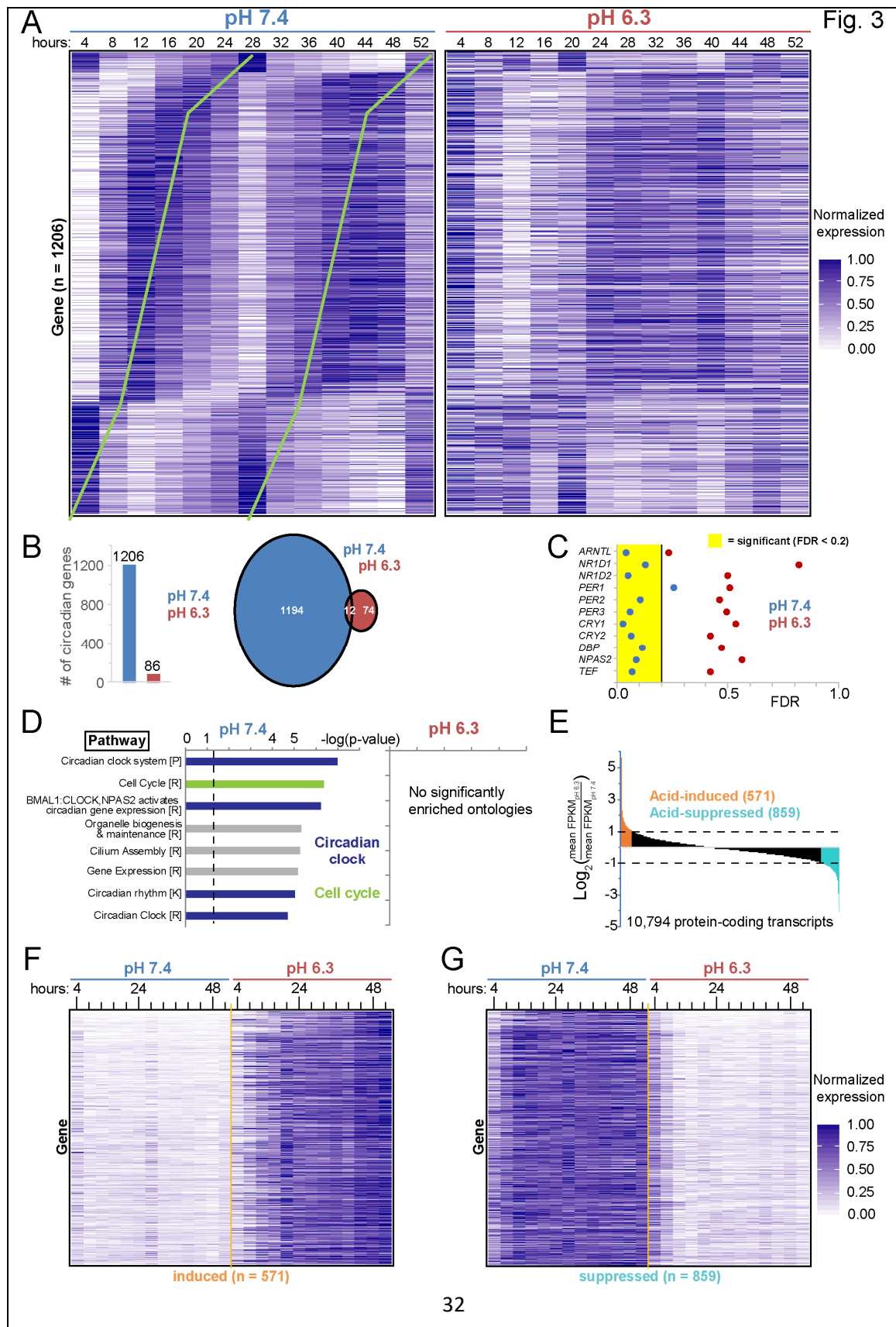


**Figure 3 – The normally circadian transcriptome ceases oscillation in acid.**

**A.** Expression in pH 7.4 and 6.3 of the 1206 protein-coding genes with statistically significant circadian oscillation in neutral conditions (pH 7.4) ( $p < 0.05$ , false discovery rate (FDR)  $< 0.2$ ) ordered by pH 7.4 phase. Fragments per kilobase of transcript per million (FPKM) mapped reads determined from RNA-seq of RNA collected every 4 hours for 52 hours from U2OS *Arntl::dLUC* cells treated with media of each pH as in 2D. Normalized expression (see Methods) color-coded as indicated. Green lines highlight the circadian periodicity in expression in pH 7.4. **B.** Histogram and Venn diagram indicating the number of protein-coding genes with statistically significant circadian oscillation in pH 7.4 or 6.3 or both. **C.** FDR statistic of test for circadian rhythmicity of expression (as in A) for core and secondary feedback loop clock genes and representative clock paralogs (*NPAS2*) and output regulators (*DBP*, *TEF*) in pH 7.4 or 6.3. **D.** Pathway ontologies significantly enriched (B&Y  $q < 0.05$ ) amongst circadian transcripts indicated in B. P=PantherDB, R=Reactome, K=KEGG. Terms related to cell cycle and clock colored as shown.  $p < 0.05$  above dashed line. **E.** Acid-induced and acid-suppressed transcripts defined as  $\log_2$  of the ratio of the average expression over all 13 time points (4h-52h) in pH 6.3 to pH 7.4  $> 1$  or  $< -1$ . **F./G.** Expression in pH 7.4 and 6.3 of the 571 acid-induced (F) and 859 acid-suppressed transcripts (G) defined in E. Color scale as in A. Ranked from top by most highly induced or suppressed. See Figure S3.

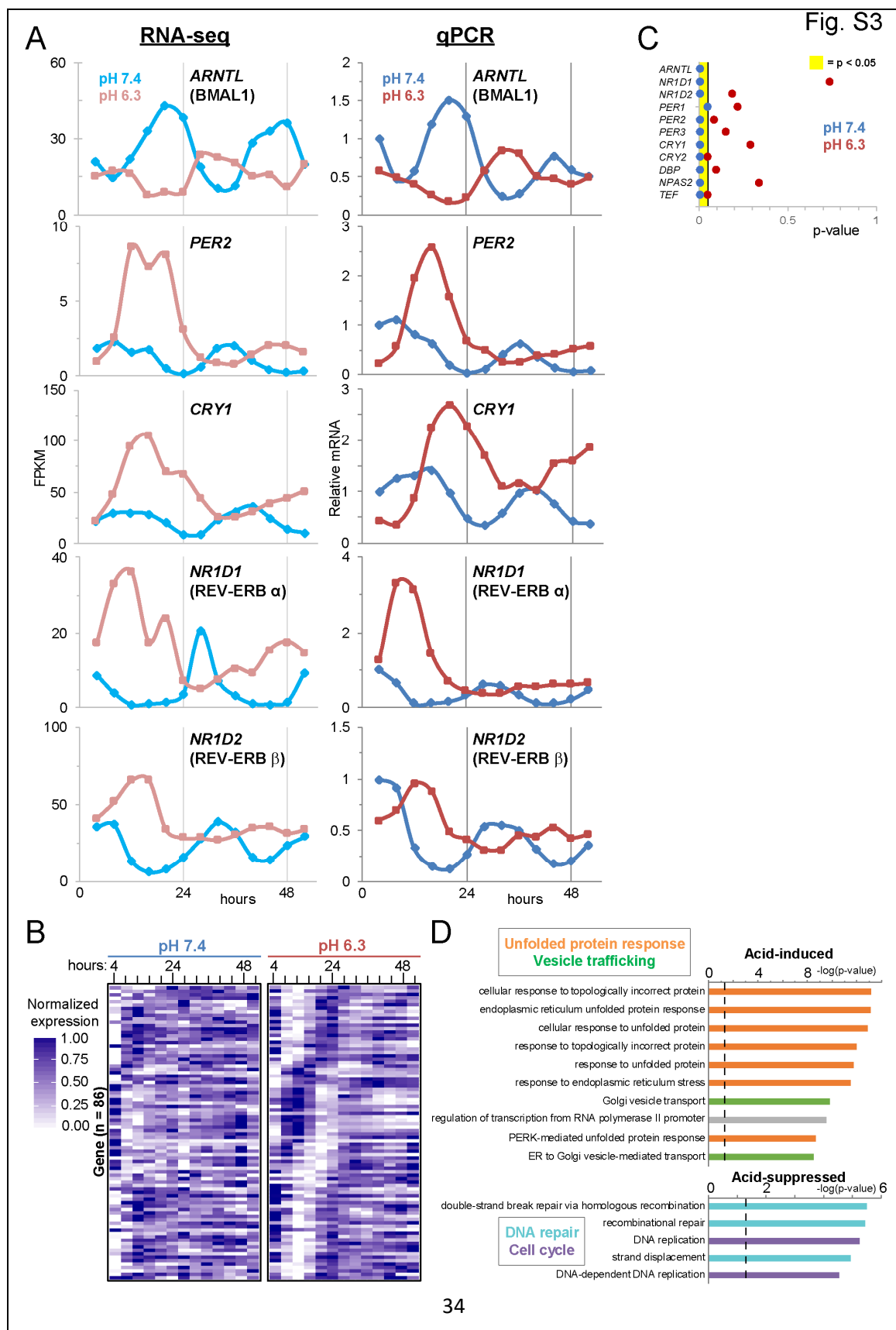


**Figure S3. Transcriptomic analyses reveal loss of oscillation of the core clock and its outputs during acid stress. Related to Figure 3**

**A.** Expression of representative core clock genes over the 52-hour timecourse in pH 7.4 and 6.3 as determined by RNA-sequencing (RNA-seq) (left) versus real-time polymerase chain reaction (qPCR) (right, data also appear in 2D) of RNA collected as described in 3A. RNA-seq reported as fragments per kilobase of transcript per million mapped reads (FPKM). **B.** Expression in pH 7.4 and 6.3 of the 86 protein-coding genes with statistically significant circadian oscillation in pH 6.3 (3B) ( $p < 0.05$ , false discovery rate (FDR)  $< 0.2$ ) ordered by phase. Color scale as in 3A. **C.** p-value statistic of test for circadian rhythmicity of expression (as in 3A) for core and secondary feedback loop clock genes and representative clock paralogs (*NPAS2*) and output regulators (*DBP*, *TEF*) in pH 7.4 or 6.3. **D.** Most highly significant biological process ontologies represented in the 571 acid-induced and 859 acid-suppressed transcripts (defined in 3E) with terms related to unfolded protein response, vesicle trafficking, DNA repair, and cell cycle colored as shown.  $p < 0.05$  above the dashed line. For pH 6.3, all ontologies with B&H q-value  $< 0.05$  shown; for pH 7.4, the top 10 ontologies are shown ( $q < 1 \times 10^{-5}$ ).

## Low pH inhibits translation and thereby the clock

To delineate the mechanism by which hypoxia-generated acid suppresses the clock, we first determined how extracellular pH ( $\text{pH}_e$ ) and DMOG affect intracellular pH ( $\text{pH}_i$ ). We generated a U2OS cell line stably expressing a cytoplasmic pH probe consisting of pH-insensitive mCherry fused to pH-sensitive GFP (SuperEcliptic (SE) pHluorin) (Koivusalo et al., 2010). Using a  $\text{pH}_i$  standard curve generated with ionophores (S4A, S4B), we concluded that  $\text{pH}_i$  fell in cells exposed to acidic media or DMOG (4A, S4C), in accord with findings of others (McBrian et al., 2013; Pouyssegur et al., 1985). Consistent with  $\text{pH}_i$  acidification driving clock collapse, two inhibitors of hydrogen ion efflux pathways, amiloride (which inhibits sodium-hydrogen antiporter 1 (NHE1) among other exchangers) and  $\alpha$ -cyano-4-hydroxycinnamate (a monocarboxylate transporter 1 inhibitor) lowered intracellular pH (S4E) (Koivusalo et al., 2010; McBrian et al., 2013) and reversibly suppressed circadian oscillation of *Arntl::dLUC* (S4D).

Because acid profoundly disrupted transcript levels of clock network components, we assessed their protein levels. Indeed, hypoxia decreased PER2 and BMAL1 amplitudes in a manner rescuable by highly buffered media (4B). However, this rapid and durable protein-level suppression was unexpected given its divergence from RNA-level distortions previously noted in hypoxia, where *ARNTL* transcript was suppressed but *PER2* transcript was induced (S2F). To clarify these surprising results, we examined BMAL1 and PER2 protein levels over 48 hours at four-hour resolution and confirmed suppressed protein levels and oscillation in hypoxia when the media was of low buffering capacity (4C, 4G). Exposure to acidic media was sufficient to recapitulate this rapid and durable suppression (4D, 4G). Similar suppression of CLOCK protein level was also noted in both hypoxic low buffer media and acidic media (S4F). Consistent with acidification downstream of HIF suppressing clock network protein levels and thereby

molecular clock oscillation, during low dose DMOG treatment, which initiates gradual acidification (S4I), amplitude of oscillation of both endogenous clock proteins (S4G) and the *Arntl*::dLUC reporter (S4H) remained intact through about 24 hours, after which dampening began in concert with the accumulating acid load.

The rapid and profound protein-level suppression of the clock suggested regulation of protein production or stability might underlie clock collapse. Although acid is reported to activate a kinase of the eukaryotic elongation factor 2 (eEF2K), thereby inhibiting translational elongation in acid (Xie et al., 2015), eEF2K activity was neither detected in nor required for acid-mediated clock collapse (S4J, S4K). In contrast, mTORC1 signaling, a key regulator of translation in response to the cell's nutrient status and growth factor signals (Dibble and Manning, 2013; Saxton and Sabatini, 2017), was profoundly inhibited in acidic conditions arising from HIF stabilization by hypoxia or DMOG, as indicated by the reduction in phosphorylation of downstream components: ribosomal protein S6 and its kinase (S6K) and eukaryotic translation initiation factor 4E-binding protein 1 (4EBP1) (4E, S4G). Application of acidic media was sufficient to inhibit mTORC1 signaling (4F), while highly buffered media rescued mTORC1 signaling from suppression by hypoxia or DMOG treatment in association with rescue of levels of representative clock proteins (PER2, CRY2) (4H). This ability of acid to suppress mTORC1 signaling, previously seen by others (Balgi et al., 2011; Chambard and Pouyssegur, 1986), was observed in all other cell lines studied: 293T, MDA-MB-231, MEFs, HCT116, MCF7 (S4L, S5F, S7J, S7K).

Consistent with mTORC1 inhibition causing clock suppression, we found that inhibitors of mTORC1 dampened *Arntl*::dLUC oscillation in proportion to their efficacy. For example, the active-site inhibitors Torin1 and Torin2 or *n*-butanol, which depletes phosphatidic acid required for mTORC1 activity (Toschi et al., 2009), durably

suppressed mTORC1 signaling (4K, S4M, S4P) and the amplitude of the circadian reporter (4I, 4J, S4N, S4O, S4Q). Rapamycin, an allosteric mTOR inhibitor, only partially reduced clock amplitude, consistent with its inability to significantly suppress phosphorylation of 4EBP1 (a well-recognized limitation of this agent (Saxton and Sabatini, 2017)) and the rapid partial rebound of phosphorylation of S6 (S4R).

To determine whether alleviating the sequestration of translation initiation factor eIF4E by 4EBPs could restore the clock in acid or DMOG, we knocked down (4L) or out (4M, 4N, S4S) individual 4EBPs. As anticipated given the multiplicity of 4EBP proteins and unresolved S6K inhibition, these approaches yielded partial rescue of clock protein levels (S4S) and clock oscillation (4L, 4M, 4N) in both acidic media and DMOG exposure. Interestingly, while 4EBP1 deletion initially rescued high amplitude oscillation in DMOG, these cells quickly began to die, perhaps consistent with the notion that high amplitude clock oscillation is untenable for a cell confronted with acid stress while sustaining itself on a limited (hypoxic) metabolic program (4M).

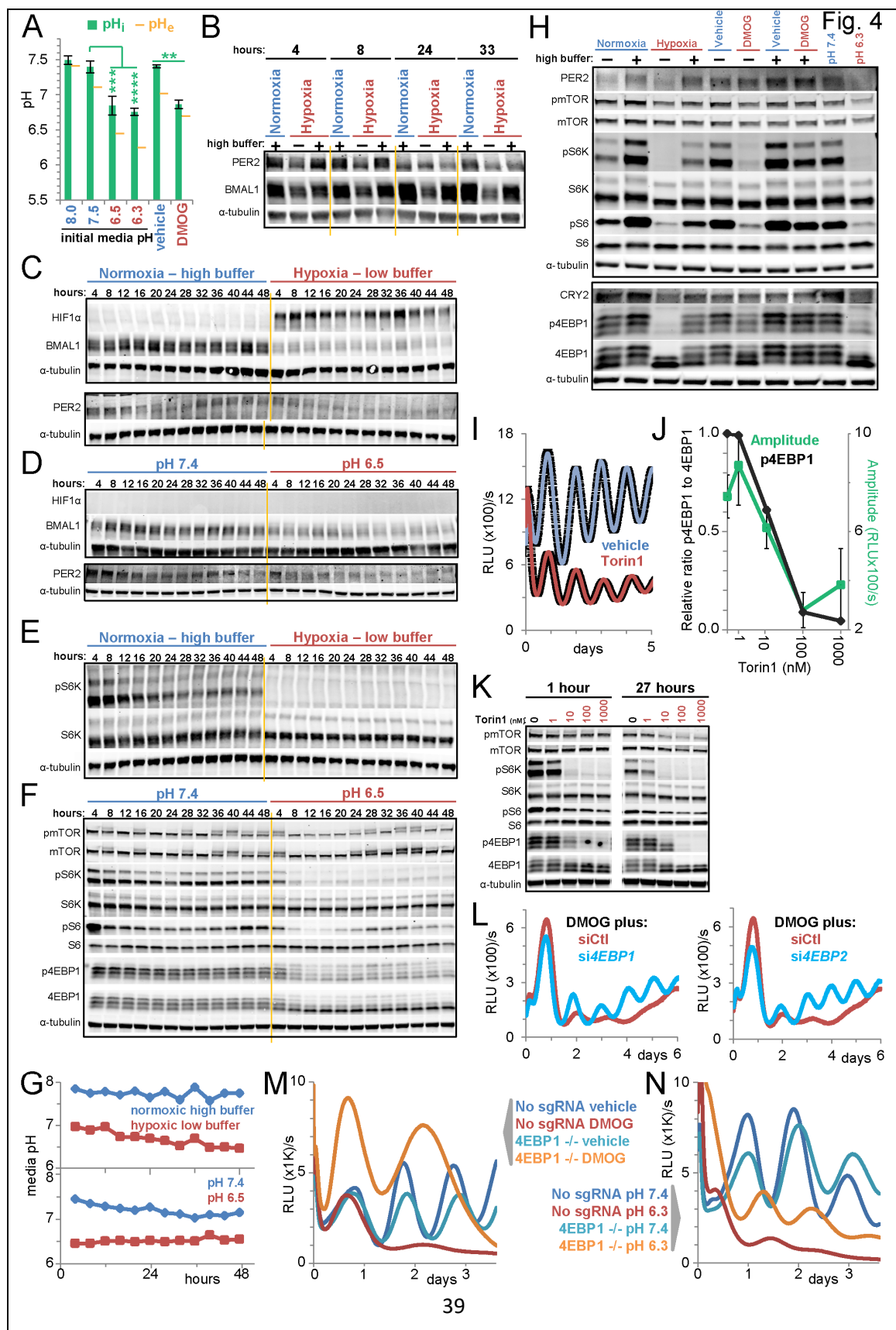


**Figure 4 – Acid suspends the circadian clock through inhibition of mTORC1.**

**A.** Intracellular pH ( $\text{pH}_i$ ) of U2OS cells as measured by ratiometric pH probe mCherry-SEpHluorin after incubation in media of the indicated pH or treated with vehicle or 500  $\mu\text{M}$  DMOG in low buffer conditions for 24 hours. Extracellular pH ( $\text{pH}_e$ ) recorded from the same cells after 33 hours treatment also shown.  $\text{pH}_i \pm$  standard deviation (SD) derived from three or more 10x fields per condition (S4C) using a standard curve (as in S4A) generated in parallel. T-tests (unpaired, two-tailed, unequal variances) of  $\text{pH}_i$  \*\*\*\* $p \leq 0.0001$ , \*\*\* $p \leq 0.001$ , \*\* $p \leq 0.01$ . RE of 2-3 per condition. **B.** Immunoblots of core clock proteins using lysate from U2OS cells grown in normoxic high buffer or hypoxic (1%  $\text{O}_2$ , media pre-deoxygenated) low or high buffer conditions. **C/D.** Immunoblots for HIF1 $\alpha$  and the indicated clock proteins from U2OS cells as in B (C) or in media of pH 7.4 or 6.5 (D). **E/F.** Immunoblots of lysate collected in C (E) and D (F) using antibodies specific to phosphorylated sites (Ser2448 (mTOR), Thr389 (S6K), Ser235/236(S6), Thr37/46(4EBP1)) or total levels of mTORC1 substrates and downstream signaling components. Tubulin shared by E, C. **G.** Media pH over the 48-hours shown in C-F. **H.** Immunoblots for core clock proteins and mTORC1-signaling components using lysate from U2OS cells in normoxia or hypoxia (1%  $\text{O}_2$ , media pre-deoxygenated) or treated with vehicle or 300  $\mu\text{M}$  DMOG in low or high buffer conditions or exposed to media of pH 7.4 or 6.3 for 8 hours. **I.** Luminescence of U2OS *Arntl::dLUC* cells treated with vehicle or 100 nM Torin1. Mean $\pm$ SEM of 3 BR. RE of 2. **J.** Normalized ratio of the intensities of p4EBP1 to total 4EBP1 at 27 hours (quantified from K) and the mean $\pm$ SEM amplitude over 4 days (calculated from the mean of 3 BR as in I) both as a function of Torin1 dose. Y-axis scaled as  $\log([\text{Torin}] + 1)$ . **K.** Immunoblot for mTORC1 signaling using U2OS cell lysate collected after 1 and 27 hours of treatment with

vehicle or 1-1000 nM Torin1. Unrelated intervening lanes cropped. **L.** Luminescence of U2OS *Arntl*::dLUC cells treated with 10 nM non-targeting control (siCtl) siRNA or siRNA against *EIF4EBP1* (4EBP1) or *EIF4EBP2* (4EBP2) prior to treatment with 300 uM DMOG in low buffer media. Mean of 2 BR. RE of 2. **M/N.** Luminescence of U2OS *Arntl*::dLUC *EIF4EBP1* CRISPR knockout (4EBP1 <sup>-/-</sup>) and editing control (no sgRNA) clonal lines treated with vehicle or 500 uM DMOG in low buffer conditions (M) or media of pH 7.4 or 6.3 (N). Mean of 2-3 BR. RE of  $\geq 3$ . Black rectangles enclose immunoblots from same gel. Yellow lines for readability only. All cells synchronized at time 0 except A, K. RE = representative experiment. BR = biological replicates. See also Figure S4.

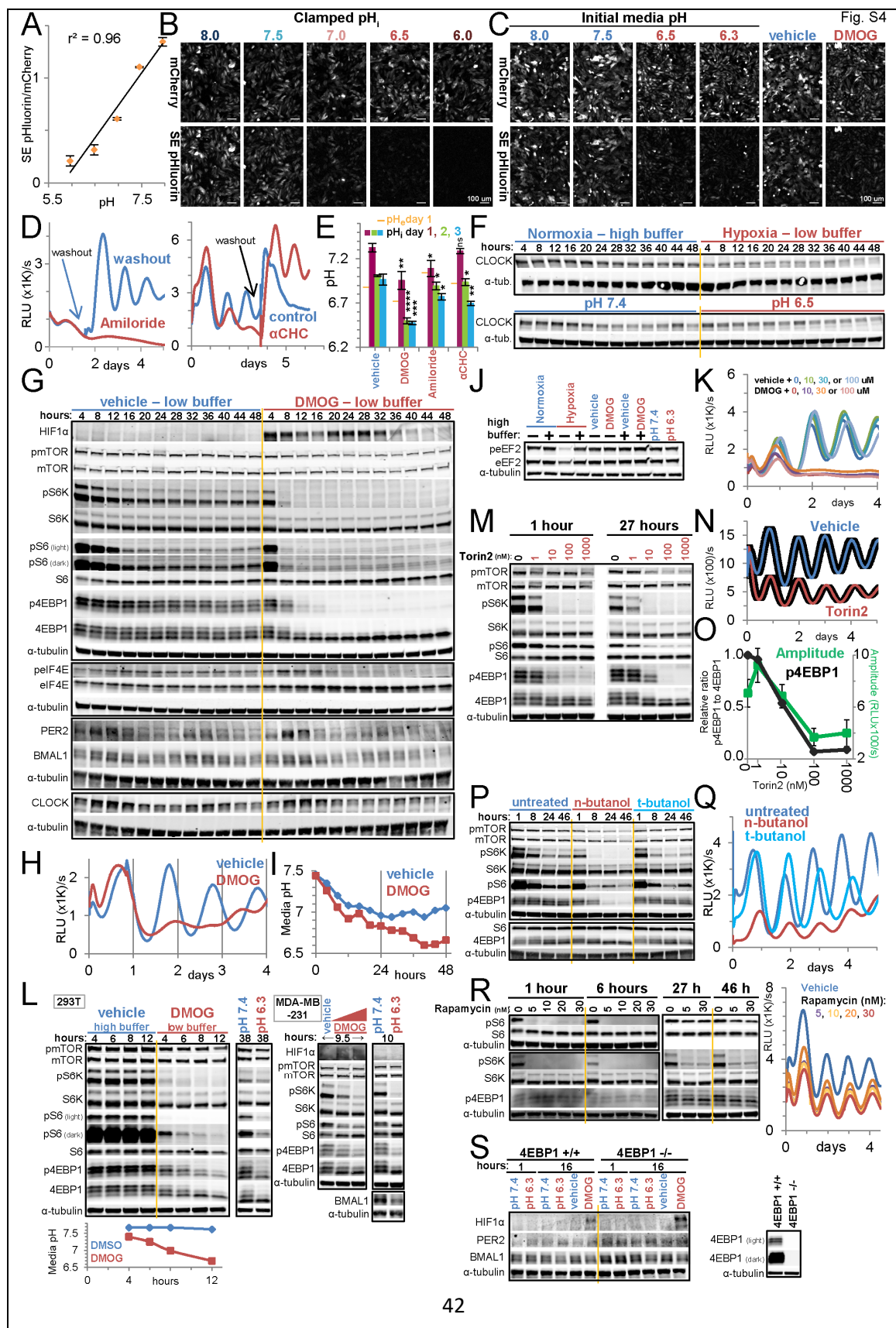


**Figure S4. mTORC1 inhibition mediates suppression of the circadian clock by acid. Related to Figure 4**

**A.** Representative standard curve and linear best-fit equation relating the ratiometric signal of the cytoplasmic pH probe mCherry-SEpHluorin to intracellular pH ( $\text{pH}_i$ ) generated by incubating U2OS cells stably expressing the construct in media of pH 6.0-8.0 containing ionophores that cause  $\text{pH}_i$  to equilibrate with extracellular pH ( $\text{pH}_e$ ). Data presented as mean  $\pm$  standard deviation (SD) of the ratios of the intensities of the SEpHluorin and mCherry signals across an entire 10x field for three or more fields per pH standard. Representative experiment of >6. **B.** Representative 10x fields upon which A was generated. **C.** Representative 10x fields upon which 4A was generated. **D.** Real-time luminescence monitoring of U2OS *Arntl::dLUC* cells synchronized and treated with vehicle or 200  $\mu\text{M}$  amiloride (left) or 250  $\mu\text{M}$   $\alpha$ -cyano-4-hydroxycinnamate (right). At the indicated times, treatment was washed out by media change. Representative experiments of  $\geq 3$ . **E.** Timecourse of  $\text{pH}_i$  of U2OS cells over three days of treatment with vehicle, 500  $\mu\text{M}$  DMOG, 200  $\mu\text{M}$  amiloride or 250  $\mu\text{M}$   $\alpha\text{CHC}$ . Day 1  $\text{pH}_e$  also indicated for reference (orange line).  $\text{pH}_i \pm \text{SD}$  derived from three or more 10x fields as in A. Student's T-tests (unpaired, two-tailed, equal variances) comparing treatment to vehicle at same time point. \* $p \leq 0.05$ , \*\* $p \leq 0.01$ , \*\*\* $p \leq 0.001$ , \*\*\*\* $p \leq 0.0001$ , ns =  $p > 0.05$ . Representative experiment of 3. **F.** Immunoblots for CLOCK using lysate collected in 4C and 4D. Tubulin loading controls shared with 4C and 4F. **G.** Immunoblots for HIF1 $\alpha$  and the indicated mTORC1-signaling components using lysate collected from U2OS cells every 4 hours for 48 hours after synchronization and treatment with vehicle or 300  $\mu\text{M}$  DMOG in low buffer media. Ser209 (EIF4E). **H.** Real-time luminescence monitoring of U2OS *Arntl::dLUC* cells

treated in parallel to the timecourse in G. Representative of 2. **I.** Media pH during G. **J.** Immunoblot for phosphorylation of Thr56 of eEF2 using U2OS cell lysate collected 8 hours after synchronization and placement in normoxia or hypoxia (1% O<sub>2</sub>, media pre-deoxygenated), or treatment with vehicle or 300 uM DMOG in low or high buffer media, or exposure to media of pH 7.4 or 6.3. Tubulin control shared with blots in 4H. **K.** Real-time luminescence monitoring of U2OS *Arntl*::dLUC cells synchronized and treated with vehicle or 300 uM DMOG and 0-100 uM A-484954 (eEF2K inhibitor) in low buffer media. Mean of triplicates. Similar results seen with A-484954 treatment of cells in media of pH 7.4 and 6.3 (not shown). **L.** Immunoblots for the indicated mTORC1 signaling or clock components using lysate collected periodically from 293T (left) or synchronized MDA-MB-231 cells (right) treated with 500 (293T) or 500 and 1000 (MDA-MB-231) uM DMOG in low buffer conditions or exposed to acidic media. Representative experiment of ≥3 each condition. Vehicle control in high (293T) or low (MDA-MB-231) buffer media. Bottom panel indicates media pH at the time of lysate collection in 293T cells. **M.** Immunoblot for mTORC1 signaling using lysate collected from U2OS cells after 1 and 27 hours of treatment with vehicle or 1-1000 nM Torin2. All lanes from same gel with intervening lanes cropped for space. **N.** Real-time luminescence monitoring of U2OS *Arntl*::dLUC cells synchronized and treated with vehicle or 100 nM Torin2. Mean ± SEM of cells plated in triplicate. Representative experiment of 2. **O.** Normalized ratio of the background-corrected intensities of p4EBP1 to total 4EBP1 at 27 hours (quantified from M) and the average amplitude (± SEM) over 4 days (beginning 1 day after synchronization and based upon the mean profile of biological triplicates as in N) both as a function of Torin2 dose. Y-axis scaled as  $\log([\text{Torin}] + 1)$ . **P.** Immunoblots for mTORC1 signaling using lysate collected

periodically over 2 days from U2OS cells synchronized and either left untreated or treated with 0.4% of the primary alcohol *n*-butanol to deplete phosphatidic acid or control treated with the non-phosphatidyl-reactive tertiary alcohol *tert*-butanol (see Methods). **Q.** Real-time luminescence monitoring of U2OS *Arntl*::dLUC cells treated in parallel to P. Representative experiment of 4 each with 1-3 biological replicates and with additional arms not shown revealing dose-dependent effects of 0.2-0.6% *n*-butanol treatment. **R.** Immunoblots (left) for mTORC1 signaling using lysate collected from synchronized U2OS cells after treatment with vehicle or 5-30 nM rapamycin for 1, 6, 27, or 46 hours in two independent experiments. *Right:* Real-time luminescence monitoring of U2OS *Arntl*::dLUC cells synchronized and treated with vehicle or 5-30 nM rapamycin. Mean of cells plated in triplicate. **S.** Immunoblots for HIF1 $\alpha$  and indicated clock network proteins (left) or 4EBP1 (right) using lysate collected from unsynchronized (no dexamethasone) *Arntl*::dLUC *EIF4EBP1* (4EBP1) CRISPR knockout or parental *Arntl*::dLUC U2OS cells after 1 or 16 hours of exposure to media of pH 7.4 or 6.3 or treatment with vehicle or 500  $\mu$ M DMOG in low buffer media. Black rectangles enclose immunoblots from same gel. Yellow lines for readability only.

## **Acid inhibits mTORC1 signaling independently of both amino acid sensing and TSC2**

mTORC1 activity requires sensing of both growth factors and amino acids (predominantly, leucine and arginine) through pathways converging on Ras homolog enriched in brain (RHEB) and Ras-related (RAG) GTP binding proteins, respectively, with neither pathway alone sufficient for activation (Saxton and Sabatini, 2017). Acidic media blunted activation of mTORC1 in response to stimulation with either serum (growth factors) (5A) or leucine and arginine (5B), consistent with acid inhibiting signals through either of these requisite pathways. The binding of leucine by sestrins upstream of RAG GTP-binding proteins relies on a histidine residue in a lid-latch mechanism (Saxton et al., 2016). Given the near-neutral pKa of histidine, we wondered if protonation of this residue might disable leucine sensing and render mTORC1 inactive. Knockdown of leucine-sensing mTORC1-inhibiting sestrin-1 and sestrin-2, but not the leucine-insensitive sestrin-3 (Wolfson et al., 2016), weakly rescued both mTORC1 signaling and clock reporter oscillation in HIF-generated acidic conditions (S5A, S5B). However, leucine-triggered dissociation of sestrin2 from GATOR2 component WDR24 (S5C) was pH insensitive (S5D), suggesting acid did not block leucine sensing. Moreover, cells in which all three sestrin proteins are deleted (Saxton et al., 2016) remained sensitive to the mTORC1-suppressive effects of acid (S5E). Further, U2OS cells stably expressing constitutively GTP-bound RAGB were generated, rendering mTORC1 signaling independent of amino acids as anticipated (5C) (Sancak et al., 2008), but these cells likewise remained sensitive to the inhibitory effects of HIF-generated acid on mTORC1 signaling (5D) and clock oscillation (5E), refuting the hypothesis that acid hinders amino acid sensing.

We therefore suspected that acid instead suppressed signaling to RHEB through activation of tuberous sclerosis 2 (TSC2), the GTPase-activating protein (GAP) for RHEB. Consistent with this hypothesis, both in TSC2 null MEFs (S5F) (Zhang et al., 2003) and U2OS cells with TSC2 knockdown (S5G) or CRISPR deletion of TSC2 (5F), significant rescue of mTORC1 signaling was seen both in directly acidified media or media acidified downstream of stabilization of HIF. However, this rescue of mTORC1 activation was incomplete (best appreciated with quantification shown in 5G) and did not fully maintain clock amplitude in acidic media (S5H). Furthermore, when we queried upstream regulators of TSC2 (Dibble and Manning, 2013; Saxton and Sabatini, 2017) over 48-hour timecourses, we found no evidence for TSC2 activation by AMPK or GSK3B activation or ERK inhibition (S5I, S5J, S5K, S5L). Similarly, although regulated in development and DNA damage responses (REDD1/*DDIT4*), a HIF target, can stimulate TSC2 (Dibble and Manning, 2013), REDD1 did not appear to activate TSC2 in acid, as REDD1 induction by acid was modest (S5M, S5N, S5O) and much weaker than that in response to HIF stabilization in highly buffered media (S5O), a condition where mTORC1 signaling was preserved.

Absence of evidence indicative of TSC2 activation by acid and only partial rescue by TSC2 knockout suggested that acid inhibited mTORC1 through TSC2-independent means. We further tested this hypothesis in a distinct cellular context. T cells encounter low pH in the tumor microenvironment and require mTORC1 signaling for differentiation and activation of effector cells (Delgoffe et al., 2011; Pollizzi et al., 2015). Remarkably, acidic media blunted mTORC1 activation in both CD4<sup>+</sup> and CD8<sup>+</sup> primary T cells in response to stimulation *in vitro* (5H). Intriguingly, T cells, like cancer cells, demonstrated a TSC2-independence in the ability of acid to suppress mTORC1.

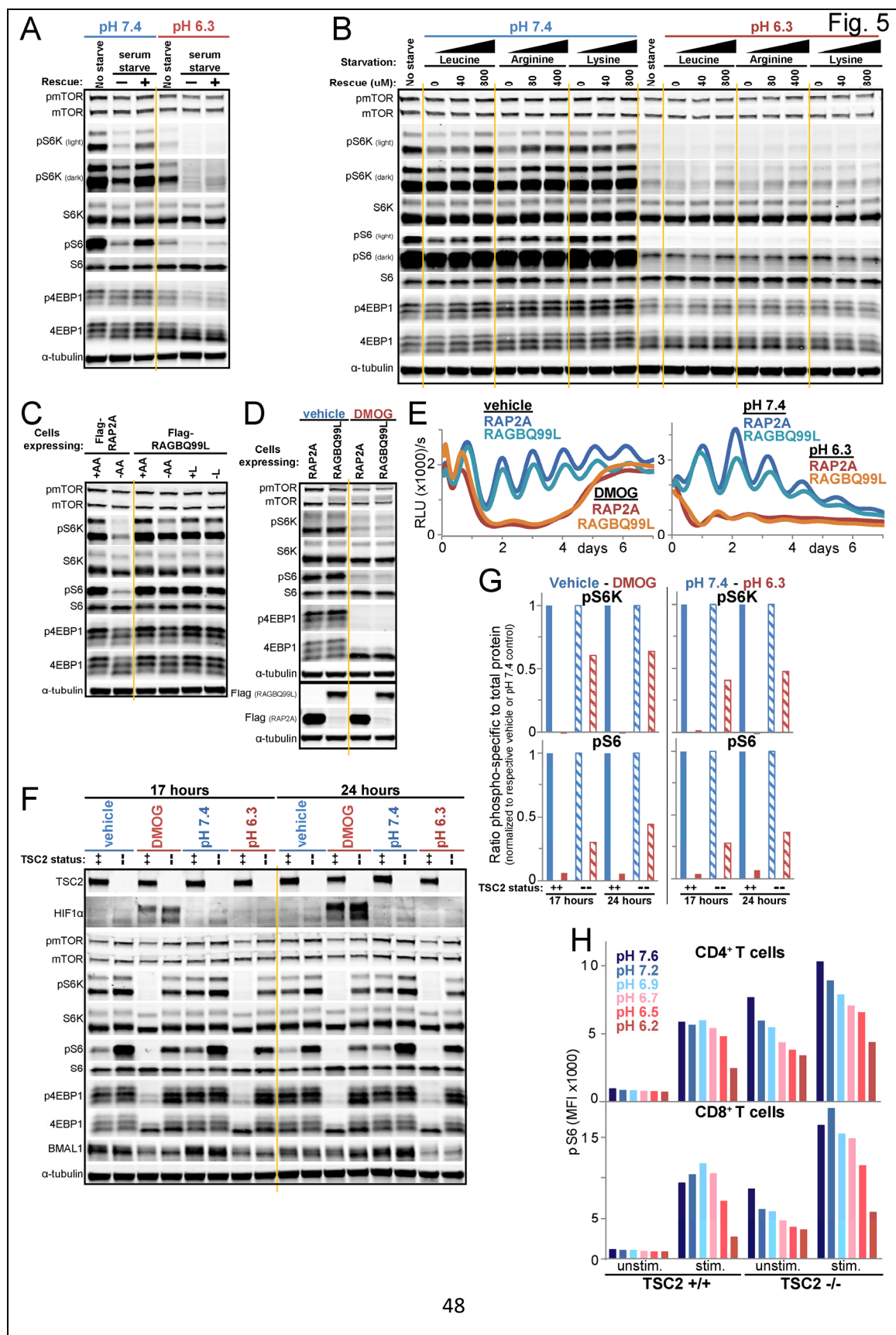


**Figure 5 – Acid inhibits mTORC1 and the clock in a RAG-independent manner not fully rescuable by TSC2 loss.**

**A./B.** Immunoblots for mTORC1 signaling using lysate from U2OS cells unstarved or starved of serum for 50 minutes in pH 7.4 or 6.3 and then rescued or not for 10 minutes with 10% undialyzed serum (A), or unstarved or starved of leucine, arginine, or lysine for 50 minutes in pH 7.4 or 6.3 and then either rescued or not for 10 minutes with the indicated concentrations of the missing amino acid (approximately twice the reported sensor Kd (Wolfson and Sabatini, 2017) and full DMEM level) in the same pH. 10% dialyzed serum throughout (B). **C.** Immunoblots for mTORC1 signaling in U2OS *Arntl::dLUC* cells stably expressing RAP2A or RAGBQ99L after 1 hour of near-complete amino acid (AA) or leucine (L) starvation or incubation in media with AA or L added back. All media pH 7.4 with 5% undialyzed serum. **D.** Immunoblots of lysate from cell lines in C 23 hours after synchronization and treatment with vehicle or 500 uM DMOG in low buffer (replete AA) media. **E.** Luminescence of the *Arntl::dLUC* reporter in parallel to D. 3 BR. **F.** Immunoblots for HIF1 $\alpha$ , mTORC1 signaling, and BMAL1 using lysate from *Arntl::dLUC* TSC2 CRISPR knockout (TSC2<sup>-/-</sup>) or parental *Arntl::dLUC* U2OS cells (++) following treatment with vehicle or 500 uM DMOG in low buffer media or exposure to media of pH 7.4 or 6.3 for 17 and 24 hours. RE of 2. **G.** Quantification of F. Ratio of the intensity of pS6K or pS6 to total S6K or S6, respectively. Each control-treatment pair normalized to respective control (vehicle, pH 7.4). **H.** Mean fluorescence intensity (MFI) of pS6 staining of wildtype (+/+) and TSC2 knockout (-/-) CD4<sup>+</sup> and CD8<sup>+</sup> T cells assessed by flow cytometry after TCR stimulation for 1 hour in media of the indicated pH. RE of 5 each with 1-4 BR.

RE=representative experiment, BR=biological replicates. See also Figure S5.

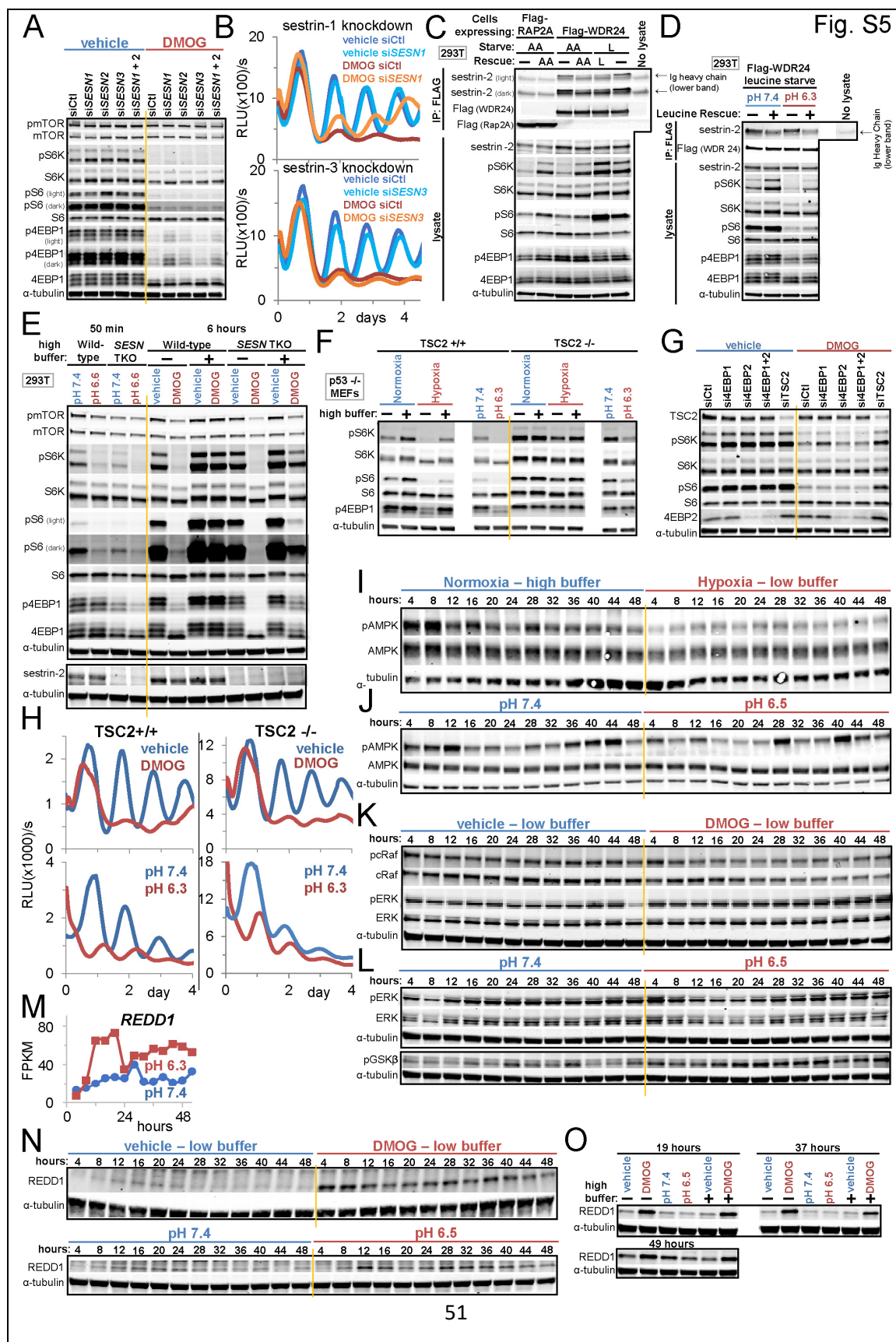


**Figure S5. Disruption of the clock by acid is independent of amino acid sensing and TSC2 activation. Related to Figure 5**

**A.** Immunoblot for mTORC1 signaling using lysate collected from U2OS cells treated with 5 nM non-targeting control (siCtl) siRNA or siRNA against transcripts encoding leucine-sensing Sestrins (SESN1, SESN2) or the non-leucine sensing SESN3 prior to synchronization and treatment with vehicle or 500 uM DMOG in low buffer media for 20 hours. 2.5 nM siRNA each when two oligos used. **B.** Real-time luminescence monitoring of *Arntl::dLUC* U2OS cells treated with 2 nM non-targeting control (siCtl) siRNA or siRNA against *SESN1* or *SESN3* prior to synchronization and treatment with 500 uM DMOG in low buffer media. Representative experiment of  $\geq 4$  with 1-3 biological replicates per condition. **C.** Immunoblot for Sestrin-2 following immunoprecipitation of FLAG-tagged proteins from lysate collected from 293T cells stably expressing Flag-tagged Rap2A (control protein) or WDR24 (a component of the GATOR2 complex) and near-starved of all amino acids (AA) or leucine (L) for 50 minutes (pH 7.4) prior to rescue with AA/L or continued starvation for 10 minutes. Lysate was additionally immunoblotted for components of mTORC1 signaling. (Starvation media base contained no AA/L but was supplemented with 5% undialyzed serum.) Note Ig heavy chain runs just below Sestrin-2. **D.** Immunoblots of immunoprecipitated proteins and lysate as in C using lysate collected from Flag-WDR24 293T cells near-starved of leucine for 50 min in pH 7.4 or 6.3 prior to 10 minutes of leucine rescue or continued starvation (in same pH). An additional independent experiment generated similar results after 14 hours of acid exposure. **E.** Immunoblot for mTORC1 signaling using lysate collected from wild-type or *SESN* triple knockout (*SESN* TKO, where all three *SESN* genes have been silenced by

CRISPR editing) 293T cells after exposure to media of pH 7.4 or 6.6 for 50 minutes or treatment with vehicle or 1mM DMOG in low buffer media for 6 hours. **F.** Immunoblot for mTORC1 signaling using lysate collected from wild-type (+/+) or TSC2 null (-/-) mouse embryonic fibroblasts (MEFS) (both p53 null) after 8 hours of exposure to normoxic or hypoxic (1% O<sub>2</sub>, pre-deoxygenated media) low or high buffer media or media of pH 7.4 or 6.3. Unrelated intervening lanes cropped. **G.** Immunoblot for mTORC1 signaling using lysate collected from U2OS cells treated with 10 nM non-targeting, *EIF4EBP*, or *TSC2* siRNA prior to treatment with vehicle or 300 uM DMOG treatment in low buffer media for 14 hours. **H.** Real-time luminescence monitoring of the *Arntl::dLUC* reporter monitored continuously in parallel to 5F. Mean of biological duplicates. Representative experiment of 3 each with 2-3 biological replicates. **I./J.** Immunoblots for phosphorylated (Thr172) and total AMPK using lysate collected every 4 hours for 48 hours from synchronized U2OS cells in normoxic high buffer or hypoxic low buffer media (I) or in media of pH 7.4 or 6.5 (J). AMP-activated protein kinase (AMPK) was inactivated (dephosphorylated) in acidic conditions. Two additional independent experiments encompassing 8, 19, 37, 49, and 66-hour time points confirmed reduced pAMPK in pH 6.5 or DMOG low buffer conditions. **K/L.** Immunoblots for phosphorylated cRaf (Ser338), ERK (Thr202/Tyr204), and GSK3 $\beta$  (Ser9) using lysate collected every 4 hours for 48 hours from synchronized U2OS cells treated with vehicle or 300 uM DMOG in low buffer media (K) or in media of pH 7.4 or 6.5 (L). Although phosphorylation of c-Raf was suppressed in DMOG treatment, the downstream extracellular signal-regulated kinase (ERK/MAPK) was not suppressed in either DMOG or acidic media. Dephosphorylation indicative of activation of glycogen synthase kinase 3 beta (GSK3B), a TSC2-activating kinase, was unapparent in acidic

conditions (L). **M.** Expression of *DDIT4* (REDD1) in media of pH 6.3 and 7.4 over a 52-hour timecourse as determined by RNA-seq of RNA collected every 4 hours. Reported as FPKM as in S1H. Note REDD2 (DDIT4L) was not expressed (undetectable by RNA-seq). **N/O.** Immunoblots for REDD1 using lysate collected every 4 hours for 48 hours from synchronized U2OS cells treated with vehicle or 300 uM DMOG in low buffer media or in media of pH 7.4 or 6.5 (N). Additional immunoblots from an independent experiment using lysate collected at three time points following treatment with vehicle or 500 uM DMOG in low or high buffer media or exposure to media of pH 7.4 or 6.5 (O). Unrelated intervening lanes cropped. Tubulin loading controls in I-L and N shared with corresponding membranes in 4C-D, 4F, S4G, and S7O.

### **Centrifugal redistribution of lysosomes inhibits mTORC1 signaling**

Because TSC2 deletion could not fully rescue mTORC1 signaling and clock oscillation in low pH, we hypothesized that acid might prevent mTOR localization to the lysosomal surface in response to RAG signaling, precluding mTOR activation by lysosome-tethered RHEB. In U2OS cells, as in other cell types (Jongsma et al., 2016), lysosomes predominantly reside in a perinuclear aggregate seen by staining of endogenous lysosomal associated membrane protein 2 (LAMP2) in fixed cells (6A, S6A) or by addition of the fluorescent probe LysoTracker to live cells (6B). mTOR is recruited to this perinuclear lysosomal aggregate in an amino acid-dependent manner (6C, S6B), as reported (Sancak et al., 2008). Startlingly, acidic conditions profoundly disrupted this perinuclear clustering and rapidly and reversibly dispersed lysosomes (LAMP2) throughout the cell (6D, 6E), which imaging of live cells expressing tagged versions of LAMP1 confirmed (6F, S6C). Despite this phenomenon being noted in the literature (Heuser, 1989), its significance remains obscure. As such, we wondered if this scattering of lysosomes in low pH might contribute to mTORC1 silencing and clock suppression by acid.

Lysosomes traffic on microtubules through the action of motor proteins. Correspondingly, the perinuclear lysosome aggregate intimately associated with microtubules, rather than the actin cytoskeleton (S6D), coinciding with a microtubule organizing center (MTOC) (6G, S6E). In acid, the actin and microtubule cytoskeletons remained intact while lysosomes dispersed throughout the cell (6G, S6D, S6E), suggesting lysosomes move peripherally toward the plus ends of microtubules in acid (6H). Indeed, quantification of the radial distribution of nuclear, tubulin, and LAMP2 staining revealed a peak in both LAMP2 and tubulin intensity adjacent to the nuclear envelope in neutral pH. In acidic media, the density of LAMP2 dispersed to distances

farther from the nucleus despite near identical architecture of tubulin (6I). However, mTOR and LAMP2 continued to show high staining coincidence, whether in sustained or more rapid reversals of pH and lysosome spatial distribution (6J, 6K, S6F, S6G, S6H). Indeed, quantification readily revealed the expected amino acid-dependence of mTOR enrichment in the lysosomal compartment but revealed no such pH-dependence (6L).

mTORC1's persistent localization to lysosomes in acid yet diminished activity suggests that centrifugal redistribution of lysosome-bound mTORC1 might be sufficient to disable signaling. To test this hypothesis, we inhibited dynein, which moves cargo toward the nucleus, with Ciliobrevin D (CbD) (Li et al., 2016). Incubation of cells with CbD revealed dispersion of LysoTracker peripherally away from the MTOC (6M). The dimming of the acidophilic LysoTracker dye (6M) yet persistent intensity of GFP-tagged LAMP1 (6N, S6I) is consistent with published reports indicating peripherally localized lysosomes are less acidic (Johnson et al., 2016). Treatment of cells with CbD over a timecourse caused a gradual decrease in mTORC1 signaling (6O) and dampening of clock amplitude (6P) in association with the gradual redistribution of lysosomes (GFP-LAMP1) to the periphery (6N, S6I). Depolymerization of microtubules with nocodazole likewise disrupted the polarized perinuclear aggregate of lysosomes (S6J, S6L) and inhibited mTORC1 signaling (S6K). Reaggregation of lysosomes at later time points was accompanied by reactivation of mTORC1 (S6M, S6N).

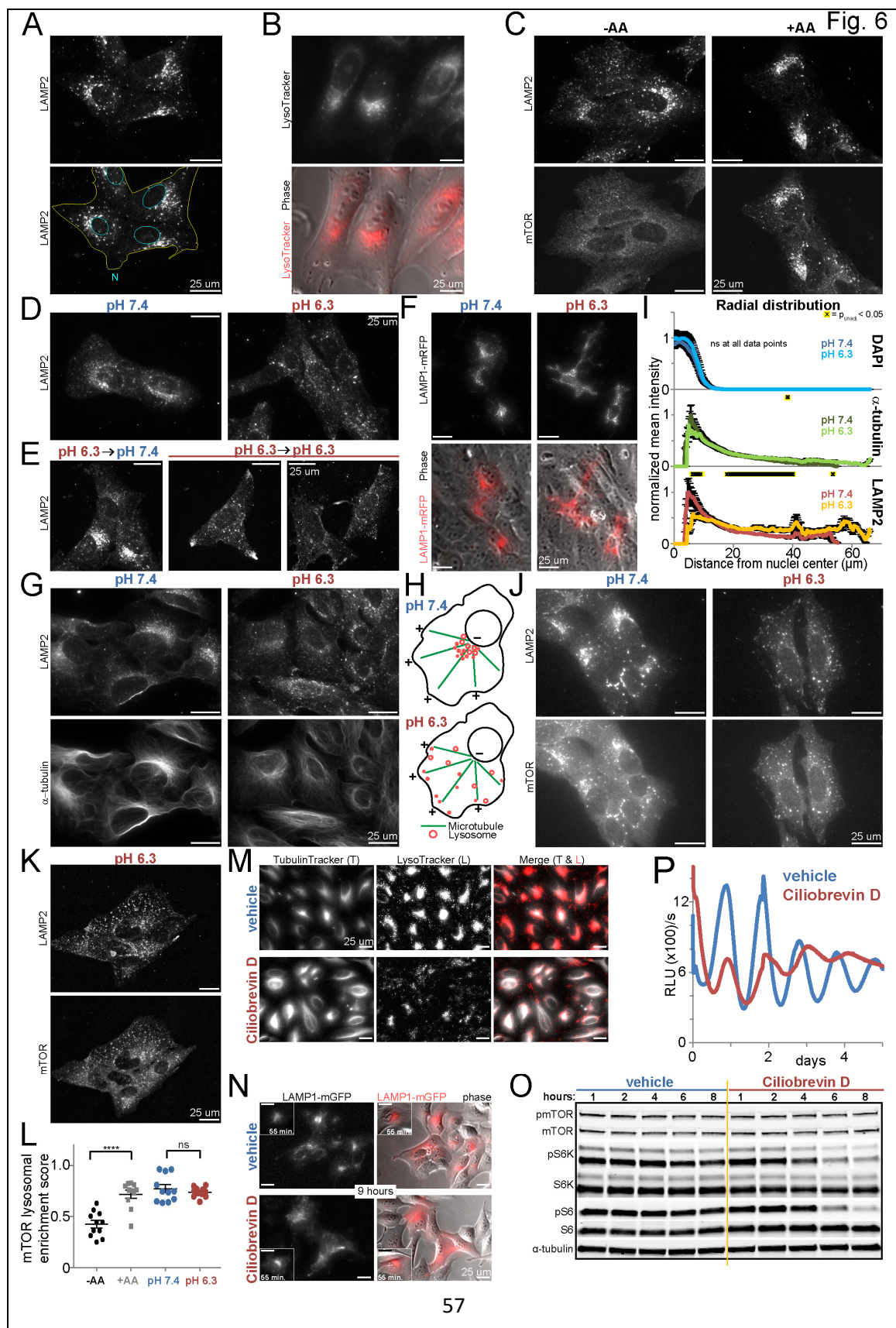


**Figure 6 – Acid causes peripheral redistribution of lysosomes and silencing of lysosome-localized mTORC1.**

**A.** U2OS cells immunostained for lysosomal protein LAMP2. Nuclei and extent of cytoplasm annotated in lower panel. **B.** Live imaging of U2OS cells with lysosomes labeled with LysoTracker. Lower panel merged with phase-contrast image. **C.** U2OS cells immunostained for LAMP2 and mTOR. Cells were starved of amino acids for 115 min and then rescued (+AA) or not (-AA) for 25 min before processing. **D./E.** U2OS cells immunostained for LAMP2 following exposure to media of pH 7.4 or 6.3 for 2.25 hours (D) or following incubation in media of pH 6.3 for 105 min followed by exchange of media for media of pH 7.4 (rescue, left) or 6.3 (mock rescue, right two fields) for 25 min (E). **F.** Live imaging of U2OS cells expressing lysosomal protein LAMP1 fused to mRFP after incubation in media of pH 7.4 or 6.3 for 4 hours. Lower panels: merged mRFP and phase-contrast images. **G.** U2OS cells immunostained for LAMP2 and  $\alpha$ -tubulin following exposure to media of pH 7.4 or 6.3 for 2.25 hours. **H.** Schematic interpreting 6D-G. The typical perinuclear aggregate of lysosomes disperses upon cellular acidification with lysosomes displaced toward the cell periphery (microtubule plus (+) ends). **I.** Mean intensity of DAPI (nuclear stain),  $\alpha$ -tubulin, and LAMP2 as a function of distance from nucleus center (i.e. radial coordinate) after 2.75 hours in media of pH 7.4 and 6.3. n=15 cells each pH. Mean $\pm$ SEM normalized to each channel's maximum. Student's T-test (unpaired, two-tailed, equal variance) unadjusted  $p < 0.05$  (\*) at 0/228, 2/228, and 117/228 radial data points, respectively. Representative images in S6E. **J./K.** U2OS cells immunostained for LAMP2 and mTOR following amino acid starvation for 130 minutes in media of pH 7.4 or 6.3 and subsequent restimulation with amino acids for 10 minutes in the same pH (J), or

following incubation in media of pH 6.3 for 2 hours with media change (same pH) 15 minutes prior to processing (K). **L.** Quantification of mTOR lysosomal enrichment in U2OS cells immunostained for LAMP2 and mTOR following starvation of amino acids for 155 min prior to continued starvation or rescue with amino acids for 10 minutes or following exposure to media of pH 7.4 or 6.3 for 165 min. n =11 fields per condition, encompassing 86, 98, 101, and 93 cells, respectively. Mean±SEM superimposed with raw data. T-tests (unpaired, 2-tailed) \*\*\*\*p<0.0001, ns = p>0.05. Representative of quantifications of two RE from >3 RE. **M.** Live imaging of U2OS cells treated with vehicle or 40 uM ciliobrevin D (dynein inhibitor) for 10.5 hours. Lysosomes and polymerized tubulin labeled with LysoTracker and TubulinTracker. **N.** Live imaging of U2OS cells expressing LAMP1 fused to GFP (pseudocolored red) after treatment with vehicle or 60 uM ciliobrevin D for 55 min (cropped inset) and 9 hours (different fields). Right: merged GFP and phase-contrast images. **O.** Immunoblot for mTORC1 signaling using U2OS cell lysate collected over an 8-hour timecourse of vehicle (veh.) or 40 uM ciliobrevin D treatment. RE of 3. **P.** Luminescence of U2OS *Arntl::dLUC* cells synchronized and treated with 50 uM ciliobrevin D or vehicle. Mean of 2 BR. RE of 2, 2-3 BR each. Representative fields of ≥3 BR for all microscopy. RE = representative experiment. BR = biological replicates. See also Figure S6.

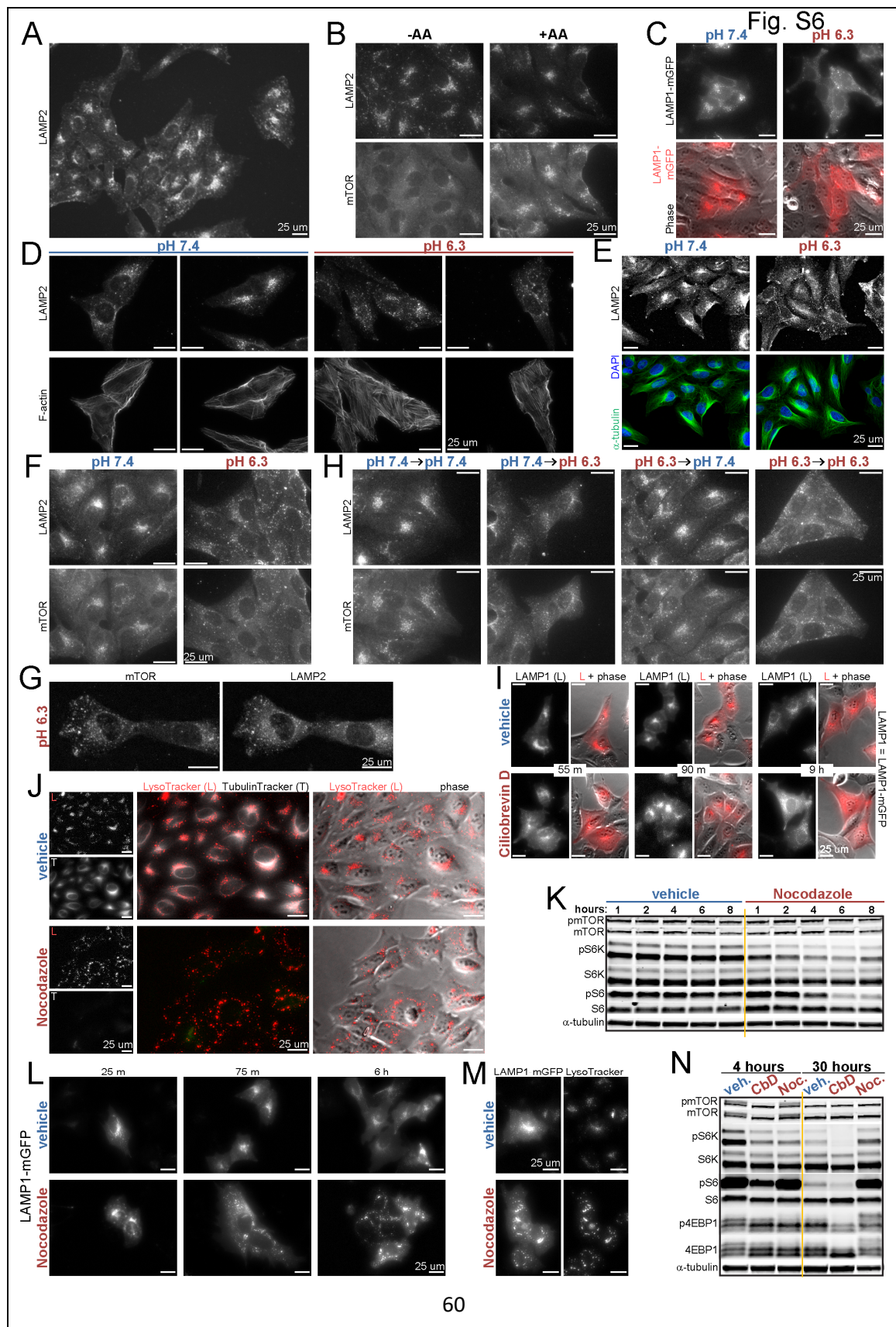


**Figure S6. Spatial dispersion of lysosomes suppresses mTORC1 signaling.**

**Related to Figure 6**

**A.** U2OS cells immunostained for lysosomal protein LAMP2 imaged at lower magnification. Independent replicate experiment of that shown in 6A. **B.** U2OS cells coimmunostained with LAMP2 and mTOR. Cells were starved of amino acids for 140 min followed by rescue (+AA) or not (-AA) with amino acids for 10 min before processing and imaging. Independent experiment from that shown in 6C. **C.** Live imaging of U2OS cells transiently expressing lysosomal protein LAMP1 fused to green fluorescent protein after incubation in media of pH 7.4 or 6.3 for 2.5 hours. Lower panels: merged GFP (pseudocolored red for better visibility) and phase-contrast images. (Heterogeneity in LAMP1 expression owing to variable transfection efficiency). Independent replicate experiment of that shown in 6F using different LAMP1-fusion construct. **D.** U2OS cells coimmunostained for LAMP2 and filamentous (F-) (polymerized) actin following exposure to media of pH 7.4 or 6.3 for 2.25 hours. **E.** U2OS cells coimmunostained for LAMP2, alpha-tubulin, and DAPI (nuclear stain) following exposure to media of pH 7.4 or 6.3 for 2.75 hours. Quantified in 6I. Independent replicate experiment from that shown in 6G. **F.** U2OS cells coimmunostained for LAMP2 and mTOR following incubation in media of pH 7.4 or 6.3 for 2.25 hours. Independent experiment from that shown in 6J. **G.** U2OS cells coimmunostained for LAMP2 and mTOR following incubation in media of pH 6.3 for 120 min. Enlarged to highlight colocalization of LAMP2 and mTOR. Independent replicate experiment of that shown in F. **H.** U2OS cells coimmunostained for LAMP2 and mTOR following incubation in media of the first indicated pH for 105 min followed by 30 min in media of the second indicated pH. **I.** Live imaging of U2OS cells

expressing LAMP1 fused to GFP after treatment with vehicle or 60 uM ciliobrevin D for 55 min, 90 min, and 9 hours. Images on right at each time point show merged GFP and phase-contrast images. Additional fields and time point of 6M. **J.** Live imaging of U2OS cells treated with vehicle or 2 uM nocodazole (tubulin depolymerizing agent) for 6.5 hours. Lysosomes and polymerized tubulin labeled with the acidophilic dye LysoTracker (L) and TubulinTracker (T), respectively, prior to imaging. **K.** Immunoblot for mTORC1 signaling using lysate collected from unsynchronized U2OS cells over an 8-hour timecourse during treatment with vehicle or 2 uM nocodazole. Representative experiment of 3. **L.** Live imaging of U2OS cells expressing LAMP1 fused to GFP after treatment with vehicle or 2 uM nocodazole for 25 min, 75 min, and 6 hours. **M.** Live imaging of U2OS cells expressing LAMP1 fused to GFP after treatment with vehicle or 2 uM nocodazole for 7 hours showing initiation of lysosome reclustering. Lysosomes labeled with LysoTracker prior to imaging to highlight colocalization of signal from both lysosome-labeling techniques for the subset of cells expressing LAMP1-GFP. (Heterogeneity in LAMP1 expression owing to variable transfection efficiency.) **N.** Immunoblot for mTORC1 signaling using lysate collected from unsynchronized U2OS cells after 4 and 30 hours of treatment with vehicle (veh.), 60 uM ciliobrevin D (CbD), or 2 uM nocodazole (Noc.). Representative fields of multiple fields acquired from each of  $\geq 3$  biological replicates. Images visualizing endogenous proteins/lysosomes contrasted uniformly (see Methods).

The influence of lysosome spatial location on mTORC1 signaling is reminiscent of the mechanism by which human cytomegalovirus (HCMV) maintains persistent mTORC1 signaling. HCMV encodes a viral protein, UL38, which inhibits host TSC2 (Moorman et al., 2008). Unlike uninfected cells (6C, S6B), HCMV also bypasses mTORC1's requirement for amino acids by maintaining perinuclear localization of mTORC1 through a dynein-dependent mechanism (Clippinger and Alwine, 2012; Clippinger et al., 2011). As such, we infected cells with HCMV and saw impressive rescue of mTORC1 signaling in both acidic media and in HIF-generated acid (7A). As kinesins oppose dynein and traffic cargo toward the plus (peripheral) end of microtubules, we reasoned inhibition of kinesin motor proteins might also thwart acid-induced peripheral redistribution of lysosomes and rescue signaling. However, antagonism of plus-directed lysosomal trafficking is challenging as there are over 35 kinesins expressed in U2OS cells (S7A, S7B). Nonetheless, we decided to knockdown the most abundantly expressed kinesin, kinesin family member 5B (*KIF5B*), a component of kinesin-1 which has been shown to contribute to lysosome trafficking in other cell types (Li et al., 2016). As anticipated given kinesin redundancies, partial knockdown of kinesin-1 resulted in partial resistance of mTORC1 signaling to suppression by acid with all three siRNAs tested (7B), consistent with acid inhibiting mTORC1 through centrifugal dispersion of lysosomes.

### **Restoration of spatial coincidence of RHEB and lysosome-bound mTORC1 rescues mTORC1 signaling and the clock from acid suppression**

Interestingly, in primary CD8<sup>+</sup> T cells, we noted that the acid-mediated suppression of mTORC1-signaling, previously found to be TSC2-independent (5H), was not associated with loss of mTOR from the lysosomal surface (S7C, S7D). Thus, data from

both U2OS cells (5F, 5G) and primary T cells (5H) indicated that TSC2 deletion was insufficient to fully rescue mTORC1 signaling despite intact amino acid sensing (5D) and persistent localization of mTOR to lysosomes in acid (6L, S7D). We therefore wondered if the unified explanation might be that peripheral redistribution of lysosomes in acid limits the ability of RHEB to activate lysosome-bound mTOR (7C), explaining why TSC2 deletion could enhance but not fully rescue mTORC1 activity. Consistent with this model, dynein inhibition reduced mTORC1 signaling in TSC2 knockout cells despite the expected higher basal level of mTORC1 signaling in these cells (7D). More precisely, we wondered whether contact between RHEB and mTOR might be affected by spatial redistributions driven by acid. After validating an anti-RHEB antibody (S7E-G), we coimmunostained for mTOR, LAMP1, RHEB, and nuclei and observed, consistent with others (Menon et al., 2014), that RHEB is enriched in a perinuclear location similar to that of lysosomes (7E-F) irrespective of amino acid status (S7H). In response to amino acids, mTOR is recruited to lysosomes (S7H), allowing RHEB and mTOR to interact. Remarkably, in acid, RHEB retained its perinuclear niche while lysosomes with bound mTOR redistributed to the periphery (7E-F). Indeed, quantification of the radial distribution of nuclear, RHEB, LAMP1, and mTOR staining indicated strong perinuclear affinity of all three proteins in neutral conditions but clear reduction in spatial concordance between RHEB and LAMP1-mTOR in low pH as a result of RHEB's resistance to the centrifugal forces acting on LAMP1 and mTOR (7G).

These data suggested a model in which peripheral redistribution of lysosomes in acid inhibited the circadian clock by limiting RHEB's ability to spatially contact lysosome-bound mTOR to activate it. We reasoned, then, that a sufficient increase in the amount of RHEB in the periphery should rescue the circadian clock by restoring activity of peripherally redistributed mTOR. Indeed, abundant overexpression of constitutively

active RHEB<sup>N153T</sup> (Urano et al., 2005) caused mislocalization of RHEB throughout the cell and thereby increased peripheral RHEB density to quantified levels at or above the typical neutral perinuclear level without altering LAMP1 or mTOR localization (7F, 7G). As hypothesized, this restoration of RHEB-mTOR coincidence was accompanied by a full rescue of clock oscillation in acidic media (7H) and a corresponding more thorough resistance of mTORC1 signaling to acid compared with knockout of TSC2 (7I). That acidification facilely spatially separates RHEB and mTOR but not LAMPs and mTOR suggests that in these cells the majority of RHEB may normally be localized on non-lysosomal endomembranes at the MTOC—a distribution supported by high resolution images showing tight spatial congruity in LAMP and mTOR distribution and close apposition but discordance between either of these two and RHEB (S7I)—a surprising notion given current favored models of mTORC1 signaling (Sancak et al., 2010), but not unprecedented (Hanker et al., 2010; Manifava et al., 2016), that would indicate trans-endomembrane RHEB-mTOR interaction mechanistically underlying mTOR activation (7J).

Having delineated a mechanistic model to explain how acid produced by hypoxic metabolic rewiring suppresses mTORC1 signaling, we then wished to test whether such mechanisms could be observed in tumors *in vivo* on account of the hypoxic and acidic nature of significant portions of tumors (Gallagher et al., 2008; Gillies et al., 2002). To do so we made use of tumor specimens available from several previously undertaken studies (Estrella et al., 2013; Ibrahim-Hashim et al., 2017) in which tumor xenografts were hosted by mice drinking either tap water or water supplemented with sodium bicarbonate, the latter a method shown in these studies and by others (Gallagher et al., 2008) to raise intratumoral pH, including, notably, intracellular pH (Raghuhand et al., 1999). We assessed these tumors by immunohistochemistry for phosphorylated S6

(pS6) as a measure of mTORC1 signaling. This analysis revealed that, in two tumor models (colon cancer HCT116, breast cancer MCF7) exhibiting low pS6 staining in tumors hosted by control mice, sodium bicarbonate therapy significantly elevated mTORC1 signaling (7K, S7L), consistent with *in vitro* corollary work with these cell lines showing acid sufficient to inhibit mTORC1 signaling and additional bicarbonate (highly buffered media) able to blunt HIF-mediated mTORC1 suppression (S7J-K). Importantly, this elevation in mTORC1 signaling in treated tumors is not a secondary effect of bicarbonate stimulating proliferation, as growth rates of bicarbonate-treated tumors in these studies were either slower (HCT116) or unaffected (MCF7) (Estrella et al., 2013; Ibrahim-Hashim et al., 2017). In a third model (breast cancer MDA-MB-231), tumor mTORC1 activity was already high in control mice and no further augmentation was seen with bicarbonate therapy (S7M). This suggests tumor acidity suppresses mTORC1 signaling in significant regions of tumors *in vivo* but that some tumors have unknown mechanisms of escape.

Interestingly, unlike the full rescue of circadian oscillation observed with RHEB<sup>N153T</sup> overexpression in acidic media (7H), overexpression of RHEB<sup>N153T</sup> failed to rescue circadian oscillation from DMOG treatment despite high mTORC1-signaling (7I) and cells began to die after about 2.5 days (S7N). Consistent with the unfolded protein response RNA signature seen in acid (S3D), modest phosphorylation of the translation initiation factor eIF2 $\alpha$  was seen in exposure to acidic media and in more acidic late time points during DMOG exposure (S7O). We speculated that persistent mTORC1-signaling forced by RHEB overexpression might compound the unfolded protein response of acidified hypoxic cells and evoke a strong stress response that inhibits translation orthogonally to mTORC1 and thwarts our efforts to rescue the clock (S7P). Indeed, in support of this model, only cells overexpressing RHEB<sup>N153T</sup> during DMOG exposure

displayed hyperphosphorylation of endoplasmic reticulum (ER) transmembrane protein PRKR-like ER kinase (PERK) and induction of downstream ER-stress-responsive targets activating transcription factor 4 (ATF4) and C/EBP homology protein (CHOP/*DDIT3*) (S7Q) (Wouters et al., 2005). Thus, forced high mTORC1-induced translation in acidified hypoxic cells exacerbates ER stress, inhibiting cap-dependent translation through eIF2 $\alpha$  phosphorylation which in turn drives translation of the *DDIT3* transcription factor ATF4 (S7Q). Consequently, continued suppression of the clock in RHEB-overexpressing HIF-stabilized acidic cells highlights the same fundamental principle learned from acid-mediated mTOR suppression: inhibition of translation during hypoxic stress suspends the molecular circadian clock.

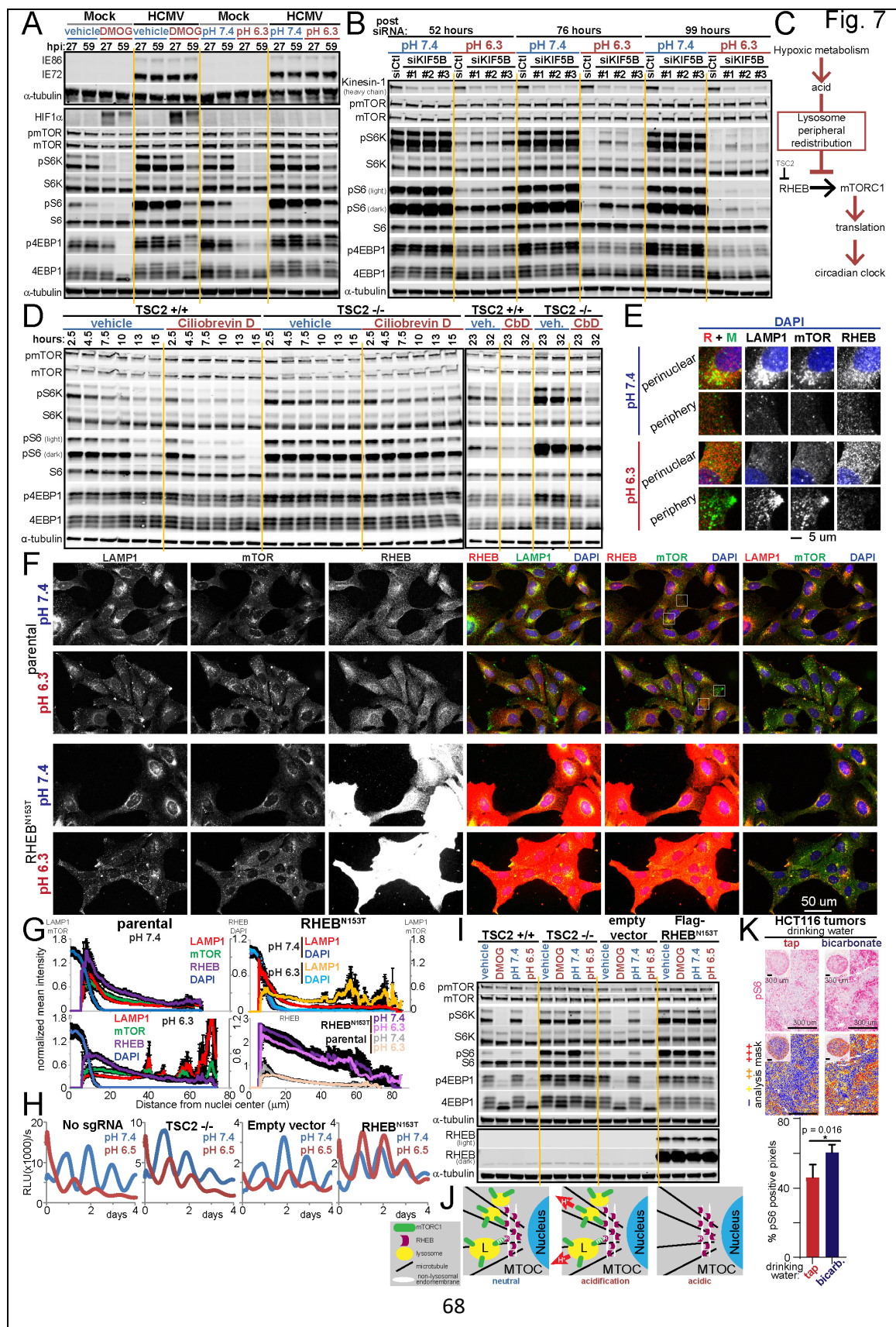


**Figure 7 – Acid inhibits mTORC1 signaling and the clock by spatially separating RHEB and lysosome-bound mTORC1.**

**A.** Immunoblot for mTORC1 signaling, HIF1 $\alpha$ , and the human cytomegalovirus (HCMV) proteins IE72 and IE86 using lysates from HCMV-infected or uninfected (mock) U2OS cell. Cells were treated with vehicle or 500  $\mu$ M DMOG in low buffer conditions for 8 and 12 hours prior to harvest at 27 and 59 hours post infection (hpi), respectively. Exposure to pH 7.4 and 6.4 began 1 hour prior to harvest. **B.** Immunoblot for mTORC1 signaling and kinesin-1 heavy chain (HC) using U2OS cell lysate collected at 52, 76, and 99 hours post delivery of 10 nM control (Ctl) siRNA or three different siRNA against *KIF5B* (kinesin-1 HC). Cells exposed to media of pH 7.4 and 6.5 one hour prior to harvest. RE of 2. **C.** Model. Acid produced during hypoxic metabolic rewiring suppresses circadian clock oscillation through inhibition of mTORC1-governed translation as a consequence of centrifugal redistribution of lysosome-bound mTORC1 limiting mTOR activation by RHEB. **D.** Immunoblot of mTORC1 signaling using lysate collected over a 32-hour timecourse from clonal *TSC2* CRISPR knockout (-/-) or parental U2OS cells (+/+) treated with vehicle or 50  $\mu$ M ciliobrevin D. Left: time points up to 15 hours. Right: 23 and 32-hour time points. **E/F.** U2OS parental and constitutively active *RHEB*<sup>N153T</sup>-expressing cells immunostained for LAMP1, mTOR, RHEB and nuclei (DAPI) after 160 minutes in media of pH 7.4 or 6.3. White boxes in F correspond to the fields enlarged in E to highlight representative perinuclear and peripheral regions of parental cells. RE of 3. **G.** Mean intensity of DAPI, mTOR, RHEB, and LAMP1 as a function of distance from the nucleus quantified from F. n=10-13 cells each pH for each cell line. Mean $\pm$ SEM normalized to each channel's maximum for parental pH 7.4 **H.** Luminescence monitoring of the

*Arntl::dLUC* reporter in *TSC2* CRISPR knockout (-/-), *RHEB*<sup>N153T</sup>-expressing, and respective control U2OS synchronized and exposed to pH 7.4 or 6.5 media. Mean of 3 BR. RE of 3-4, 1-3 BR each. **I.** Immunoblot for mTORC1 signaling using lysate collected from cells treated in parallel to H or treated with vehicle or 500  $\mu$ M DMOG in low buffer conditions for 20 (*TSC2*) or 16 (*RHEB*<sup>N163T</sup>) hours. RE of 2. **J.** Model of trans-endomembrane contact between lysosome-localized mTORC1 and non-lysosomal RHEB disrupted upon acid-driven peripheral redistribution of lysosome-bound mTOR. MTOC = microtubule organizing center **K.** Immunohistochemical pS6 staining of HCT116 xenograft tumors carried by host mice drinking normal tap water or 200 mM sodium bicarbonate *ad libitum* throughout tumor hosting (up to 3 weeks). Representative high-power fields with inset low-power images of entire tumor cross section. Positivity mask in lower panels. Percent pS6 positive pixels quantified over entire viable area of tumor cross section. Mean $\pm$ SD n=4 mice each arm. 2-tailed Student's t-test. RE= representative experiment. Biological replicates = BR. See also Figure S7.

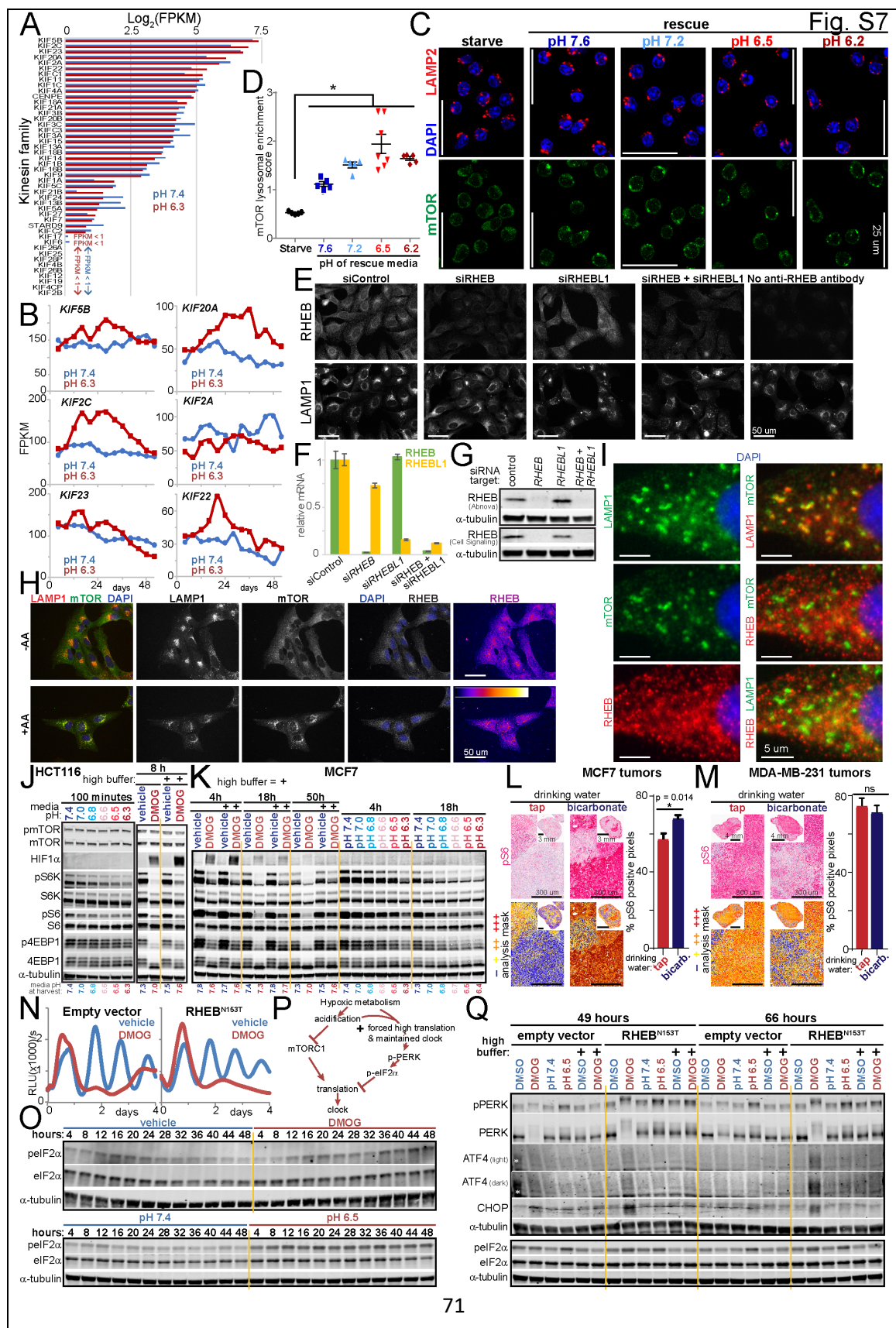


**Figure S7. Dampened translation subsequent to either silencing of lysosome-bound mTORC1 by acid or ER stress disrupts the clock. Related to Figure 7**

**A.** Expression of kinesin family members (n=46) in U2OS cells as determined by RNA-seq reported as the  $\log_2$  of the mean fragments per kilobase of transcript per million mapped reads (FPKM) determined every 4 hours for 52 hours (13 time points) after exposure to media of pH 7.4 or 6.3. Ranked by mean expression in pH 6.3. **B.** Expression of the 6 most abundant kinesins as determined in A. **C.** Previously activated OVA-specific CD8<sup>+</sup> T cells (OT-1, see Methods) coimmunostained for LAMP2, mTOR, and DAPI following starvation of amino acids and growth factors for 1 hour (neutral pH) prior to continued starvation for 30 minutes or rescue with replete media (full amino acids and serum) of pH 7.6, 7.2, 6.5, or 6.2 for 60 minutes. Images of staining of endogenous proteins contrasted uniformly (see Methods). **D.** Quantification of mTOR lysosomal enrichment in C. n = 5-7 fields each condition, encompassing 437, 293, 303, 243, and 393 total cells, respectively. Mean  $\pm$  SEM superimposed by raw data. Ordinary 1-way ANOVA followed by Tukey method comparing all means. Rescue from starvation increases mTOR lysosomal enrichment. Increasing acidity of rescue media does not reduce mTOR lysosomal association. \* $p \leq 0.05$ . **E.** U2OS cells coimmunostained for LAMP1 and RHEB after 2 days of treatment with non-targeting siRNA or siRNA targeting RHEB, RHEBL1, or both RHEB and RHEBL1 (10 nM each target, normalized to 20 nM with non-targeting siRNA where needed) to validate immunofluorescence specificity of the anti-RHEB antibody. RE of  $>3$ . **F/G.** qPCR (F) and immunoblot (G) of RNA and protein collected in parallel to E to assess knockdown efficiency and accordance with an independent anti-RHEB antibody (Cell Signaling) (G). Mean  $\pm$  SEM of technical replicates in F. RE of 3 each. **H.**

U2OS cells immunostained for LAMP1, mTOR, RHEB and nuclei (DAPI) after amino acid starvation for 155 minutes followed by 10 minutes of amino acid or mock rescue. RE of 3. **I.** Representative U2OS cell in media pH 7.4 immunostained for LAMP1, mTOR, RHEB, and nuclei (DAPI). Channel combinations as shown to highlight high coincidence of mTOR and LAMP1 staining consistent with localization of mTOR to lysosomes. Distinct patterning of RHEB suggests possible occupancy of a separate but spatially adjacent compartment. **J.** Immunoblots for mTORC1 signaling using lysate collected from HCT116 cells exposed to media of the indicated pH or treated with vehicle or 1 mM DMOG in low or high buffer media for the durations indicated. RE of 2 each with 2 BR. **K.** Immunoblots of lysate from MCF7 cells as in J. **L/M.** Immunohistochemical pS6 staining of cross sections of MCF7 (L) and MDA-MB-231 (M) xenograft tumors carried by host mice drinking normal tap water or 400 mM sodium bicarbonate *ad libitum* from 3 days post tumor cell inoculation through tumor harvest (five weeks later). Representative high-power fields with inset low-power images of tumor cross section. Positivity mask in lower panels. Percent pS6 positive pixels quantified over entire viable area of tumor cross section. Mean $\pm$ SD, n=5 mice (L) or 4 mice (M) for each arm. 2-tailed Student's t-tests \*p<0.05, ns=not significant **N.** Luminescence of *RHEB*<sup>N153T</sup>-overexpressing and control *Arntl::dLUC* U2OS cells treated with vehicle or 500 uM DMOG in low buffer conditions. Mean of 3 BR. RE of 4, 1-3 BR each. **O.** Immunoblot for phosphorylated and total eIF2 $\alpha$  (Ser51) using lysate collected from U2OS cells every 4 hours for 48 hours after synchronization and treatment with vehicle or 300 uM DMOG in low buffer media (upper) or exposure to media of pH 7.4 or 6.5 (lower). Tubulin loading controls shared with S4G and 4F. **P.** Model. Acid produced during hypoxic metabolic rewiring suppresses circadian clock

oscillation through inhibition of mTORC1-governed translation as a consequence of centrifugal redistribution of lysosome-bound mTORC1. Orthogonal stress signaling pathways, such as that resulting in inhibitory phosphorylation of eIF2 $\alpha$ , can likewise inhibit circadian clock oscillation by converging on a common mechanism of dampened cap-dependent translation. **Q.** Immunoblot for signaling downstream of PERK over a 3-day timecourse using lysate collected from *RHEB*<sup>N153T</sup>-overexpressing or control U2OS cells synchronized and treated with vehicle or 500 uM DMOG in low or high buffer conditions or exposed to media of pH 7.4 or 6.5. \*non-specific artifact. Representative experiments of 4 with varying sampling intervals. RE= representative experiment. Biological replicates = BR.

## CHAPTER 3 – Conclusions and Future Directions

### Conclusions

Hypoxia, because of the significant metabolic challenge it poses, has long been speculated to alter many aspects of normal physiology. Those conducting early rodent and human studies observed that low oxygen reversibly dampened the amplitude of normally circadian parameters such as body temperature (Bosco et al., 2003; Mortola and Seifert, 2000). Others noted the structural similarities between hypoxia inducible factors and clock network proteins (Bersten et al., 2013) and their capacity to heterodimerize *in vitro* (Hogenesch et al., 1998; Hogenesch et al., 2000; Takahata et al., 1998). Still others noted the sequence similarity between E-box (CLOCK-BMAL1) and HRE (HIF-ARNT) consensus binding sites and reported transcriptional crosstalk (Chauvet et al., 2004; Miki et al., 2004; Miyazaki et al., 2002; Pelster and Egg, 2015). While our studies were in progress, three reports revived this notion of hypoxia-clock interplay and concluded that HIF1 $\alpha$  might disrupt the clock through binding to promoters of specific clock network genes (Adamovich et al., 2017; Peek et al., 2017; Wu et al., 2017). While both Wu and Peek presented evidence of endogenous (Peek) or overexpressed (Wu) HIF1 $\alpha$  binding to the *PER2* promoter, and Adamovich proposed HIF1 $\alpha$  binding to *ROR $\alpha$*  and *CRY2* promoters, functional testing via rescue experiments (i.e. knockdown of proposed HIF-driven clock genes) either failed (Adamovich) or was not performed (Wu and Peek).

In contrast to these foundational studies, we show that acid—not HIF transactivation of clock genes—mediates suspension of the circadian molecular clock and diurnal transcriptome in hypoxia or upon pharmacologic stabilization of HIF. Acid, a

consequence of HIF-directed hypoxic metabolism, is sufficient to drive lysosomes, the platform upon which mTORC1 is normally activated, to the cell periphery. We find this redistribution suppresses the clock by spatially separating mTORC1 from its upstream regulator RHEB and thereby potentially inhibiting mTORC1 signaling and the translation of clock network proteins governed by it. Knocking down *HIF1A* or inhibiting its glycolytic flux-enabling target *LDHA*, buffering against acidification, or restoring mTORC1 activity each rescues clock oscillation, illustrating that acid produced due to HIF1 $\alpha$ -mediated metabolic rewiring halts the clock by inhibiting mTORC1, a complex well known to coordinate cellular activities to match current metabolic resources and afflicting stresses.

Indeed, by identifying pH as the critical variable and allowing it to align to that seen in the hypoxic solid tumor microenvironment, we uncover a more profound (Peek et al., 2017) and consistent (Wu et al., 2017) clock disruption by HIF than that recently described. Notably, these studies proposing direct transcriptional mechanisms for how HIF perturbs the clock presented no or limited evidence that described HIF-driven clock transcript-level changes propagated to the protein level. Additionally, Wu and colleagues relied exclusively on chemical or genetic stabilization of HIF1 $\alpha$  (rather than true hypoxia), and they, like Peek and colleagues, performed no confirmatory timecourses at the endogenous transcript or protein level to corroborate reporter-based conclusions of effects on rhythmicity (Peek et al., 2017; Wu et al., 2017). With our experiments employing both chemical- and low oxygen-mediated HIF stabilization (as well as pH conditions) and our gathering of two-day 4-hour resolution timecourses at the clock reporter, endogenous transcript, endogenous protein, and, in the case of pH conditions, protein-coding transcriptome levels, we significantly extend the vantage into how hypoxia effects the circadian biology of cells.

To our knowledge, few others have explored the effect of low pH on the clock. However, those that have observed, without explanatory mechanism, similarly profound suppression of clock-driven oscillations in rat fibroblasts and mollusks, with the latter also shown to be reversible and phenocopied by chemicals that block H<sup>+</sup> efflux and acidify pHi (Khalsa et al., 1991; Kon et al., 2008). Interestingly, in the one seemingly contradictory brief report, the limited data presented appeared to indicate acidic (pH 6.7) culture of primary human skin fibroblasts modestly enhanced amplitude of oscillation relative to neutral culture, perhaps indicating that physiologically acidic tissues such as skin (pHe 4.5-6.9 (Ohman and Vahlquist, 1994)) upregulate proton extrusion pathways to maintain neutral pHi in these more acidic milieus or harbor mTOR signaling or other factors supportive of the clock tuned for peak activity at pH values appropriate for their physiologic niche (Lee et al., 2011).

Our conclusion that mTORC1 is rapidly, potently, and durably inhibited by acid is corroborated by other work. Remarkably, prior to the discovery of mTOR, it was observed that intracellular acidification (through acidic media exposure or genetic or pharmacologic inhibition of H<sup>+</sup> export) could potently suppress phosphorylation of ribosomal protein S6 and translation (Chambard and Pouyssegur, 1986; Pouyssegur et al., 1982). More recently, a group has rediscovered acid's effect. However, the mechanism seems to have alluded them, with their first report concluding TSC2 dependence (Balgi et al., 2011) and a subsequent report TSC2 independence (Fonseca et al., 2012). We resolve this paradox by identifying that acid-driven peripheral relocalization of mTOR limits its activation by RHEB; correspondingly, TSC2 knockout partially rescues mTORC1 signaling by eliminating GAP activity toward RHEB but does not circumvent this downstream block.

We observed striking peripheral redistribution of lysosomes in acidic conditions, a phenomenon first described decades ago (Heuser, 1989) and documented since in a number of systems. To our knowledge, no one has previously queried if an acidic environment might impact mTORC1 signaling through this spatial disturbance. Our work thus gives mechanistic significance to a long unexplained low pH phenomenon and intriguingly furthers in new ways a theme of governance of mTOR activity through spatial positioning of key players (Menon et al., 2014; Sancak et al., 2010).

In summary, our studies reveal that hypoxia reversibly suspends the homeostatic circadian timekeeper of cancer cells as a consequence of a byproduct of the metabolism it dictates driving a subcellular inhibitory spatial alteration of mTORC1.

## **Future Directions**

### *Acid as a synchronizing stimulus*

Recognizing the incompleteness of their model, the recent Adamovich publication proposed that the ability of oscillating tissue oxygen tensions and the HIF1 $\alpha$  axis to reset clocks in mammalian tissues and cell lines could be mediated by “other factors yet to be identified.” Whether oscillating transient acidification fulfills this role awaits formal demonstration; but, clock-driven circadian oscillations in pH in mammalian tissues (Dmitriev and Mangel, 2001; Peek et al., 2017) allow for the intriguing possibility of conserved reinforcing bidirectional acid-clock crosstalk.

### *mTORC1 as a mediator of peripheral clock entrainment by feeding rhythms*

Our finding that mTOR governs peripheral clocks echoes prior findings in the central clock of model organisms such as flies (Zheng and Sehgal, 2010). Notably, in the central clock of mice, the mTOR/4EBP1/eIF4E axis is activated by light, and

pharmacologic or genetic inhibition reduces light-induced translation of clock proteins and entrainment (Cao et al., 2015; Cao et al., 2010; Cao et al., 2013). Recent observations in peripheral mammalian clocks also point to a clock-mTOR connection, as PTEN loss in human head and neck squamous cell carcinoma cell lines and mouse epidermis increases BMAL1 protein levels in an mTORC1-dependent manner (Matsumoto et al., 2016). Additionally, rhythmic mTOR signaling has been shown to support circadian rhythmicity in mammalian translation rates (Jouffe et al., 2013; Lipton et al., 2015), emphasizing the multiple levels at which mTOR acts to promote optimal timing. Moreover, as feeding cycles are now understood to be the dominant entraining force (*zeitgeber*) for peripheral clocks (Introduction Box 1) (Damiola et al., 2000), it is especially alluring to consider that mTOR, given its role in sensing nutrient, growth factor, and energy levels and coordinating cellular response, is poised to perhaps be a central player in this currently only incipiently understood synchronization pathway (Dibner and Schibler, 2015).

#### *pH as an environmental parameter sensed by mTOR*

mTORC1 integrates several environmental signals including those indicative of levels of amino acids and energy to limit biosynthetic activities—particularly translation—to times sufficiently supported by requisite resources (Saxton and Sabatini, 2017). It is intriguing to think that pH might similarly be monitored by mTORC1 through mechanisms described here to restrict protein synthesis to periods when pH is conducive to appropriate protein folding. Additionally, mTORC1 might sense glycolytic flux through the two protons produced for every glucose molecule metabolized to pyruvate or lactate (Chapter 1 – Introduction, Box 6; (Divakaruni et al., 2014)). As mTORC1 positively regulates glycolysis (Brugarolas et al., 2003; Duvel et al., 2010), an ability of mTORC1 to

sense an accumulating metabolic acid load—which threatens to slow the kinetics of enzymatic reactions, inappropriately protonate peptides, and otherwise harm the health of cells—and ease its drive of this acid source would seem advantageous. In this manner, a  $H^+$ -mediated feedback loop might exist regulating glycolysis through known mTORC1-sensitive glycolysis-stimulating factors, such as HIF1 $\alpha$ , permitting mTOR to tune glycolytic flux to optimal rates.

#### *Resolution of conflicting reports about active mTOR in the cell periphery*

Our finding that centrifugal lysosome redistribution is both necessary and sufficient for acid's suppression of mTOR is consistent with prior work indicating dynein (Clippinger and Alwine, 2012) and perinuclear clustering of lysosomes (Clippinger et al., 2011; Rainero et al., 2015) support mTORC1 signaling. However, it is notable that Korolchuk and colleagues reported a seemingly inverted spatial dynamic from our findings with starvation (and therefore inhibited mTOR) associated with perinuclear clustering of lysosomes and refeeding (and therefore active mTOR) associated with peripheral redistribution (Korolchuk et al., 2011). As starvation-induced mTOR inhibition induces autophagy (Kim and Guan, 2015), this perinuclear clustering of lysosomes may reflect the movement of lysosomes and autophagosomes to the microtubule organizing center (MTOC) to facilitate fusion. Indeed, pharmacologic inhibition of mTORC1 has been shown to be sufficient to induce perinuclear lysosome aggregation (Li et al., 2016). As centrifugal lysosome redistribution is a cause rather than consequence of mTORC1 inhibition in our model, acid-induced silencing of mTORC1 through peripheral redistribution of lysosomes is not incompatible with autophagy-induced retrograde trafficking of lysosomes.

However, further data presented by Korolchuk and colleagues are more difficult to reconcile with our findings. These authors reported that peripheral margination of lysosomes in HeLa cells through overexpression of several kinesins and associated adaptors caused augmented mTOR signaling with the reverse true upon knockdown (Korolchuk et al., 2011). However, a more recent report in HeLa cells did not observe hindered mTORC1 signaling when lysosomes clustered at the MTOC in response to knockout of a different kinesin-associated factor (Pu et al., 2015). The reasons for these contradictory results in the same cell line remains unclear. Nonetheless, we cannot exclude the existence of cell-type specific differences as HeLa cells appear distinctly wired in several ways, perhaps in some way stemming from their origin in cervical tissue, a particularly acidic environment. For instance, Korolchuk and colleagues noted that starvation (including serum starvation) alkalinized HeLa cell pHi, which they suspected mediated lysosome perinuclear aggregation. Given that it is classically noted that growth factor stimulation causes alkalinization of pHi, owing to the growth-factor responsiveness of H<sup>+</sup> exchangers such as NHE1 (Moolenaar, 1986; Pouyssegur et al., 1985), it is not surprising that work in other cell types, or even the same cell type (Martins et al., 2011), has noted opposite directionality with lysosomes peripherally redistributed upon starvation (Wang et al., 2017; Zaganjor et al., 2014).

As most cells display predominantly perinuclear lysosomes (Jongsma et al., 2016) (and mTOR (Clippinger and Alwine, 2012; Clippinger et al., 2011; Sancak et al., 2008)) in culture (i.e. while growing and therefore dependent on mTORC1), we suspect future investigations will clarify that perinuclear lysosome-bound mTORC1 is an active pool and that this location is critical for spatial contact with RHEB. Indeed, in other studies exploring the spatial localization of mTOR in HeLa cells—as well as in MEFs, A549, and PANC-1 cells—the majority of mTORC1 localized perinuclearly in serum-

stimulated (mTORC1-activated) cells with a much smaller portion localized to plasma membranes (Saci et al., 2011). Correspondingly, a recent study across a panel of cell types, including Hela, characterized two populations of lysosomes: a principal perinuclear “cloud” and much tinier highly dynamic pool sparsely and transiently populating the periphery (Jongsma et al., 2016). That HCMV has evolved a mechanism to actively bring mTOR to the perinuclear region and that doing so allows the virus to maintain mTORC1 activity in the face of inhibitory signals underscore, we believe, the importance of this spatial location to mTORC1 activation (Clippinger and Alwine, 2012; Clippinger et al., 2011). However, in our studies at neutral pH the periphery of the cell was not devoid of lysosome-bound mTOR (Jongsma et al., 2016) and our model need not imply that subpopulations of mTORC1 do not translocate to various niches in the cell to regionally tailor biosynthetic activities.

#### *Mechanism of lysosome redistribution in acid*

The mechanism by which acid drives lysosomes to the periphery remains unsettled but is generally speculated to be an upsetting of the normal balance between centripetal (e.g. dynein) and centrifugal (e.g. kinesin) forces. It has been reported that acidification releases inhibitory effects of kinesin light chain on heavy chain binding to microtubules (Verhey et al., 1998), suggesting activation of a kinesin might be causative. Alternatively, axonemal dynein is appreciated to be inhibited by intracellular acidification, which is believed to keep spermatozoa flagella inactive during storage in the epididymis (Nishigaki et al., 2014), and pH-dependence of cytoplasmic dynein has been likewise proposed (Mohan et al., 2006).

As mentioned above, recent descriptions have characterized two pools of lysosomes in cells, a more abundant spatially restricted perinuclear pool, and a smaller more mobile peripheral pool (Jongsma et al., 2016). Delineation of the specific cargo trafficked by the many kinesin and dynein subunits and adaptors would permit better understanding of the entities redistributed by specific genetic and pharmacologic manipulations and may clarify discrepant reported impacts of genetic manipulations discussed above. Acid silences mTORC1 by driving mTORC1 away from its activator RHEB. Perhaps tactics that move mTORC1 and all its supporting positive regulators and substrates to the periphery in concert enhance activation of mTORC1 by increasing mTOR's proximity to upstream growth factor signaling molecules as proposed (Korolchuk et al., 2011; Saki et al., 2011).

#### *Role of lysosomal V-ATPase*

Lumens of lysosomes are acidified by the ATP-dependent vacuolar H<sup>+</sup> pump, V-ATPase (Mindell, 2012). Recently, it has been described that moving lysosomes to the periphery alkalinizes their lumen at least in part because of reduced activity of the lysosomal V-ATPase (Johnson et al., 2016). While knockdown and pharmacologic inhibition have confirmed the requirement for V-ATPase activity for amino acid-dependent recruitment of mTORC1 to lysosomes through RAGs (Zoncu et al., 2011), our verification that mTOR continues to reside on lysosomes in acid makes reduced V-ATPase activity an unlikely contributor to reduced mTOR activity in low pH. Nonetheless, the mechanism behind the requirement for V-ATPase activity—but peculiarly not lysosomal lumen acidity—for mTORC1 signaling remains unknown (Wolfson and Sabatini, 2017; Zoncu et al., 2011).

### *mTOR dependence of clock network translation*

Our data strongly support a model of suppression of the circadian clock in hypoxia through mTORC1 inhibition by acid. Indeed, low pH, which we observed to be sufficient to inhibit mTORC1 signaling, likewise displayed sufficiency for suppression of both clock network protein levels and amplitude of clock oscillation. Correspondingly, mTOR inhibitors (Torins, rapamycin, *n*-butanol) recapitulated clock suppression in proportion to their ability to durably and thoroughly inhibit mTORC1. Knocking down or out 4EBP proteins gave partial rescue of the clock (as hypothesized given redundancies in 4EBP proteins and continued suppression of S6K and S6 phosphorylation), while highly buffered media achieved commensurate full rescues of culture pH, mTORC1 signaling, clock network protein levels, and clock amplitude. Additionally, we documented an acid-driven spatial subcellular disturbance of the platform upon which mTORC1 signaling occurs and found this disturbance to be sufficient to inhibit mTORC1 and clock reporter oscillation. Moreover, overcoming this inhibitory spatial change with overexpression of constitutively active RHEB rescued mTORC1 signaling in acid with corresponding rescue of the clock, fully consistent with a model in which acid suppresses the clock through suppression of translation governed by mTOR.

Further study confirmed representative clock network proteins including BMAL1, PER2, and CLOCK are suppressed in low pH below the level of these proteins seen in a population of desynchronized cells (Figure 8, see legend), and in opposition to directionality of transcript dynamics (Chapter 2 – Results, Figure 2D), indicating protein-level suppression in acid rather than desynchrony of cells, in accord with single-cell assessment presented previously (Chapter 2 – Results, Figures 2A and S2E). Additionally, inhibition of translation with the translocation inhibitor cycloheximide not unexpectedly similarly diminished expression of these three representative clock

network proteins as well as clock reporter amplitude and cycling, recapitulating the effect of acid (Figure 9).

Figure 8

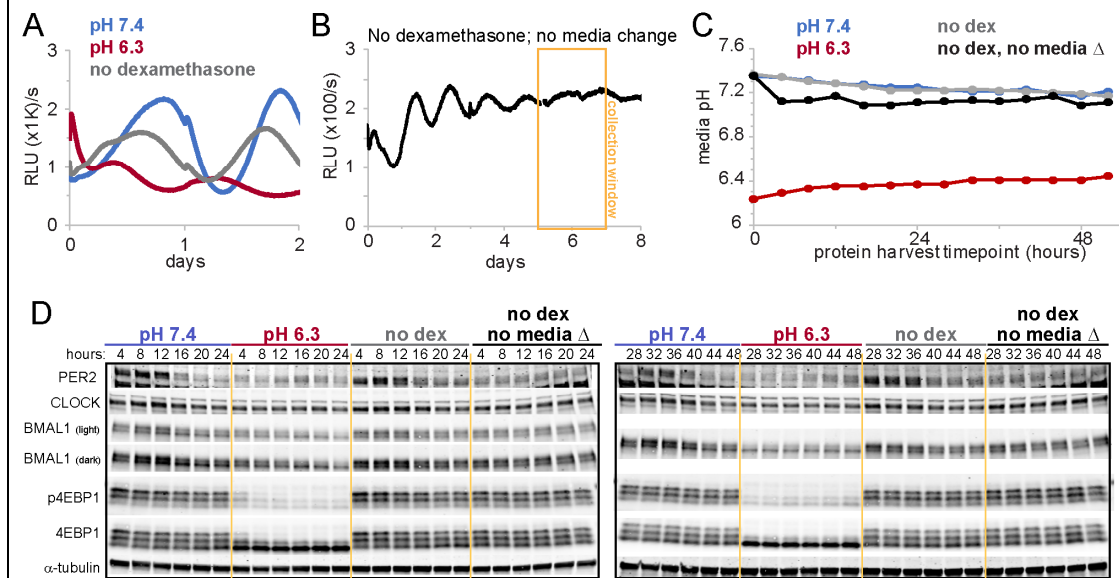


**Figure 8 - Clock network protein levels are suppressed in acidic cells to a level below that in desynchronized cells, indicating protein-level suppression rather than phase/period discordance.**

U2OS *Arntl::dLUC* cells were treated with neutral (pH 7.4) or acidic (pH 6.3) media containing dexamethasone and compared to two populations of desynchronized cells in media of neutral pH (pH 7.4): cells with no dexamethasone synchronization (“no dex”) or cells with no dexamethasone synchronization and allowed to incubate without media change for 5 days prior to experiment start to circumvent the synchronizing stimulus of media change (“no dex, no media change”). Clock reporter luminescence (A, B) and media pH (C) monitored in parallel to a 48-hour timecourse in which lysates were immunoblotted for representative clock network proteins (PER2, BMAL1, CLOCK) and mTORC1 substrate (4EBP1) phosphorylation (D). RLU = relative luciferase units.

Figure 9

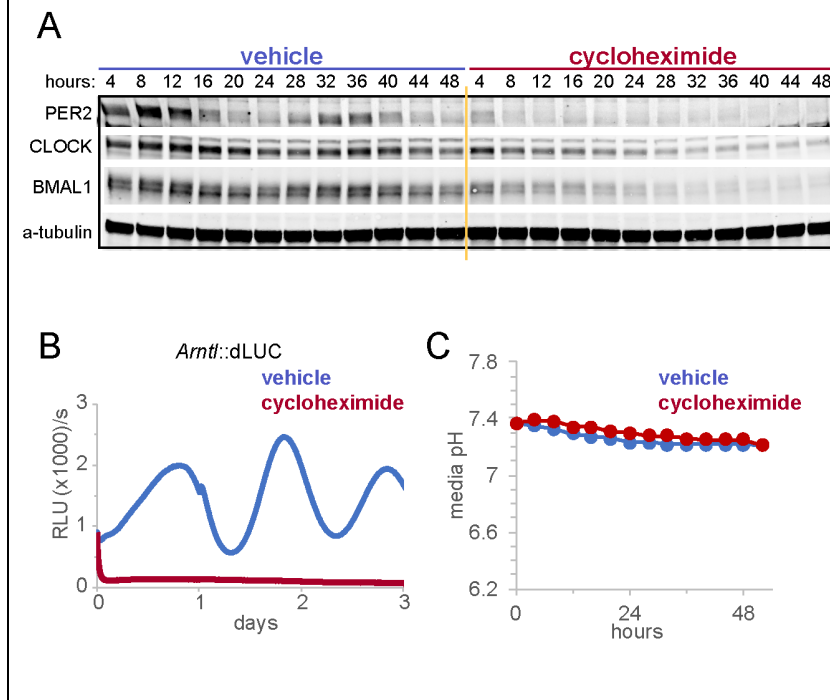


**Figure 9 - Inhibition of protein synthesis recapitulates pH-mediated clock collapse.**

**A.** Immunoblots for representative clock network proteins (PER2, CLOCK, and BMAL1) over a 48-hour timecourse using lysate collected from synchronized U2OS *Arntl::dLUC* cells treated with vehicle or 50 ug/mL cycloheximide. **B/C.** Luminescence (B) and media pH (C) monitored in parallel to the timecourse in A.

There are several classes of transcripts that have been shown to be exquisitely sensitive to mTORC1 inhibition (most notably, 5'-terminal oligopyrimidine tract (TOP) transcripts) (Nandagopal and Roux, 2015; Sonenberg and Hinnebusch, 2009). Although we have not bioinformatically scoured clock transcripts for nucleotide sequences characteristic of membership in these groups, we are aware of no report indicating clock genes are amongst these transcripts. However, as David Sabatini's and colleagues' ribosome profiling after Torin (mTOR inhibitor) treatment has revealed, while there indeed are TOP mRNAs that are hypersensitive to mTOR inhibition, "mTOR inhibition suppresses the translation of nearly all (99.8%) mRNAs to some degree, with a mean reduction in translation of 61%" (Thoreen et al., 2012). (Unfortunately, clock genes, other than REV-ERBs, did not make the detection cutoff for this analysis so were not reported on specifically in this study.) Thus, it is reasonable to expect that translation of clock genes is suppressed by mTORC1 inhibition.

As mTORC1 is a central regulator of numerous cellular processes, we anticipate inhibition of the circadian clock is part of an overarching cellular response to hypoxia mediated by acid. Indeed, both Torin treatment (Thoreen et al., 2012) and hypoxia (Koritzinsky et al., 2006) have been reported to cause a global decrease in the portion of ribosomes in polysomes (complexes of multiple ribosomes bound to the same mRNA, indicative of efficient translation of these transcripts). Similarly, when we performed polysome profiling of U2OS cells grown in neutral or acidic (pH 6.3) media for 37 hours, we observed reduction in the global polysome fraction and an increase in the number of monosomes and free ribosomal subunits (Figure 10, A-E) resembling the effect of Torin (Thoreen et al., 2012). Moreover, interrogation of the distribution of two representative clock network transcripts revealed both BMAL1 and PER2 mRNA to be disproportionately lost from polysomes (shifting to higher percentage found in

monosomal and free RNA) (Figure 10, F-G), consistent with a translational block. In contrast, TXNIP mRNA, known to be robustly transcriptionally induced by low pH (Chen et al., 2010), had substantial polysomal loading corresponding to the significant induction of its protein level (Figure 10, H-I).

Figure 10

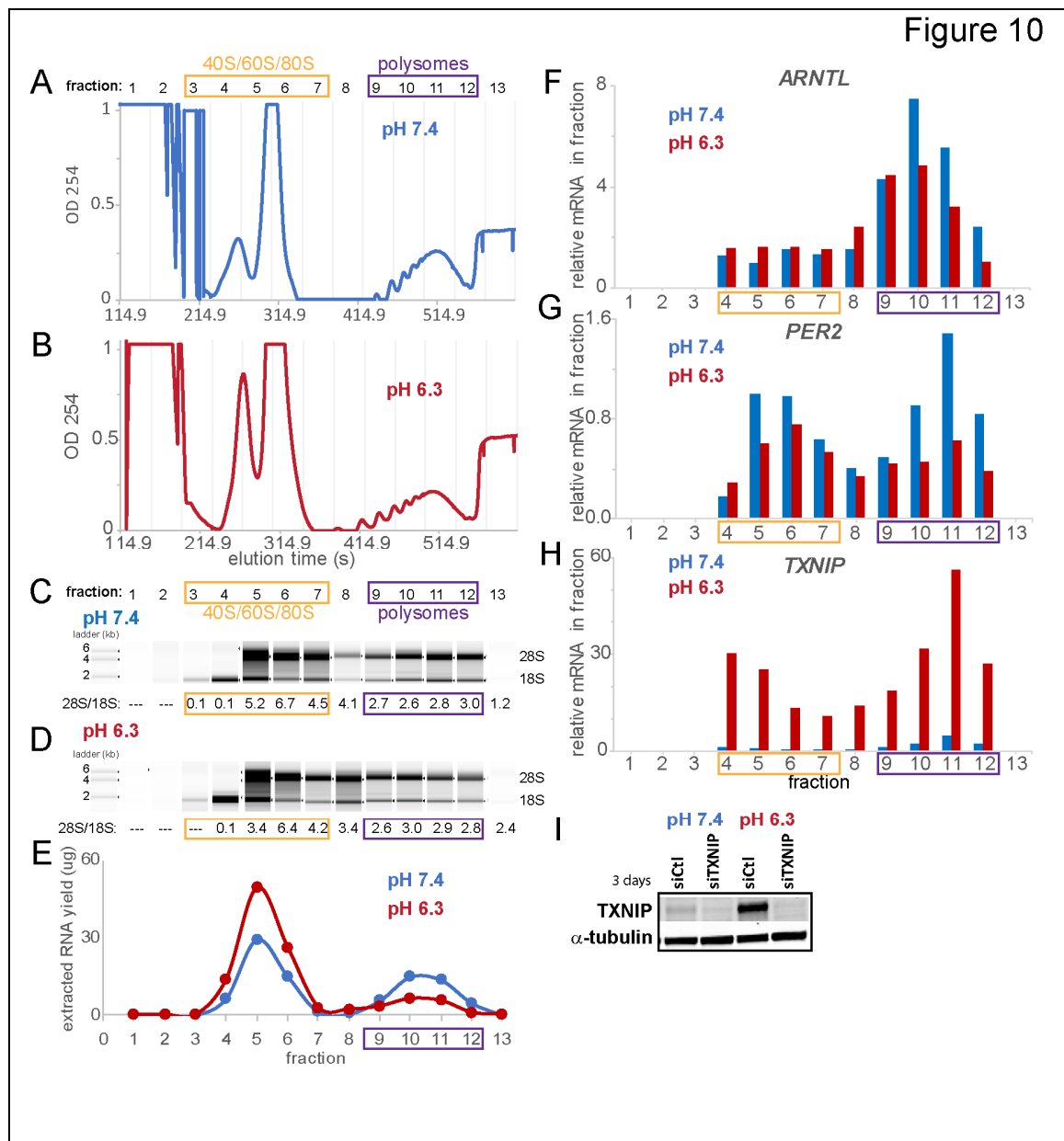


**Figure 10 – Low pH depletes clock network transcripts from polysomes while globally shifting ribosomes out of polysomes.**

**A/B.** Polysome profiling of U2OS *Arntl::dLUC* cells after 37 hours of exposure to pH 7.4 (A) or pH 6.3 media (B) as assessed by optical density of sucrose gradients at 254 nm with annotation of the 13 fractions subsequently made. **C/D.** “Gel-like images” of tape station analyses of extracted RNA to assess RNA composition. Bands corresponding to 28S and 18S (large and small ribosomal subunit component rRNAs, respectively) annotated along with ratio of 28S to 18S yield. Fractions  $\geq 9$  considered polysomes (See Methods). **E.** Nanodrop yield of purified RNA. Note profile correspondence to A-B suggesting good extraction yield across fractions. **F-G.** Relative abundance of clock protein-encoding mRNAs *ARNTL* (F) and *PER2* (G) in fractions as assessed by qPCR normalized to spike-in control (See Methods). **H.** Relative mRNA abundance of acid-induced transcript *TXNIP* similarly determined. **I.** Immunoblot for TXNIP in cells treated with 10 nM non-targeting or TXNIP-directed siRNA and exposed to media of pH 7.4 or 6.3 for 3 days (66 hours).

Overall, our observations suggest that low pH has a global effect on translation resembling Torin, reflecting the commonality of mTORC1 inhibition. Moreover, we directly document that this suppression of translation in acid encompasses clock network transcripts, supporting a model in which mTOR inhibition by low pH and consequential slowing of translation of clock network transcripts leads to clock collapse. Future polysome profiling at shorter timepoints of acid exposure might reveal specific clock network proteins to be disproportionately sensitive to mTOR inhibition. As light-induced translation of PER proteins in the central clock is reported to be particularly sensitive to mTORC1 inhibition (Cao et al., 2010), PER proteins might display analogous strong sensitivity to acid-mediated TOR inhibition in peripheral clocks.

#### *RHEB localization and mechanism of mTOR contact*

The ability of acid to drive rapid spatial redistribution of lysosome-bound mTOR without significant alteration of RHEB localization, as well as the incongruency in neutral conditions between RHEB and both mTOR and LAMP immunostaining patterning, suggested to us that RHEB perhaps is not localized to lysosomes. Indeed, our data led us to propose a model of mTORC1 signaling whereby amino acids recruit mTOR to lysosomes residing at the microtubule organizing center (MTOC) allowing mTOR to contact RHEB localized to distinct endomembranes likewise trafficked to or enriched in this subcellular domain. Such a model differs from the prevailing model of mTORC1 signaling (Chapter 1 – Introduction, Box 7; (Sancak et al., 2010)) in which RHEB is asserted to be constitutively anchored to lysosomal membranes. Resolving this opposition requires additional evidence to corroborate or reject our model or to clarify the cell-type or other parameters dictating when each discrepant mechanism prevails.

As described in the Results section (Chapter 2) and substantiated here with additional fields, replicates, or further experiments (see corresponding figure legends), we arrived at our model after careful verification of the specificity (Figure 11A) of a previously validated RHEB antibody (Menon et al., 2014) and interrogation of the distribution of RHEB (Figure 11B). Notably, in contrast to earlier reports suggesting that permeabilization destroys RHEB immunofluorescence signal (Buerger et al., 2006; Saito et al., 2005; Sancak et al., 2008), we, with incidentally mild permeabilization conditions, retained specific RHEB signal; however, that the Manning group's imaging excelled with somewhat harsher conditions than even some of these earlier studies (Buerger et al., 2006; Menon et al., 2014) suggests antibody quality not permeabilization technique limited early experiments. We then confirmed endogenous RHEB to reside in a perinuclear location similar to the distribution of lysosomes and independent of amino acid status (Figure 11 C), consistent with prior reports (Menon et al., 2014). As RHEB is described to be anchored to lysosomes through its farnesylated tail (Menon et al., 2014; Sancak et al., 2010; Sancak et al., 2008), we anticipated RHEB would be peripherally displaced in acid, mirroring lysosome redistribution. To our surprise, however, RHEB retained its perinuclear location in acid, thus becoming spatially separated from mTORC1 (Figure 11 D).

This unanticipated discrepancy between RHEB and mTOR-LAMP distribution and dynamics in acid suggested RHEB and mTOR might reside in distinct compartments in the perinuclear region. We decided to quantitatively characterize the spatial distribution of mTOR, RHEB, and LAMP1 in 4-color immunofluorescence microscopy images of U2OS cells at neutral pH to explore this possibility further. This approach compellingly supported our model, revealing LAMP1 and mTOR to be highly coincident in spatial distribution and RHEB to be closely apposed but discordant (Figure 11 E).

These observations are consistent with mTORC1 localization to lysosomes and RHEB occupancy of spatially adjacent but separate compartment. These data thus suggest the mechanistic importance of lysosome-localized mTOR activation by RHEB localized to non-lysosomal perinuclear endomembranes. Moreover, these data indicate a previously unsuspected mechanism of mTORC1 inhibition under low pH and provide a function for the rapid dispersion of lysosomes driven by acid—a phenomenon that was observed for several decades without understanding of its function.

Figure 11

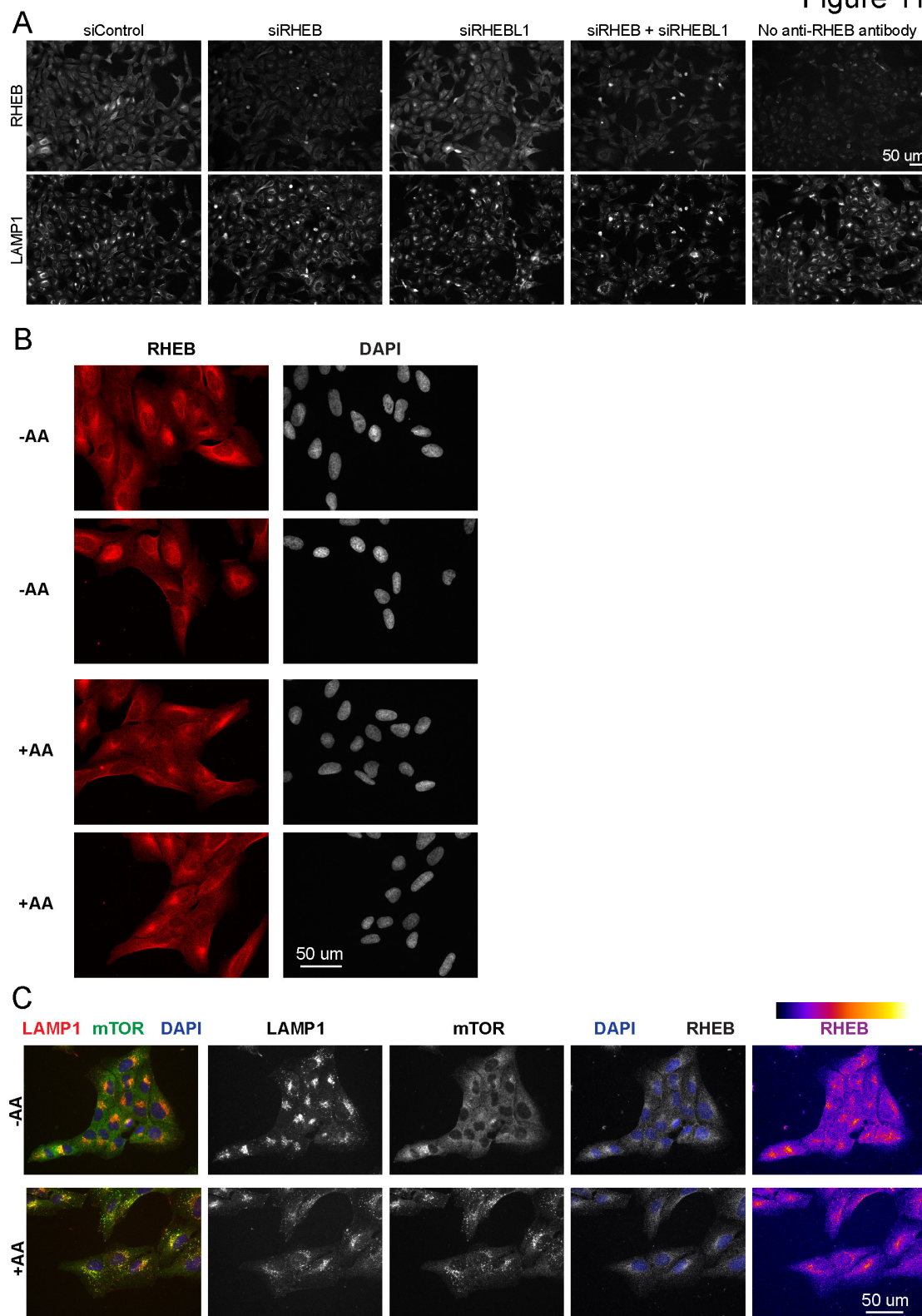
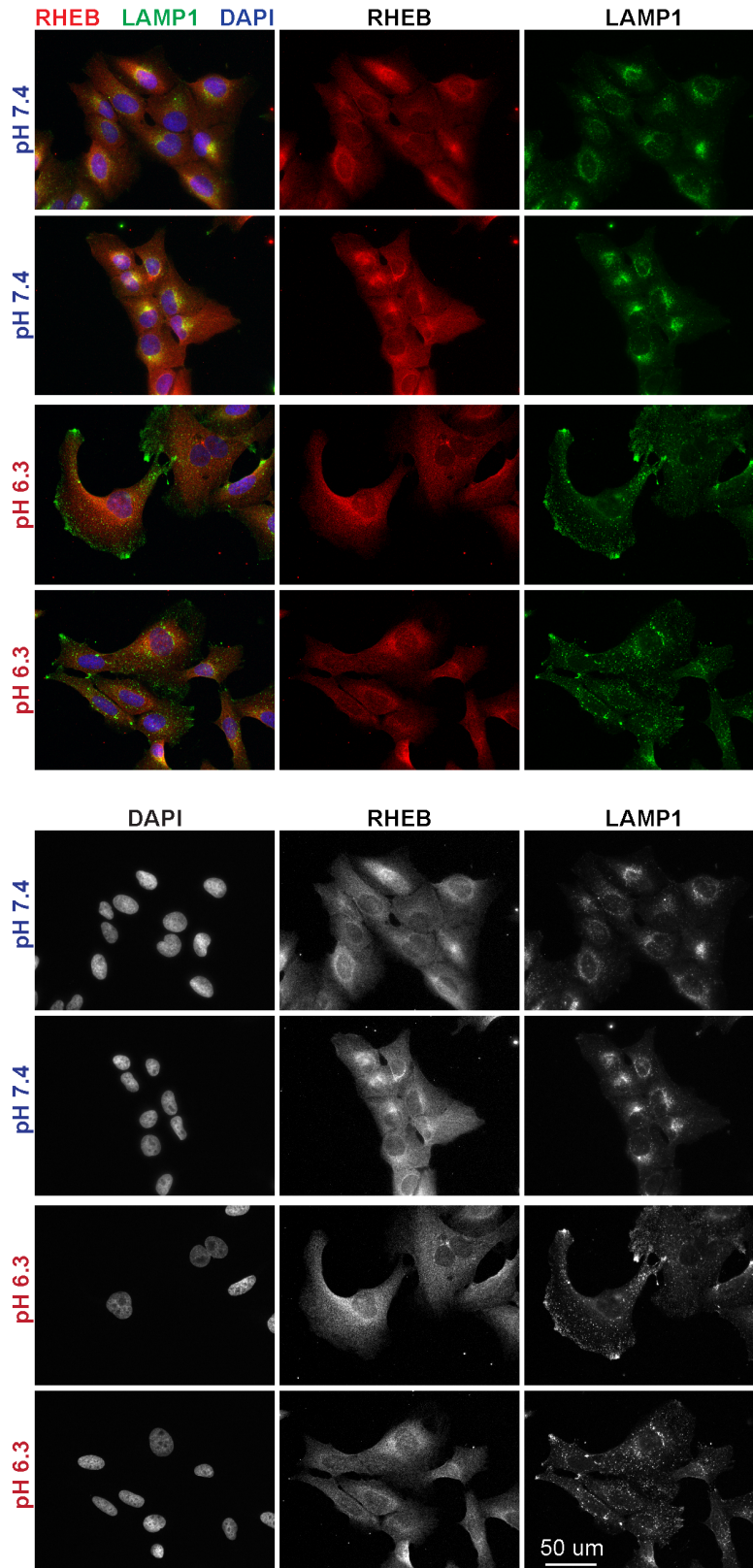


Figure 11 (continued)

D



same fields as above

Figure 11 (continued)

E

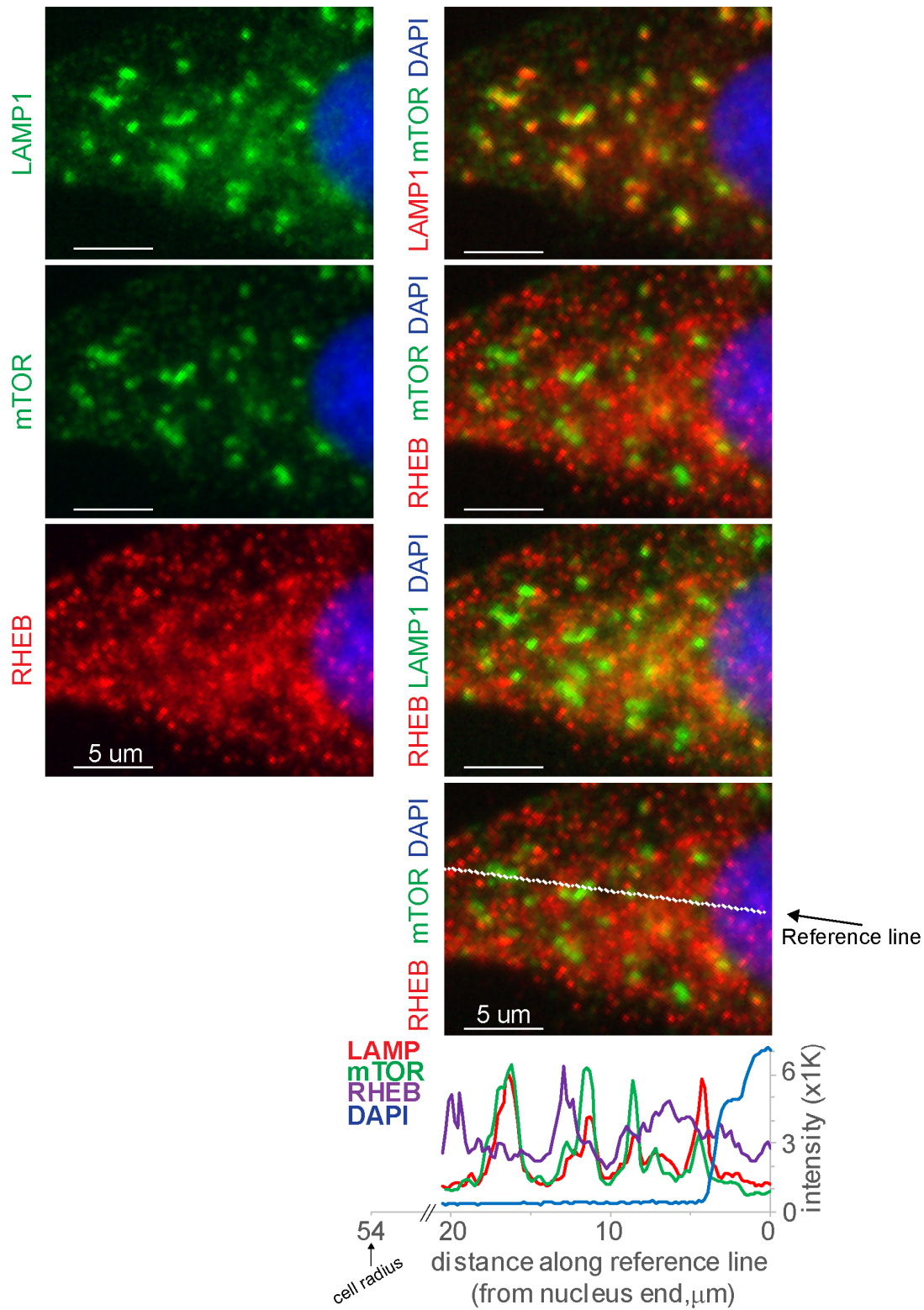


**Figure 11 – Immunofluorescence microscopy of endogenous RHEB suggests RHEB residence on non-lysosomal endomembranes at the microtubule organizing center.**

Extension of data presented in Chapter 2 Figure 7 and Supporting Figure 7. **A.** Low power fields of immunofluorescence imaging presented in Chapter 2 Figure S7E. U2OS cells coimmunostained for LAMP1 and RHEB after 2 days of treatment with non-targeting siRNA or siRNA targeting RHEB, RHEBL1, or both RHEB and RHEBL1 (10 nM each target, normalized to 20 nM with non-targeting siRNA where needed) to validate immunofluorescence specificity of the anti-RHEB antibody. RE of >3. **B.** Independent replicate experiment of data presented in Chapter 2 Figure S7H. U2OS cells immunostained for RHEB and nuclei (DAPI) after amino acid starvation for 105 minutes followed by 10 minutes of amino acid or mock rescue. **C.** Additional fields of immunofluorescence imaging presented in Chapter 2 Figure S7H. U2OS cells immunostained for LAMP1, mTOR, RHEB and nuclei (DAPI) after amino acid starvation for 155 minutes followed by 10 minutes of amino acid or mock rescue. RE of 3. **D.** U2OS cells immunostained for LAMP1, RHEB, and nuclei (DAPI) after 105 minutes in media of pH 7.4 or 6.3. RE of 3. Images in upper panel shown in single-channel grayscale in lower panel. Independent experiment from that presented in Chapter 2 Figure 7 E-F. **E.** Images reproduced here from Chapter 2 Figure S7I to show relationship with quantification presented here in lower panel. Representative U2OS cell in media pH 7.4 immunostained for LAMP1, mTOR, RHEB, and nuclei (DAPI). Intensity profile of LAMP1, mTOR, RHEB, and DAPI along a reference line (depicted) extending from within the nucleus outward through the cytoplasm (23  $\mu$ m line, longest cell radius 54  $\mu$ m). Distinct patterning of RHEB suggests occupancy of a

separate but spatially adjacent compartment. RE= representative experiment.  
Biological replicates = BR.

Our data suggest mTORC1 is inhibited in low pH because RHEB fails to move in concert with lysosomes to the periphery. Robustly overexpressing RHEB causes RHEB to mislocalize throughout the cell and rescues mTORC1 signaling from acid suppression, consistent with rescue through restoration of colocalization of RHEB with peripherally displaced lysosome-localized mTORC1. This model suggests that targeting RHEB to the lysosome or mTORC1 to the RHEB-containing compartment should rescue mTORC1 signaling in acid and would thus be an important future test of our model. Additionally, these unexpected data raise two central questions: on which membranes does RHEB reside? Why the contradiction to the prevailing model of mTORC1 activation?

RHEB's farnesylated tail and the ability of farnesylation inhibitors that dislodge RHEB from membranes to inhibit mTOR signaling (Buerger et al., 2006; Hanker et al., 2010) clearly suggest active RHEB resides on endomembranes. The perinuclear location of RHEB suggests several membranal compartments anchored by the microtubule organizing center are candidate endomembranes, including Golgi, endoplasmic reticulum (ER), and mitochondrial membranes.

Despite the dominant narrative (Sancak et al., 2010), several groups have reported non-lysosomal perinuclear RHEB localization in agreement with our inferences. Using GFP-tagged RHEB and RHEB2 (*RHEBL1*) constructs, Hanker and colleagues concluded RHEB proteins colocalized with Golgi and ER markers (Hanker et al., 2010). Especially notably, these authors explicitly stated a failure to observe colocalization of either RHEB protein with markers of late endosomes or lysosomes, including LAMP2 and LysoTracker. An earlier report by Buerger and colleagues likewise concluded RHEB associated with the ER and Golgi using a similar approach (Buerger et al., 2006). More precisely, abolition of mTORC1 signaling after treatment with brefeldin A, an ER to Golgi

trafficking inhibitor disruptive of Golgi integrity, supported the proposition that RHEB needed to reach Golgi membranes to activate mTORC1. Indeed, substitution of RHEB's endogenous membrane anchoring tail with an amino acid sequence intended to force RHEB to the Golgi, but not one targeting RHEB to the ER, was sufficient to fully activate mTORC1. Additionally, live cell imaging of trafficking of GFP-labeled wild-type RHEB over a timecourse with parallel immunoblotting for mTORC1 signaling showed mTORC1 activity to peak as RHEB reached the Golgi. Although these authors neglected to visually confirm the intended localization of RHEB following their forced-targeting technique and peculiarly harvested lysate from a different cell line than that imaged for their timecourse experiment, Manifava and colleagues have more recently independently corroborated this work and documented both ER and Golgi localization of fluorescently tagged RHEB and Brefeldin A sensitivity of mTORC1 signaling (Manifava et al., 2016). Thus, although we may be the sole voice suggesting lysosome-localized mTORC1 and RHEB localized to distinct endomembranes make contact by bridging these separate endomembrane compartments via the coordinating help of the microtubule organizing center, we are not the first to propose non-lysosomal RHEB localization. Moreover, Manifava and colleagues' inability to observe anticipated strong colocalization of mTORC1 and RHEB strongly parallels our experience and observations (Figure 11E).

Interestingly, early characterization of RHEB reported that RHEB nucleotide binding state appeared to dictate on which endomembrane compartment RHEB resided (Saito et al., 2005). Overexpressed wild-type RHEB localized to membranes overlapping with markers of late endocytic vesicles (late endosomes and lysosomes) but overexpressed constitutively GDP-bound mutant RHEB or overexpressed RHEB in cells treated with a PI3K inhibitor localized to non-lysosomal endomembranes abutting lysosomes (Saito et al., 2005). Peculiarly, the compartment where inactive (GDP-bound)

RHEB was thus reported to be found is more reminiscent of the domain where we observe RHEB under conditions when mTOR signaling is active and RHEB is therefore predicted to be GTP bound. The reasons for these discrepancies are unknown. In addition to possible cell-specific differences, the use of overexpressed proteins might itself artificially influence localization.

Several observations suggest caution is warranted when interpreting results of experiments based upon overexpressed RHEB. First, Saito and colleagues found that overexpression of RHEB and RHEB2 (*RHEBL1*) induced the formation of multiple very large endocytic (lysosome-like) vesicles. That such large vesicles seem absent or much fewer in non-transfected cells questions the physiologic nature of these vesicles and trafficking to them. Secondly, overexpressed wild-type RHEB proteins initially localized to non-lysosomal membranes in this study prior to late lysosomal localization. This could reflect normal vesicular trafficking. Alternatively, non-physiologic levels might saturate normal compartments, overwhelm processing steps known to be required for proper localization of RHEB (Hanker et al., 2010), or alter membrane compartment physiology causing targeting for recycling through lysosome fusion. (Indeed, our ability to rescue mTORC1 signaling from acid relies on and demonstrates an ability to drive atypical localization of RHEB through overexpression). Consistent with existence of such confounders, our own experience with LysoTracker dye, a means to label the acidic lumens of lysosomes without exogenous protein overexpression, and an informal survey of literature and web images depicting use of this reagent suggest the atypicality of such large lysosomal structures, including for the same cell lines (Bobak et al., 2017). Similar reservations might extend to the majority of reports on RHEB localization due to their same reliance on overexpressed RHEB without corroborating visualization of endogenous RHEB (Buerger et al., 2006). Nonetheless, if this GTP status-dependent

compartmentalization of RHEB asserted by Saito and colleagues is validated, this would interestingly suggest RHEB might alter its membrane localization in response to activation, echoing similar signaling-induced relocation of mTOR (Sancak et al., 2008) and TSC2 (Menon et al., 2014). However, as RHEB possesses a farnesylated tail that anchors it in membranes (Hanker et al., 2010), how such rapid relocation would be achieved is not immediately clear and would perhaps require release of this anchor or endomembrane fusion events.

Future study is needed to integrate the above reports and clarify the localization of RHEB and whether such localization varies across cell lines. High resolution immunofluorescence microscopy using reliable antibodies to endogenous RHEB, such as the one we have employed, could be complimented by immunoprecipitation, organelle isolation, and electron microscopy or cryotomography techniques. Perhaps differential localization of RHEB exists across cell types, reflecting differing functionalities of cells and consequently differing quantities and character of endomembranes. Differential RHEB localization might endow differential mTORC1 sensitivity to sensed environmental parameters or regulate where in the cell mTORC1 and its downstream substrates become activated. Indeed, if some cell types possess RHEB constitutively anchored to lysosomes, as popularly believed, our model would predict mTORC1 signaling in these cells to be insensitive to acid. Admittedly, it is difficult to distinguish the location from which RHEB contacts and activates mTORC1 from compartments the protein is trafficked through during protein and endomembrane maturation. Reconstitution of RHEB knockout cells with mutant RHEB constructs targeted to specific organelles could clarify these ambiguities.

### *Tumor cell mTORC1 suppression by acidic microenvironment*

Our *in vitro* data showing acid to be sufficient to inhibit mTORC1 signaling and our *in vivo* data indicating rescue of mTORC1 signaling with bicarbonate treatment suggest mTORC1 signaling is inhibited in acidic regions of tumors. Consistent with this interpretation, sodium bicarbonate supplementation of mouse drinking water did not significantly alter expression of a HIF target (carbonic anhydrase 9, CAIX) (Figure 12), suggesting rescue of mTORC1 signaling with bicarbonate therapy occurs through elevation of intratumoral pH rather than an effect on upstream HIF signaling or perfusion.

Figure 12

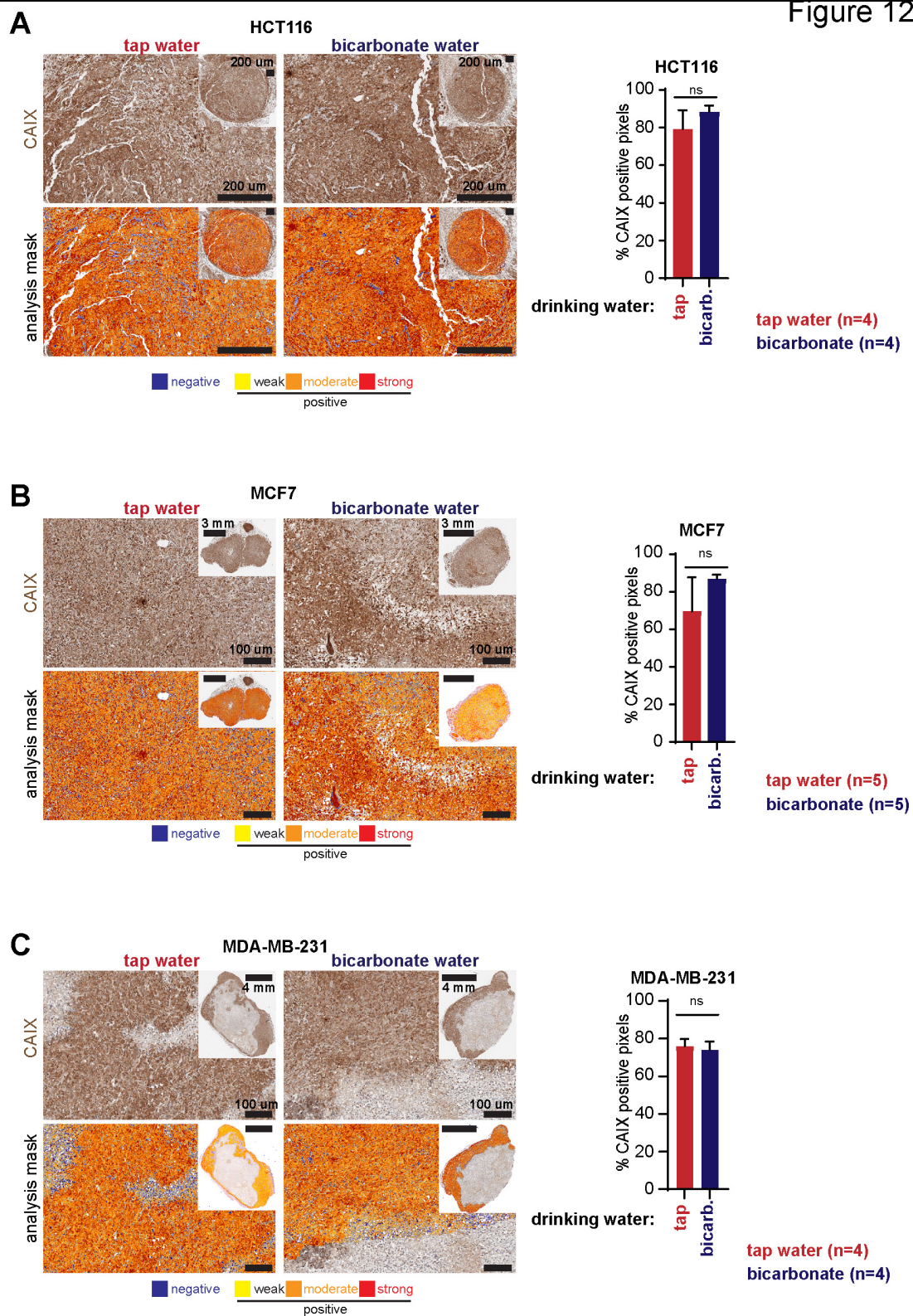


**Figure 12 – Bicarbonate therapy rescues mTORC1 signaling downstream of HIF.**

**A.** Immunohistochemical carbonic anhydrase IX (CAIX) staining of HCT116 xenograft tumors carried by host mice drinking normal tap water or 200 mM sodium bicarbonate *ad libitum* throughout tumor hosting (up to 3 weeks). Representative high-power fields with inset low-power images of entire tumor cross section. Positivity mask in lower panels. Percent CAIX positive pixels quantified over entire viable area of tumor cross section. Mean $\pm$ SD n=4 mice each arm. 2-tailed Student's t-test. **B/C.** Immunohistochemical CAIX staining of cross sections of MCF7 (B) and MDA-MB-231 (C) xenograft tumors carried by host mice drinking normal tap water or 400 mM sodium bicarbonate *ad libitum* from 3 days post tumor cell inoculation through tumor harvest (five weeks later). Representative images and quantification as in A. Mean $\pm$ SD, n=5 mice (B) or 4 mice (C) for each arm. 2-tailed Student's t-tests, ns=not significant. Same tumors stained for pS6 in Chapter 2 Figure 7 K and Supporting Figure 7 L-M.

We decided to use our xenograft model of B cell lymphoma (P493) to determine if additional evidence indicative of tumor acidity suppressing mTORC1 signaling *in vivo* could be obtained (Figure 13). We first determined whether mTORC1 signaling could be inhibited by low pH in this cell line *in vitro* and confirmed that, like all the other cell lines explored over the course of this study (U2OS, 293T, HCT116, MCF7, MDA-MB-231, MEFs), mTORC1 signaling in these cells was sensitive to inhibition by acid (Figure 13A in comparison to figures in Chapter 2 - Results). We then formed xenografts with the P493 line and noted that the percentage of cells positive for phospho-S6 (pS6) by immunofluorescence diminished with tumor size, with parallel assessment of a rapamycin-treated mouse confirming the specificity of our quantitative assessment (Figure 13B). As larger tumors would be anticipated to be larger because of higher rates of proliferation, lower mTORC1 signaling in larger tumors is counterintuitive and therefore perhaps is suggestive of mTORC1 suppression by increased hypoxia and acidity as larger tumors outstrip diffusion and perfusion. Indeed, further immunohistochemical assessment suggested a gradient of pS6 such that the viable tissue at the core of the tumor was nearly devoid of pS6 staining while the periphery featured high pS6 staining (Figure 13C). Solid tumors have been shown to likewise feature oxygen, lactate, and pH gradients, with the center and other regions remote from blood supply being most severely hypoxic and acidic ((Gallagher et al., 2008; Gillies et al., 2002; Manzoor et al., 2008; Sattler et al., 2007); in particular, Figure 4B in Gallagher et al., Figure 6C in Sattler et al., and Figure 1 in Manzoor et al.) . Indeed, when we took steps to attempt to quantify the three-dimensional distribution of pS6 immunofluorescence in 13 tumors (with careful exclusion of necrotic areas), we saw a clear reduction in pS6 intensity with radial distance from the tumor surface, again with specificity confirmed by analysis of a rapamycin-treated mouse (Figure 13 D-E).

To independently corroborate these observations, we turned to a second tumor model, an orthotopic pancreatic tumor model (PANC02). In addition to pS6, we stained for a HIF target (carbonic anhydrase IX, CAIX) as a marker of hypoxic regions and saw a striking inverse spatial correlation between pS6 and this HIF target (Figure 13F), consistent with suppression of mTORC1 in regions featuring hypoxia-stabilized HIF (and therefore HIF-mediated anaerobic glycolysis), and consistent with observations of others (He et al., 2016). Thus, both P493 and PANC02 tumors reveal data consistent with mTORC1 suppression *in vivo* in the anticipated hypoxic and acidic regions of the tumor microenvironment.

Figure 13

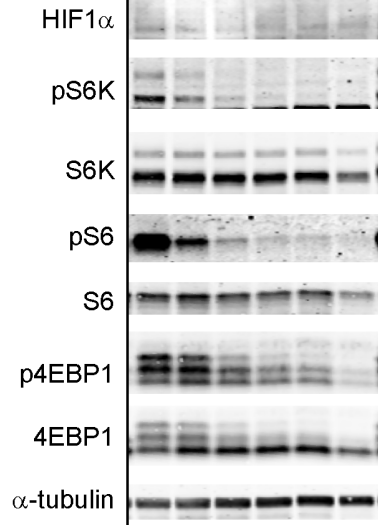
**A**

P493 *in vitro*

24 hours

media pH:

7.4 7.0 6.8 6.6 6.5 6.3



**B**

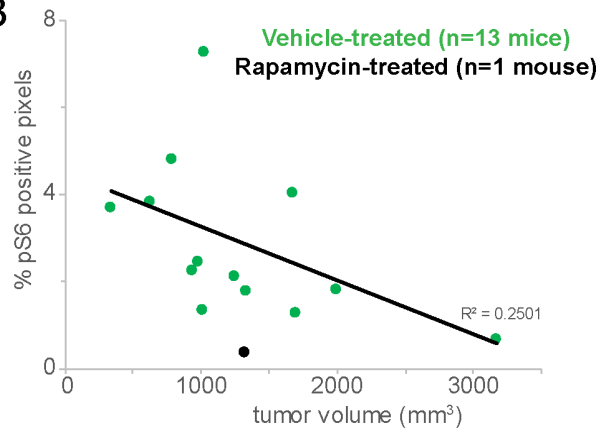
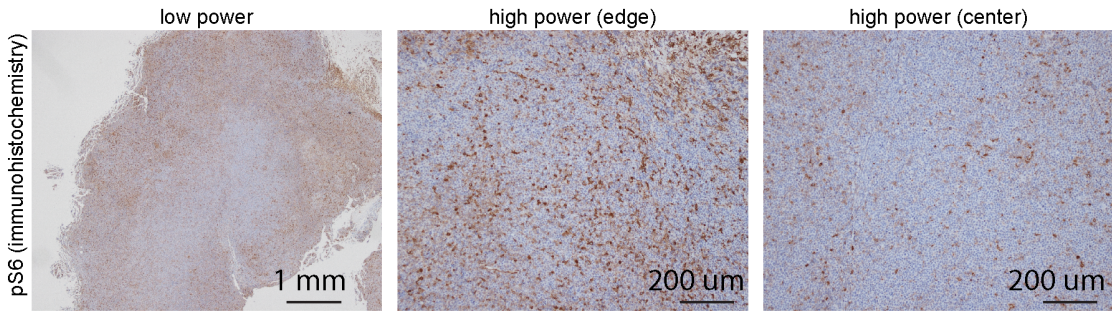


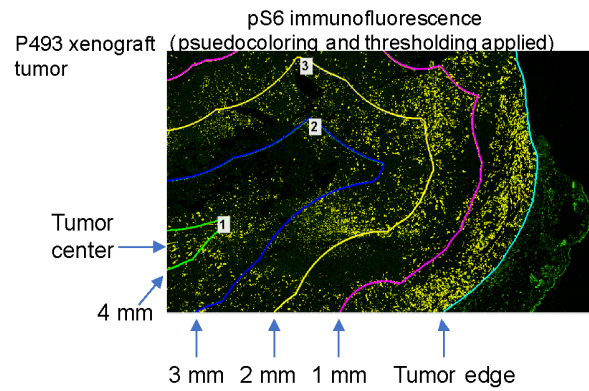
Figure 13 (continued)

C

P493 xenograft tumor



D



E

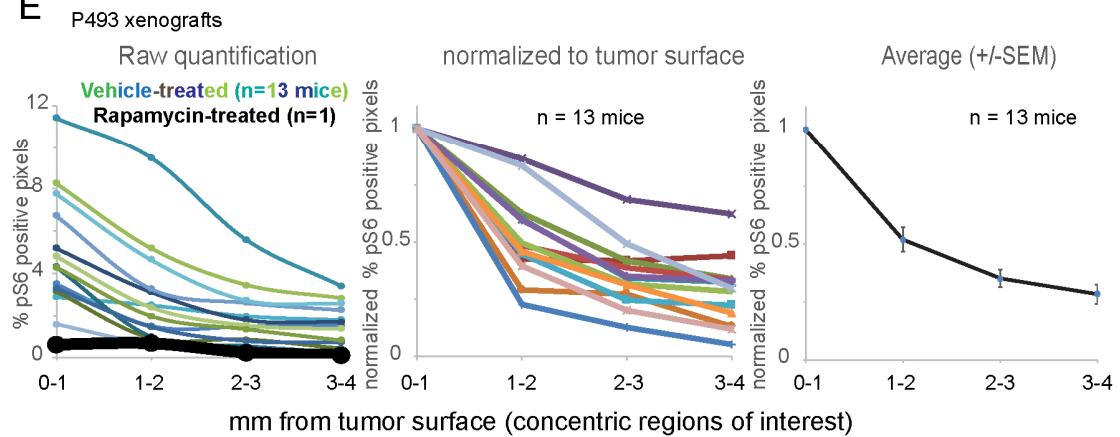




**Figure 13- mTORC1 signaling is low in anticipated hypoxic and acidic regions of two tumors models *in vivo*.**

**A.** Immunoblot for mTORC1 signaling and HIF1 $\alpha$  using lysate collected from P493 cells treated with media of the indicated pH for 24 hours *in vitro*. **B.** Percent phospho-S6 (Ser235/236, pS6) immunofluorescence positive pixels in cross sections of P493 tumor xenografts from control (n=13) or rapamycin-treated (n=1) mice as function of tumor volume (see methods). **C.** Representative immunohistochemical staining of P493 xenograft tumors for pS6. Low power image (left) with high power fields at tumor edge (middle) and tumor center (right). **D.** Schema for quantification in E. P493 xenograft tumors from control or rapamycin-treated mice were immunostained for pS6 by immunofluorescence protocol. Necrotic areas identified via comparison to hematoxylin and eosin stained adjacent sections were excluded from analysis. Tumor edge was demarcated and percent of pixels positive for pS6 was calculated in concentric regions of 1 mm width as depicted. Positivity threshold was determined by measurement of non-cytoplasmic (background) signal in representative region. **E.** Percent pS6 positive pixels as a function of radial distance from tumor edge (as described in D) for tumors from 13 mice. Data presented as raw quantification (left) and after normalization to outermost shell (0-1 mm) (middle). Mean $\pm$ SEM of normalized data shown at right. Raw quantification of tumor from rapamycin-treated mouse shown for comparison (black heavier line in left plot). **F.** Immunohistochemical staining for carbonic anhydrase IX (CAIX) and pS6 using adjacent sections of four PANCO2 orthotopic murine pancreatic tumors. Lower panel shows regions of interest

(white boxes) enlarged at right.

The above data suggest tumor acidity can dampen mTORC1 signaling in tumor cells. Future work using fluorescent or bioluminescent circadian reporters in tumor xenograft cells holds the promise of revealing whether such mTORC1 suppression contributes to clock dampening in tumors. Interest in discerning whether such dampening can be rescued with bicarbonate therapy and the effect such clock reinstatement would have on tumors further motivates future study.

As mTOR directs biosynthetic activities in coordination with nutrient availability and growth factors, we suspected this inhibition of mTORC1 signaling in acidic regions of tumors might suppress tumor cell growth. However, immunohistochemical staining for Ki67 in our P493 xenografts revealed high Ki67 even in regions featuring low pS6 (Figure 14), suggesting that even highly proliferative tumors such as this one can feature regional suppression of mTORC1. This surprising result may be consistent with published reports suggestive of a model by which mTOR suppression in hypovascular areas promotes a switch to macropinocytosis which supports proliferation despite low mTORC1 activity (Palm et al., 2015). This complex relationship between mTORC1 inhibition and proliferation requires further study in this and additional tumor models.

Figure 14

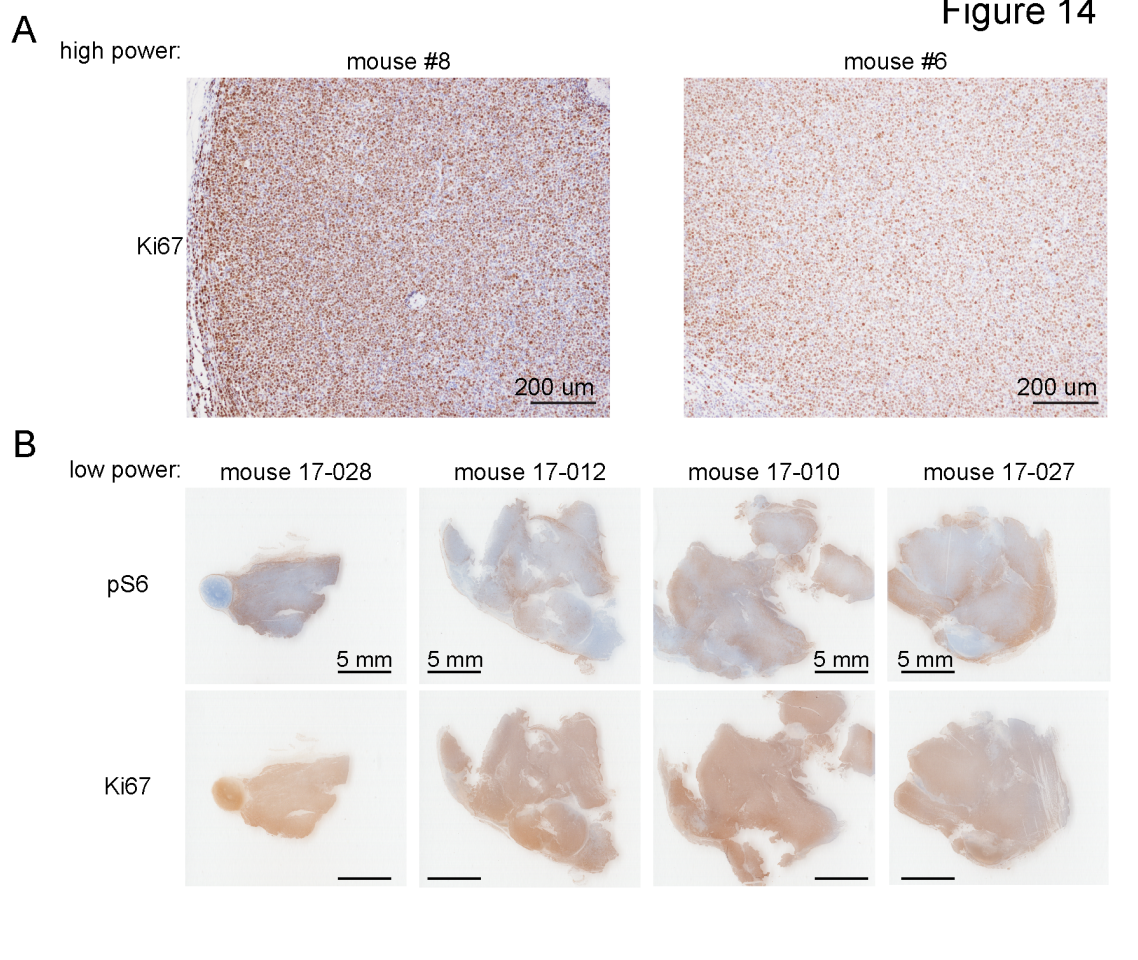


**Figure 14- Markers of proliferation remain uniformly high in P493 tumor xenografts despite regional dampening of mTORC1 signaling.**

**A.** Representative immunohistochemical staining of P493 tumor xenografts for Ki67. Two tumors shown. **B.** Low power images of immunohistochemical staining for pS6 and Ki67 using adjacent tumor sections from four additional P493 xenograft tumors.

### *Advantage of clock loss*

The ability of a tumor microenvironmental parameter to suspend the circadian clock motivates future inquiry into whether and how such clock suppression might enhance the hypoxic response or contribute to cancer cell behavior. Because of the many targets and processes under control of the clock, we speculate that shutting down the clock through mTORC1 inhibition in hypoxia is an efficient means for the cell to rapidly dampen many homeostatic energy-costly programs. This tempering of cell activities might permit the cell to better endure the period of limited metabolic and energy resources. It may also allow the stress response program to run without temporal limitation to fulfill the acute need. When stress becomes chronic, as in the acidic tumor microenvironment, oncogenes might be permitted to run a malignant program likewise freed from clock-dictated constraints. Therefore, reinstallation of a clock may prove to offer some tumor suppressive capacity. Regardless, the disruption of the temporal profile of many clock-controlled targets in acidic tumor cells should allow identification of optimal treatment times corresponding to when the therapeutic window over normal tissue is maximal and therefore promising of greatest efficacy and least toxicity.

To test the idea that suppression of the clock in response to hypoxia and acid has adaptive qualities, survival and growth rates of cancer cells with mTORC1-governed translation that is partially (4EBP1 knockout) or fully (RHEB overexpression) resistant to suppression by acid could be assessed *in vitro* or *in vivo* (xenograft) relative to wild-type cells. Combination with BMAL1 knockout could identify specifically if a running clock hinders cancer cell adaptation to tumor microenvironmental stress.

### *Immune cell mTOR inhibition by acidic tumor microenvironment*

Our work also has potential implications for cancer immunotherapy, suggesting the acidic tumor microenvironment might shut down mTOR signaling critical to T cell function. Lymphocytes have long been recognized to alkalinize  $\text{pH}_i$  upon stimulation (Gerson et al., 1982). More recently, mTORC1 has been revealed to play a critical role in the differentiation and activation of  $\text{CD4}^+$  and  $\text{CD8}^+$  T cells (Pollizzi et al., 2015; Pollizzi et al., 2016; Powell et al., 2012). For instance, pharmacologic or genetic inhibition of mTORC1 signaling prevents differentiation of  $\text{CD8}^+$  T cells into effector cells (Pollizzi et al., 2015; Rao et al., 2010) and  $\text{CD4}^+$  T cells into Th1 and Th17 subtypes (Delgoffe et al., 2011). Several reports have noted without mechanistic explanation that acidic media reversibly suppresses T cell cytokine production and cytolytic abilities *in vitro* (Brand et al., 2016; Calcinotto et al., 2012; Fischer et al., 2007; Pilon-Thomas et al., 2016), and raising the  $\text{pH}_e$  of *in vivo* tumor models with buffer therapy or a proton pump inhibitor enhances responses to both checkpoint inhibition and adoptive immunotherapy (Calcinotto et al., 2012; Pilon-Thomas et al., 2016). Correspondingly, the potent suppression of mTORC1 signaling by acid observed by us in  $\text{CD8}^+$  and  $\text{CD4}^+$  cells might be the mechanism behind acid's suppressive effects on T cells. Consistent with this, suppression of  $\text{IFN}\gamma$  production in acid was noted to be reversible and posttranscriptional in a manner suggestive of a translational block (Fischer et al., 2007; Pilon-Thomas et al., 2016). Indeed, rapamycin has been used for decades for its immunosuppressive function.

The peripheral redistribution of lysosomes in acid that we document suggests microtubule-based vesicle trafficking events critical to T cell function might also be disturbed in the acidic tumor microenvironment. After engaging an antigen presenting cell, the MTOC of the naïve T cell moves beneath the immune synapse (point of T cell

receptor (TCR) engagement) and additional TCR receptors are delivered in a dynein-dependent manner. Additionally, when a cytolytic T cell encounters a target cell, lytic granules (a lysosome-related organelle) are delivered to the MTOC through retrograde movement for release of their contents (de la Roche et al., 2016). Moreover, asymmetric partitioning (i.e. microtubule-directed trafficking) of fate-determining proteins amongst daughter cells after antigen-stimulated cell divisions gives rise to memory and effector lineages of CD8<sup>+</sup> T cells (Pollizzi et al., 2015). Therefore, it is conceivable that acid-mediated antegrade redistribution of vesicles and proteins could hinder activation, differentiation, and effector abilities of T cells and thereby enhance tumor escape from immune-mediated clearance. Consistent with this, in previous studies of T cell culture in acid, perforin content was not only noted to be lower (Fischer et al., 2007) but degranulation was also reversibly suppressed (Calcinotto et al., 2012). Given the acidic nature of the solid tumor microenvironment, acid neutralizing tactics might thus be helpful adjuvants to traditional cancer therapeutics and newer anti-cancer immunotherapies through restoration of mTORC1 signaling and proper vesicle trafficking in immune cells.

Thus, setting off to understand the interplay between hypoxic metabolism and the circadian clock, we have surprisingly come to understand new or previously overlooked fundamental and unanticipated features of a well-known key regulator of metabolism, which curiously, we realize in retrospect, was known to *time* metabolism to match environmental fluctuations in its own right. Given the centrality of the players—pH, the clock, mTOR—the future directions are numerous.

## CHAPTER 4 – Materials and Methods

### Experimental Model and Subject Details

#### Cell Lines

U2OS cells and clonal U2OS cells stably expressing *Arntl*::dLUC or *Per2*::dLUC (Zhang et al., 2009) were kindly provided by Drs. Roger Greenberg and John Hogenesch, respectively, and authenticated and confirmed free of mycoplasma by us. TSC2 knockout and wild-type p53 <sup>-/-</sup> MEFs (originally from the laboratory of Dr. David Kwiatkowski (Zhang et al., 2003)) and 293T cells were provided by Dr. Celeste Simon. Sestrin triple knockout 293T cells were provided by Dr. David Sabatini. MDA-MB-231 cells used in *in vitro* studies were provided by Dr. Donald Ayer and confirmed free of mycoplasma by us. MCF7 and HCT116 cells used *in vitro* studies were originally purchased from ATCC. U2OS, MDA-MB-231, and MCF7 cells are female. HCT116 is male.

All U2OS, 293T, and MEF cell lines were maintained in standard DMEM (4 mM L-glutamine, 25 mM glucose; Corning MT10-013-CV) supplemented with 10% fetal bovine serum (HyClone) and 1x penicillin/streptomycin (Corning) in standard humidified 5% CO<sub>2</sub>, 37 °C tissue culture incubators. MDA-MB-231 cells used for *in vitro* study were further supplemented with 1x MEM non-essential amino acids (Gibco). HCT116 cells were maintained in DMEM/F12 media (Gibco) supplemented with 1x penicillin/streptomycin and 10% newborn calf serum (HyClone). P493-6 were maintained in RPMI 1640 (Corning) supplemented with 10% FBS (Hyclone) and 1x penicillin/streptomycin (Corning) in standard humidified 5% CO<sub>2</sub>, 37 °C tissue culture incubators.

Generation of additional U2OS cell lines and experimental culture conditions described below.

HCT116, MCF7, and MDA-MB-231 cells used in *in vivo* work were purchased from ATCC, authenticated by short tandem repeat analysis, and confirmed to be free of mycoplasma. P493-6 cells used in *in vivo* work were likewise confirmed free of mycoplasma. Further details pertaining to these cell lines are detailed below in the description of this *in vivo* work.

### Animal Models

Primary T-cell cultures were sourced from C57BL/6 mice with *loxP*-flanked *Tsc2* alleles and *Cd4-Cre* (*Tsc2<sup>fl/fl</sup> Cd4-Cre*, resulting in TSC2 selectively deleted in T cells, “TSC2 -/-”) or without *Cre* (*Tsc2<sup>fl/fl</sup>*, “TSC2 +/+”) or with OVA-specific CD8<sup>+</sup> T cells (OT-I) (Pollizzi et al., 2015). All relevant animal procedures were in accordance with the guidelines of the Institutional Animal Care and Use Committee (IACUC) at Johns Hopkins University. Male and female littermates were used for each experiment with sex matching accordingly. Mice were provided with food ad libitum in standard 12-hour light/dark housing.

Xenograft studies pertaining to bicarbonate treatment were performed in accordance with the guidelines of the IACUC of the H. Lee Moffitt Cancer Center using eight- to ten-week-old randomized mixed male and female severe combined immunodeficient (SCID) mice (Fox Chase SCID Beige mice, Charles River) or female nu/nu mice (Envigo) as hosts as detailed below in the description of this *in vivo* work. Mice were provided with food ad libitum in standard 12-hour light/dark housing.

For P493 xenograft studies, all animals were maintained in accordance with the guidelines of the Institutional Animal Care and Use Committee (IACUC) at The Wistar Institute. Xenografts were formed in 6- to 8-week old athymic female nude mice (Charles River).

### Primary cells

Cells from spleens and lymph nodes (“splenocytes”) were combined for all experiments. In summary, single-cell suspensions were created by mashing organs through a 70  $\mu$ M filter. Red blood cells were removed through ACK lysing (Quality Biological). Splenocytes from mice with TSC2  $-/-$  and TSC2  $+/+$  T cells were resuspended directly into experimental conditions as described below. Splenocytes from OT-I mice were resuspended in RPMI-1640 media (Corning 10-040) with 10% FBS (Gemini Bioproducts), 2 mM L-glutamine (Corning), 10 mM HEPES (Corning), 50  $\mu$ g/mL gentamycin (Quality Biological), 1x non-essential amino acids (Gibco), and 50  $\mu$ M beta-mercaptoethanol (Sigma) and stimulated with 100 ng/mL OVA peptide (Anaspec) for 48 hrs then expanded in 10 ng/mL IL-2 (Preprotech) for 4 days to generate previously activated T cells. Primary OTI cultures were maintained in standard humidified 5% CO<sub>2</sub>, 37° C tissue culture incubators media. Experimental culture conditions described below.

## **Method Details**

### Media formulations and culture conditions (cell lines)

DMEM media with four different buffering/pH characteristics were typically used for *in vitro* experiments employing cell lines. These medias were referred to as “low buffer,” “high buffer,” “pH 7.4” (i.e. neutral media), and “pH 6.3” (or pH 6.4, 6.5, 6.6, etc. as

indicated in figures and legends, i.e. acidic media). These media formulations are described below. Exceptions to use of these medias are also noted below.

#### Low buffer media

The real-time luminometers (LumiCycle instruments, described below) that continuously measure bioluminescence from cultured cells require a non-humidified and “atmospheric” CO<sub>2</sub> (i.e. non-elevated CO<sub>2</sub>) environment for proper hardware function. Therefore, the standard widely used media in these luminometers is DMEM with buffering capacity appropriately adapted for atmospheric (0.04% CO<sub>2</sub>) culture (Yamazaki and Takahashi, 2005). In detail, this is a phenol-red-free DMEM with 25 mM glucose, 4 mM L-glutamine (Lonza), 4.2 mM (350 mg/L) sodium bicarbonate (Gibco), 10 mM HEPES (Sigma), 5% FBS, and 0.25x penicillin-streptomycin (prepared by supplementation of USBiological D9812-05). This standard media is referred to as “low buffer” media. Media pH was adjusted to pH 7.4 prior to filter sterilization. Except where noted, this media was used in atmospheric CO<sub>2</sub> conditions.

#### High buffer media

“High buffer” media is the above “low buffer” media with the HEPES eliminated and the sodium bicarbonate increased to 44 mM (3.7 g/L). (Note, this is the bicarbonate concentration in standard DMEM used in routine 5% CO<sub>2</sub> culture.) This media was used at atmospheric CO<sub>2</sub> conditions or, if noted, in 5% CO<sub>2</sub>. When used at atmospheric CO<sub>2</sub> conditions, the bicarbonate concentration is in excess of that indicated by the Henderson-Hasselbalch equation to be required to achieve a physiologic pH (i.e. pH 7.4). This excess is deliberate and, in contrast to the above “low buffer” media, enables absorption of the anticipated acid load generated by glycolytic (hypoxic) cells. High

buffer and low buffer medias were prepared from the same concentrated common base to ensure identical composition in all other regards. Media pH was adjusted to pH 7.4 prior to filter sterilization.

#### pH 7.4 and pH 6.3-6.6 medias

A media of acidity comparable to that observed in solid tumors (pH 6.2-6.6) (Gallagher et al., 2008; Gillies et al., 2002) was desired. To enhance the pH-stability of such a media, the bicarbonate-HEPES buffering system of low buffer media (above) was replaced with 25 mM PIPES (pKa of 6.66 at 37 °C, effective buffering range pH 6.1-7.5 at 25 °C; Sigma). So as to allow this acidic media and its control physiologic pH media (pH 7.4) to share the same chemical composition, 25 mM HEPES (pKa 7.31 at 37 °C, effective buffering range pH 6.8-8.2 at 25 °C; Sigma H4034) was also added. Prior to filter sterilization, a concentrated PIPES-HEPES DMEM media base was split, adjusted to pH 7.4 or pH 6.3-6.6 (as noted in figures), and brought to volume, ensuring identical media composition of neutral and acidic media in all other regards. These medias were exclusively used in atmospheric CO<sub>2</sub>. While medias of pH 7.4, 6.5, and 6.3 were predominantly used, occasional figures and legends note the use of medias prepared to other pH values, including pH 6.6, pH 6.8, pH 7.0, pH 7.5, and pH 8 (e.g. Figs. 1I, S1F, 4A, S4A-C, S5E, S7J, and S7K).

#### Additional experimental culture details

L-glutamine (Lonza) was typically left out of all DMEM media preparations and added fresh immediately before use. Above medias were further supplemented with 1x non-essential amino acids when used for MDA-MB-231 *in vitro* experiments. After seeding, cells remained in standard humidified tissue culture incubators (5% CO<sub>2</sub>, 37 °C) in

normal DMEM for typically two days until experiment initiation and treatment with one of the above medias. To protect against desiccation during the course of experiments, all cells were cultured in humidified tissue culture incubators or sealed with autoclaved vacuum grease (Dow-Corning).

#### Media formulations and culture conditions (T cells)

For experimental manipulation of pH of splenocytes or purified T cell cultures, cultures were resuspended in RPMI-1640 (Sigma R1383 with 11.1 mM glucose restored) supplemented with 10% FBS (Gemini Bioproducts), 2 mM L-glutamine (Corning), 50 ug/mL gentamycin (Quality Biological), and 50 uM beta-mercaptoethanol (Sigma) in which the bicarbonate-CO<sub>2</sub> buffering was replaced with 25 mM PIPES and 25 mM HEPES. These cultures were maintained at 37 °C in atmospheric CO<sub>2</sub> in a humidified incubator. When prepared, a slightly concentrated media was split into multiple volumes before adjusting pH to target values, bringing to volume, and sterilizing by filtering, ensuring identical media composition in all regards other than pH. pH of stored media was frequently monitored to guard against drift and ensure correct record of experimental conditions.

#### Hypoxic culture

Hypoxic conditions (1% O<sub>2</sub>) were achieved by culturing cells in a humidified incubation box within a Coy Labs oxygen control glove box ("hypoxia chamber") capable of regulating both oxygen and CO<sub>2</sub> levels by mixing N<sub>2</sub> and CO<sub>2</sub> with ambient air. Normoxia refers to ambient 21% oxygen levels. Both normoxic and hypoxic arms of Fig. 1A utilized low buffer media in atmospheric CO<sub>2</sub>. Figure S1A used 5% CO<sub>2</sub> in all conditions, with high buffer media in normoxia and low buffer media in hypoxia. All other hypoxic cultures

and respective normoxic controls were in 5% CO<sub>2</sub> with media buffering as noted in figures.

#### Cell synchronization

Cells were synchronized in circadian time where indicated in figure legends by aspiration of media and replacement with fresh media containing 0.1 uM dexamethasone (Sigma) at time 0 (Altman et al., 2015). “Unsynchronized” if indicated emphasizes no dexamethasone exposure. All T cell experiments reflect “unsynchronized” cells. MCF7, HCT116, and P493 were unsynchronized in *in vitro* experiments.

In Figure 8 where desynchronized cells were explicitly studied “no dex” refers to the omission of dexamethasone from the pH 7.4 media. For the “No dex, no media change” arm, cells grew undisturbed for 5 days in pH 7.4 media without dexamethasone prior to timecourse start to avoid the synchronizing influence of media change. See further description below under timecourse design.

#### Luciferase reporter cell lines and monitoring

##### *Generation of real-time luciferase reporters*

Clonal U2OS *Arntl*::dLUC and U2OS *Per2*::dLUC cell lines (sourced as noted above) stably express firefly luciferase under the control of mouse *Arntl* or *Per2* promoters. The luciferase has been destabilized (“dLUC”) through addition of degradation sequences enabling it to serve as a real-time reporter of the activity of the clock network (Zhang et al., 2009). A portion of the *Arntl*::dLUC data shown and not shown was generated in a clonal cell line also stably expressing Renilla luciferase driven by an independent promoter. This line was generated by transfection (Lipofectamine LTX with Plus reagent,

Promega) followed by 150 ug/mL hygromycin selection (Corning) for a vector in which the SV40 promoter from pGL4.73 (Promega) was inserted in front of destabilized Renilla (*hRlucCP*) in pGL4.78 (Promega). Derivation of a representative clone by serial dilution allowed cessation of antibiotic selection. This control reporter enabled early characterization and validation of the clock reporter. However, the luciferase activity data shown in this paper exclusively represent the luciferase activity of the firefly luciferase clock reporter, as only the substrate for this enzyme (beetle luciferin (Promega), which is not a Renilla luciferase substrate) was supplied regardless of Renilla status. Experiments (shown and not shown) employing *Arntl*::dLUC cells both with and without renilla expression demonstrated that the background presence of this control enzyme had no effect on the presented data. Therefore, both cell lines are referred to here as U2OS *Arntl*::dLUC for simplicity.

*PGK1-HRE*::dLUC and *VEGF-HRE*::dLUC real-time luciferase-based reporters of hypoxia response element (HRE) activity were generated by inserting three copies of an HRE motif derived from the human *PGK1* promoter (lifted from HRE-pGL2-TK (Li et al., 2014)) or five copies of an HRE motif from the human *VEGF* promoter (derived from 5HRE/GFP (a gift from Martin Brown and Thomas Foster, Addgene plasmid #46926)) into the promoter region of destabilized firefly luciferase (*Luc2CP*, “dLUC”) in the puromycin-selectable vector pGL4.22 (Promega) and confirmed by sequencing. Stable cell lines expressing an *HRE*::dLUC luciferase reporter and the control Renilla reporter described above were generated in U2OS cells through co-transfection of cells plated in 6-well dishes with 1.25 ug of each plasmid using Lipofectamine LTX with Plus reagent followed by 1.5 ug/mL puromycin (Gibco) and 150 ug/mL hygromycin selection simultaneously (*PGK1*::dLUC) or sequentially (*VEGF*::dLUC). Single-cell clones of the

*HRE::dLUC*, *SV40::hRlucCP* reporters representative of the population were derived by serial dilution and antibiotic selection ceased. As above, the data presented in this paper reflect luciferase activity exclusively of the firefly luciferase reporter as only substrate for this enzyme was supplied. Thus, these lines are referred to as *PGK1-HRE::dLUC* and *VEGF-HRE::dLUC* for simplicity.

#### *Real-time monitoring of luciferase reporters*

Reporter cells were plated in 35 mm dishes or 24-well plates to be confluent at the start of analyses. For example, typically 375,000 U2OS cells per 35 mm dish or 62,500 cells per well of a 24-well plate were seeded two days prior. At time zero, culture plates were aspirated, administered fresh media supplemented 0.1  $\mu$ M dexamethasone and 0.1 mM beetle potassium luciferin (Promega), sealed against desiccation with vacuum grease (35 mm dishes) or adhesive optical PCR plate film (24-well plates, Applied Biosystems), and immediately placed in a Lumicycle-32 or Lumicycle-96 luminometer (Actimetrics). Luminescence (counts/sec; “relative light units (RLU) per second”) was recorded every 10 minutes for multiple days and exported to Excel (Microsoft) with LumiCycle Analysis software (Actimetrics). If monitored cells were treated with chemical inhibitors, these were added to the media at time zero; if siRNA treated, except where noted, siRNA was delivered the day prior as described below and in legends. Depicted “washouts” were achieved by temporary removal of a plate from the Lumicycle and media replacement. All Lumicycle data are generated in atmospheric CO<sub>2</sub> conditions for reasons noted above. All data are presented as raw data with no detrending. Reported amplitudes for Torin treatments (below) represent the mean peak-to-peak amplitude over four days manually calculated from the mean luminescence of biological triplicates (as in Figures

4I, S4N) as the difference between a peak and the following trough beginning 1 day after synchronization.

#### *Lysate luciferase assay*

The photon-producing luciferase reaction requires oxygen as a reactant and is therefore susceptible to suppression of enzymatic rate in hypoxia. Therefore, we did not monitor luminescence in real-time in hypoxia. Instead, lysate was collected from hypoxic (1% O<sub>2</sub>) and normoxic control plates at time points and then subsequently assayed for luciferase activity in normoxia. In brief, reporter cells were plated in 35 mm dishes as above. Where indicated in legends, the following day, media was placed in the hypoxia chamber overnight in flasks to permit pre-equilibration. Media was similarly allowed to equilibrate in normoxia for control arms. The following day, cells were brought to the hypoxia chamber (or normoxic incubators) and media was exchanged for (pre-equilibrated) media supplemented with 0.1 uM dexamethasone. At time points, cells were rinsed once with PBS and then lysed by scraping in 500 uL passive lysis buffer (Promega E1501). Cleared supernatant was then frozen at -80 °C until assay by luminescence with the Luciferase Assay System (Promega) in 96-well format on a GloMax 96 microplate luminometer (Promega) or Biotek Synergy HT microplate reader.

Luciferase assay of cell lysates was also used to verify live-cell real-time luminescence data (Fig. S1C-D). 13,000 U2OS *Arntl*::dLUC cells per well were plated in opaque 96-well culture plates. Beginning two days later, a reverse timecourse was initiated by synchronizing wells in triplicate in staggered fashion. Media contained luciferin allowing luminescence from live cells to be measured with the same microplate luminometer immediately prior to lysis of cells and luciferase assay directly in the plate with the

Luciferase Assay System. In Fig. S1C-D, low buffer is in atmospheric CO<sub>2</sub> and high buffer media is in 5% CO<sub>2</sub>.

### Single-cell luminescence imaging

#### *Cell culture*

Frozen *Arntl::dLUC* U2OS cells were received by the Welsh lab on dry ice from the Dang lab and thawed. Cells were grown in 35 mm cell culture dishes in DMEM cell culture medium with 10% heat inactivated fetal bovine serum (GIBCO), 1x MEM non-essential amino acids, and 1x penicillin-streptomycin in a humidified atmosphere of 5% CO<sub>2</sub> at 37 °C. Cells were imaged at 30% confluence to allow for clear visual discrimination of single cells.

#### *Imaging*

Immediately before imaging, medium was replaced with PIPES/HEPES-buffered media adjusted to pH 6.3, 6.8, or 7.4 and containing 1 mM luciferin and 0.1 uM dexamethasone prepared as described above but with the serum replaced by 1X B-27 (Gibco). Imaging was conducted in two darkrooms, each with a slightly different camera and temperature control setup. In both darkrooms, plates were sealed and placed on an inverted microscope stage (Olympus IX71) within a heated lucite chamber (Darkroom 1: Solent Scientific, UK; Darkroom 2: Precision Control Systems, Eden Prairie, MN) at a constant temperature of 36 °C. Light from the samples was collected using an Olympus 4x XLFLUOR objective (NA 0.28) and transmitted to a CCD camera (Darkroom 1: Spectral Instruments SI800, Tucson, AZ, USA; Darkroom 2: Andor Technologies DU934, Belfast, UK) cooled to -90 °C. Noise was reduced by 4x4 pixel binning. Exposure was set to 12

min, and images were collected at 30 min intervals for 4 days. Further details in published methods (Welsh et al., 2005; Welsh et al., 2004).

### *Image processing*

Cosmic ray artifacts were removed in MetaMorph (Molecular Devices, Sunnyvale, CA) by taking the minimum value of pixelwise comparison of consecutive images. Luminescence intensity was measured in a manually defined region of interest (ROI) for each cell. ROI positions were adjusted to accommodate cell movement. Seven to ten cells were analyzed per plate (10 cells per plate at pH 7.4, fewer (7-9 cells per plate) for pH 6.3 due to cell death). Criteria for cell selection were that cells had to survive the course of the experiment and cells could not touch other cells to the point that they could not be tracked. Luminescence intensity values and ROI areas were logged in Microsoft Excel, and intensity was converted to analog-to-digital units (ADU) according to the following equation:

$$\text{ADU} = (\text{luminescence intensity} - \text{background intensity}) \times \text{ROI area}$$

Background intensity was set as the minimum luminescence intensity recorded across all cells for each experiment.

### *Determination of rhythmicity*

To exclude high initial luminescence transients, the first twelve hours of data were excluded. Luminescence values between 0.5 and 3.5 days, for a total of 72 hours of data, were analyzed for each experiment. To determine average brightness of each cell, mean ADU was computed across 0.5 to 3.5 days. Luminescence time series were imported into LumiCycle Analysis. To determine period, phase and amplitude, data were

fitted to a best fit sine curve corrected for dampening. Circadian rhythmicity was determined by the fast Fourier transform (FFT) peak, or percent of total variance within the circadian range corresponding to 20-36 hour periods. The scatter plot was obtained by plotting FFT peak against period. FFT peak value of 0.07 was chosen to exclude period values that were clearly outside the typical circadian range. Cells with FFT peak  $\geq$  0.07 were considered to be rhythmic. Percent rhythmic cells was computed for each pH value. Only rhythmic cells were analyzed for the below attributes.

#### *Analysis of circadian attributes*

After excluding data from cells with FFT peak  $< 0.07$ , the impact of equipment between the two darkrooms on average brightness, normalized FFT peak, period, phase and amplitude were investigated using a t-test for each pH. As expected with two different camera setups, only average brightness and amplitude were influenced. Consequently, average brightness and amplitude values were normalized by scaling to the maximum and minimum values found for each darkroom. We verified that our normalization method did not influence results by analyzing raw data from each darkroom individually before pooling normalized data from both darkrooms. As values for FFT peak, period and phase were unaffected by darkroom, raw data were pooled without normalizing for analysis of these metrics. An outlier was excluded when  $\alpha \leq 0.05$  (Grubb's test). Significance was found by running ANOVA and post-hoc Dunnett's multiple comparison tests comparing pH 6.8 and pH 6.3 to the control (pH 7.4).

#### CRISPR-editing

*EIF4EBP1* (4EBP1) and *TSC2* were silenced in U2OS *Arntl::dLUC* cells through CRISPR editing using pSpCas9(BB)-2A-GFP (PX458) (a gift from Feng Zhang, Addgene

plasmid #48138) with sgRNA sequences from the GeCKO library (Shalem et al., 2014): TGAAGAGTCACAGTTTGAGA for *EIF4EBP1* and TCTGCTGAAGGCCATCGTGC for *TSC2*. Oligos were phosphorylated, annealed, and ligated into the PX458 backbone, which was then transformed into bacteria, isolated, and verified by sequencing. The empty PX458 vector was used as control. 1.15 million cells were seeded in 10 cm plates and the following day transiently transfected with 5 ug of plasmid using Lipofectamine 3000 (Invitrogen) according to the manufacturer's directions. 24 hours later, GFP positive cells were sorted by FACS as single cells into 96-well plates. Resulting clonal lines were then screened by immunoblot for silencing of target. Because clones derived from the parental U2OS *Arntl::dLUC* line exhibit heterogeneity in intensity of luciferase expression (regardless of transfection), edited cell lines were matched to an empty vector clonal line determined to have similar luciferase expression in control (pH 7.4) conditions (#EV1\_16) for the convenience of more ready visualization of changes in amplitude of oscillation in response to experimental manipulations during real-time bioluminescence monitoring.

#### Stable overexpression

U2OS *Arntl::dLUC* lines stably expressing constitutively active RAGB or a control GTP-binding protein, RAP2A, were created by moving the flag-tagged inserts in Flag-pLJM1-RagB99L and Flag-pLJM1-Rap2A (gifts from David Sabatini, Addgene plasmids #19315 and #19311) (Sancak et al., 2008) into pcDNA3.1+ (Invitrogen) using NheI and EcoRI restriction sites and confirming by sequencing. 200,000 cells were seeded into 6-well plates and the following day transfected with 0.5 ng of linearized (BglII) plasmid using Lipofectamine 3000 and then selected with 600 ug/mL G418 (Corning) beginning two days later. Cells were maintained in selection until the initialization of experiments.

U2OS *Arntl*::dLUC lines stably expressing constitutively active RHEB (Urano et al., 2005) were similarly created by seeding 200,000 cells in a 6-well dish and the following day transfecting with 0.5 ng of sequence-confirmed pcDNA3-FLAG-Rheb-N153T (gift from Fuyuhiko Tamanoi, Addgene plasmids #19997) using Lipofectamine 3000. Beginning two days later, cells were selected with 800 ug/mL G418 followed by 400 ug/mL maintenance. Clones were derived by serial dilution and screened for expression of the transgene. As for CRISPR lines discussed above, a clone (#EV2\_6) also derived from U2OS *Arntl*::dLUC and transiently transfected with an empty vector (PX458) was designated a control for its similar baseline luciferase expression in pH 7.4 conditions. G418 selection was ceased after derivation of clones.

293T cells stably expressing WDR24 (a subunit of GATOR2) or a control protein (RAP2A) were created through lentiviral infection. 293T cells were seeded in 10 cm plates so as to be 75% confluent the following day when transfected with 3 ug of sequence-confirmed Flag-pLJM1-WDR24 or Flag-pLJM1-Rap2A (gifts from David Sabatini, Addgene plasmids #46337 and #19311) and 2.25 ug second-generation packaging plasmid psPAX2 and 0.75 ug pMD2.G envelope plasmid (gifts of Didier Trono, Addgene #12260 and #12259) using Lipofectamine 3000. Virus-containing supernatant was collected after 72 and 96 hours, filtered, concentrated with an Amicon Ultra-15 10K centrifugal filter device (Millipore), and used to transduce in the presence of 8 ug/mL polybrene (Millipore) subconfluent 293T cells seeded the day prior in 35 mm dishes. The following day, cells were trypsinized and expanded and 1 ug/mL puromycin selection was begun. Cells were maintained in selection until initialization of experiments.

U2OS *Arntl*::dLUC cells stably expressing a genetically-encoded cytoplasmic ratiometric pH probe, mCherry-SuperEcliptic (SE) pHluorin (a gift from Sergio Grinstein, Addgene plasmid #32001) (Koivusalo et al., 2010), were generated by seeding 250,000 U2OS *Arntl*::dLUC cells into one well of a 6-well plate and the following day transfecting with 1.25 ug of sequence verified mCherry-SEpHluorin using Lipofectamine LTX with Plus reagent. Beginning three days later, cells were selected with 400 ug/mL G418. After emergence of a stable line, fluorescence-activated cell sorting was used to derive a polyclonal population with mid-range brightness of the reporter to avoid reporter mislocalization from excessive expression. This line was maintained in selection until initialization of experiments.

#### pH measurements

##### *Extracellular pH*

Extracellular pH was determined by measuring the pH of a sample of culture media using the Mettler Toledo SevenGo pH meter SG2 with either the InLab micro probe or the InLab 413 SG/2m probe with automatic temperature compensation. These meters were also used to adjust the pH of media and other reagents as needed. The pH meter was recalibrated with 3 standards (Mettler Toledo 51302080) at the start of every experiment.

##### *Intracellular pH*

Intracellular pH was assessed by a method adapted from previous descriptions (Koivusalo et al., 2010) and the manufacturer-provided protocol for the intracellular pH buffer calibration kit (Invitrogen P35379). U2OS *Arntl*::dLUC cells stably expressing a genetically-encoded cytoplasmic ratiometric pH probe, mCherry-SuperEcliptic (SE)

pHluorin, in which the fluorescence intensities of the fused modified GFP (SE pHluorin) and mCherry are pH sensitive ( $pK_a = 7.2$ ) and insensitive, respectively, were generated as described above. 200,000 cells were plated in 6-well dishes and allowed to grow for two days in standard humidified tissue culture incubators (5%  $CO_2$ , 37 °C) in normal DMEM before treating with the inhibitors or medias for the duration indicated in figure legends. To generate a standard curve, each well of an untreated plate grown in parallel was washed twice with PBS and then incubated with a media pH standard (25 mM HEPES, 25 mM PIPES DMEM, pre-adjusted to pH 8.0, 7.5, 7.0, 6.5, or 6.0, as above) containing 10  $\mu$ M valinomycin and 10  $\mu$ M nigericin (Invitrogen) for 5 minutes in atmospheric  $CO_2$  at 37 °C before imaging. Alternatively, the same well was serially treated with each standard and imaged with similar results. Three or more 10x fields were captured from each standard using an Olympus IX81 inverted fluorescence microscope quipped with a 10X objective (UPLFLN10X2PH) and a cooled 12 bit CCD camera (Sensicam QE, PCO) controlled by SlideBook 6 software (e.g. S4B). Experimental plates (DMOG-treated, etc.) were subsequently likewise imaged with identical microscope hardware and acquisition settings (e.g. S4C). Images were then background-corrected in Fiji (Image J2, rolling ball background subtraction) before measuring the integrated intensity across the whole field (Schindelin et al., 2012). The ratio of the SE pHluorin (GFP) and mCherry intensities for each field was calculated. A standard curve (e.g. S4A) was generated relating the mean ratios of the standards to the pH of the standard (calibration) medias. The linear fit equation was used to calculate the intracellular pH of the experimentally treated plates (e.g. 4A). This described approach yielded similar results in validation experiments (not shown) as ratiometric assessment of regions of interest drawn within the cytoplasm of cells imaged under higher power (40x). Displayed images are uniformly contrasted.

### Chemical inhibitor treatments

Prior to treatment with inhibitors, 375,000 cells plated in 35 mm dishes were allowed to expand in normal DMEM in standard 5% CO<sub>2</sub> 37 °C incubators. Dose and duration of treatments are as indicated in legends. DMOG (Sigma) and vehicle (DMSO) treatment (regardless of buffer conditions) were in atmospheric CO<sub>2</sub>, except S1D and S4L where high buffer media was used in 5% CO<sub>2</sub> (and low buffer media was used in atmospheric CO<sub>2</sub>). All other chemical inhibitors (desferrioxamine (Calbiochem), GNE-140 (NCATS Chemical Genomics Center) (Boudreau et al., 2016), amiloride hydrochloride hydrate (Sigma) (Pouyssegur et al., 1982),  $\alpha$ -cyano-4-hydroxycinnamic acid (Sigma) (McBrian et al., 2013), Torin1 (Cayman), Torin2 (Cayman), rapamycin (Sigma), n-butanol and tert-butanol (Sigma) (Toschi et al., 2009), ciliobrevin D (Calbiochem) (Li et al., 2016), nocodazole (Cayman), A-484954 (Sigma) (Xie et al., 2015)), and cycloheximide (Sigma C4859) were used in standard low buffer media in atmospheric CO<sub>2</sub>.

Primary alcohols like n-butanol deplete phosphatidic acid required for mTORC1 signaling by substituting for water in phosphatidic acid synthesis pathways, effectively resulting in generation of phosphatidylalcohol at the expense of phosphatidic acid. Bulkier tertiary alcohols, like tert-butanol, do not efficiently participate in these transphosphatidyl reactions and therefore are used as a negative control (Toschi et al., 2009).

### Timecourse design

Each 48- or 52-hour timecourse with 4-hour intervals of RNA or protein lysate harvest was collected as a pair of staggered 24- or 28-hour parallel timecourses. Three days prior to the timecourse start, 375,000 U2OS *Arntl::dLUC* cells were seeded in 35 mm

dishes and allowed to grow in normal DMEM in 5% CO<sub>2</sub>. Twenty-four hours later, another set of plates was seeded in identical fashion. Twenty-four hours later, cells of the first set were then synchronized and treated with media of the indicated oxygen tension, pH, buffering capacity, or DMOG concentration. Twenty-four hours later, the second set of plates was synchronized and conditioned in identical fashion. For such timecourses in hypoxia, media was equilibrated overnight in the hypoxia chamber (and in parallel in normoxia) prior to relocation of cells to the hypoxia chamber and media exchange. Harvest of RNA or protein began at the indicated intervals with the 4-hour and 28-hour samples of each arm being collected together, followed by the 8-hour and 32-hour samples and so forth.

In Figure 8, where desynchronized cells were explicitly studied, pH 7.4 and 6.3 arms were set up as described above. The “no dex” arm refers to the omission of dexamethasone from the pH 7.4 media. For the “No dex, no media change” arm, six and five days prior to timecourse start (i.e. staggered timecourse beginning 3 days in advance of typical), cells were resuspended in pH 7.4 media containing no dexamethasone (but typical 5% serum) and seeded at 1/12 the typical density (to attempt to account for extra 3 days cells would be allowed to grow). Cells were permitted to grow in atmospheric conditions. No media change was made prior to lysate harvests beginning 5-6 days later. Lumicycle analysis was performed in parallel by adding luciferin to replicate plates.

#### Protein Immunoblotting

Following media aspiration, cells in 35 mm dishes were washed once with cold PBS and then harvested by scraping over ice in lysis buffer (Mammalian Protein Extraction

Reagent (Thermo Fisher Scientific) supplemented with protease inhibitor cocktail (Promega G6521), two phosphatase inhibitors (Sigma P5726, P0044), and, typically, prolyl hydroxylase inhibitor (200  $\mu$ M desferrioxamine)). (For Figure S1I, protein was instead harvested by trypsinizing cells, washing once in PBS, and resuspending in lysis buffer.) After collection of scraped cells and lysate (or after suspending cells in lysis buffer), lysis was allowed to continue on ice for at least 20 minutes. Protein lysates were cleared by centrifugation at 13,000 rpm at 4 °C and stored at -80 °C until further use. After thawing lysates on ice and quantifying protein yield with the DC Protein Assay (Bio-Rad), equal  $\mu$ g of total protein were resolved by SDS-PAGE using Criterion pre-cast Tris-Glycine 7.5% or 4-20% gradient gels (Bio-Rad). Protein was transferred by dry transfer (iBlot) to nitrocellulose membranes, which were then blocked in 5% BSA (Sigma) in TBST for 1 hour. Primary antibodies included anti-HIF1 $\alpha$  (Cayman; 1:500), anti- $\alpha$ -tubulin (Calbiochem; 1:10,000), anti-PER2 (Proteintech; 1:1000), anti-CRY2 (Epitomics, 1:500); anti-REDD1 (Proteintech; 1:1000), anti-EX2/3 (Clippinger et al., 2011) (1:6000), anti-kinesin-1 (Santa Cruz; 1:1000), anti-phospho-Thr202/Tyr204 of ERK1/2 (Cell Signaling; 1:2000), anti-RHEB (Abnova, 1:1000), anti-phospho Thr982 of PERK (lab of Constantinos Koumenis; 1:1000), and TXNIP (Abnova 1:2000). Primary antibodies against BMAL1, CLOCK, phospho-Ser2448 of mTOR, mTOR, phospho-Thr389 of S6K, S6K, phospho-Ser235/236 of S6, S6, phospho-Thr37/46 of 4EBP1, 4EBP1, 4EBP2, phospho-Ser209 of eIF4E, eIF4E, phospho-Thr56 of eEF2, eEF2, Sestrin-2, FLAG-tag, TSC2, phospho-Thr172 of AMPK $\alpha$ , AMPK $\alpha$ , phospho-Ser338 of c-Raf, c-Raf, ERK 1/2, phospho-Ser9 of GSK3 $\beta$ , RHEB, PERK, ATF4, CHOP, phospho-Ser51 of eIF2 $\alpha$ , and eIF2 $\alpha$  were all from Cell Signaling and used at 1:1000. Secondary antibodies included Alexa Fluor 790 goat anti-mouse IgG (H+L) (Invitrogen; 1:10,000) and Alexa Fluor 680 goat anti-rabbit IgG (H+L) (Invitrogen; 1:8000). All antibodies were

diluted in blocking buffer. Immunoblots were imaged with Odyssey CLx infrared imaging system (LI-COR) and uniformly contrasted. See Appendix for product numbers of reagents.

Where quantification is reported, background-corrected band intensities were calculated with Image Studio software with background defined as the median intensity immediately above and below the quantified band. Immunoblots from the same gel are enclosed within a box with black outline. Yellow lines are for readability only. When reprobing for additional targets of closely separated molecular weights, membranes were stripped with stripping buffer (Thermo) to dim signal of first target to facilitate imaging. Except when reblotting for total protein (e.g. S6K) after phosphoblot (e.g. pS6K), reprobing for additional targets of similar molecular weight was avoided. Blots of tubulin loading controls appear in multiple figures when data from a single membrane were divided between these multiple figures for clarity of presentation.

#### Protein Immunoprecipitation

Starvations and subsequent immunoprecipitation proceeded as adapted from previous descriptions (Wolfson et al., 2016) and the manufacturer-provided protocol for Anti-FLAG M2 affinity gel (Sigma). 2 million 293T cells stably expressing FLAG-tagged WDR24 or RAP2A (described above) were seeded in 10 cm plates and allowed to expand in normal DMEM in 5% CO<sub>2</sub>. Two days later, media was aspirated and cells were incubated for 50 minutes in 10 mL “starvation” conditions consisting of either amino acid free media (-AA) or leucine free media (-L) of pH 7.4 or pH 6.3 after washing twice with these respective medias. For “rescues,” one mL of 11x concentrated solution of amino acids (+AA) or leucine (+L) (in water) was spiked into plates so as to restore

amino acids to normal DMEM levels. (See starvation media descriptions below.) An equal volume of water was added to control (continued starvation) plates.

After 10 minutes, cells were washed once with cold PBS and then lysed with Triton lysis buffer (1% Triton X-100 (Sigma), 10 mM  $\beta$ -glycerol phosphate (Sigma), 10 mM pyrophosphate (Sigma), 40 mM HEPES pH 7.4, 2.5 mM  $MgCl_2$  (Sigma), and EDTA-free protease inhibitor (Roche, two mini tablets per 14 mL)) by scraping plates over ice. After 20 minutes incubation on ice, lysate was cleared. Anti-FLAG M2 affinity gel was washed three times in lysis buffer by resuspension. These resuspensions, and those during all subsequent washes, were performed by pipetting up and down with tips enlarged by cutting. 30  $\mu$ L of a 50:50 slurry of lysis buffer and gel were then added to each lysate (or to a volume of lysate diluted in lysis buffer to normalize input volume and total protein across samples). As a negative control, slurry was similarly added to lysis buffer. Lysate and resin then incubated rotating for 2 hours at 4°C. Resin was then washed once in lysis buffer and three times in lysis buffer containing 500 mM NaCl. Resin was then resuspended in 30  $\mu$ L 2x SDS loading dye with DTT (125 mM Tris-HCl pH 6.8, 4% SDS, 20% glycerol, 200 mM DTT, and 0.004% bromophenol blue), heated to 95 °C for 5 minutes, and resolved by SDS-PAGE as above. Note the Ig anti-FLAG heavy chain (visible in all lanes, including the no lysate control) appears to run just below sestrin-2 on immunoblots. Equal volume aliquots of cleared lysate (or diluted lysate) set aside prior to addition of resin were boiled in SDS loading dye in parallel and resolved on the same gel to reflect inputs.

#### Serum and amino acid starvations

Medias used for 293T or U2OS starvations were DMEM medias buffered in one of the manners described above but without the indicated amino acid(s) or serum. In detail, medias used for starvations in immunoprecipitations (S5C, S5D) or for Figure 5C were pH 7.4 and pH 6.3 media (buffered as described above) but without amino acids (USBiologic 9800-13 with 25 mM glucose and 1 mM pyruvate (Gibco) restored) or without leucine (USBiologic D9806-05, with 25 mM glucose and 4 mM glutamine restored). These medias were made with 5% undialyzed (full) FBS (HyClone), so are more accurately “near-starvation” conditions. For all other amino acid starvation experiments, medias were formulated from USBiologic 9800-13 with appropriate restorations and 5% (or 10% in Figure 5B) dialyzed serum (Gibco; making them complete amino acid starvations), with Figure 5B and 6J using buffering/pH as in pH 7.4 and pH 6.3 media and all others using buffering as in low buffer media (described above). Prior to incubation in starvation media, cells were washed at least twice in starvation media. Where applicable, “no starvation” controls were similarly washed with replete media. All amino acid rescues used 11x concentrates of amino acid(s) (made from powders (Sigma)) such that addition of a volume equal to 10% of culture volume restored amino acid content to that of normal DMEM. An equal volume of solvent (water) was spiked into control plates. Serum starvation, as in Figure 5A, was pH 7.4 or 6.3 media without serum and was rescued by addition of undialyzed (full) FBS to restore 10% serum levels. Rescues were confirmed to not appreciably alter media pH. Duration of starvations and rescues as indicated in legends. All starvation medias were used in atmospheric CO<sub>2</sub>.

Viable previously activated OTI CD8<sup>+</sup> T cells were obtained through Ficoll (GE healthcare) gradient of splenocytes (derived as described above). Cells were washed

two times in PBS before starvation of amino acids and growth factors by incubation in PBS (pH 7.4) for 1 hour. Cells then either continued in starvation for 30 minutes or were rescued from starvation into RPMI media of the indicated pH (formulated as described above) for 60 minutes.

#### RNA collection

Media was aspirated from cells growing in 35 mm dishes. 1 mL of TRIzol Reagent (Invitrogen) was added to plates. A cell scraper was then used to collect cells and lysate which was frozen at -80 °C until RNA isolation following the manufacturer's instructions with substitution of 1-Bromo-3-chloropropane for chloroform. RNA used for qPCR in Figures S1K or S7F was instead extracted with the RNeasy Plus Mini Kit (Qiagen) following cell trypsinization (S1K) or direct application of the kit's lysis buffer to aspirated 12-well culture plates and scraping (S7F).

#### Quantitative Real-Time PCR

Isolated RNA was reverse transcribed to complementary DNA (cDNA) using TaqMan Reverse Transcription Reagents (Invitrogen) using the Oligo d(T) method. cDNA was then used as template for quantitative real-time PCR with specific human primers using Power SYBR Green or TaqMan Universal PCR master mixes (Thermo Fisher) using a ViiA 7 real-time PCR system or StepOnePlus Real-Time PCR System (Applied Biosystems). Target expression was normalized to *B2M* and relative expression was calculated using the delta-delta CT method. For 52-hour qPCR timecourses (Figures 2B-D, S2A, S2C, S2F, S3A (right)), data are normalized to the respective 4-hour control (vehicle, normoxia, or pH 7.4) time point.

### siRNA knockdown

Effective dicer-substrate short interfering RNAs (DsiRNAs, referred to as “siRNA”) in Trifecta kits (IDT) were identified through qPCR-based assessment of knockdown of target transcript in U2OS cells prior to use. 185-375,000 or 50,000 cells were seeded in 35 mm dishes or 24-well dishes, respectively, and allowed to expand in standard DMEM in 5% CO<sub>2</sub> incubators. The following day, cells were transfected with DsiRNA at the concentrations indicated in legends using Lipofectamine RNAiMAX (Invitrogen) 26-31 hours prior to cell synchronization and further treatment, except Figure 7B where time points are as detailed in figure and legend. DsiRNA included those against *HIF1A*, *EPAS1*, *EIF4EBP1* (DsiRNA oligo #1 used in Lumicycle experiment, #2 used in western), *EIF4EBP2*, *SESN1*, *SESN2*, *SESN3*, *KIF5B*, *TSC2*, and *TXNIP*. Equimolar non-targeting DsiRNA was used as a control. Concentrations of DsiRNA in Fig. 1E are 20 nM each condition (10 nM when two siRNA). Concentrations elsewhere as indicated in figure legends. DsiRNA sequences in Appendix.

For validation of the anti-RHEB antibody used for immunofluorescence (see below), 200K U2OS *Arntl::dLUC* cells were seeded in each well of a 6-well plate. The following day, cells were transfected with 20 nM total siRNA per condition using RNAiMAX. More precisely, the “siCtl” condition was 20 nM non-targeting DsiRNA, “siRHEB” was 10 nM DsiRNA targeting *RHEB* and 10 nM non-targeting DsiRNA, “siRHEBL1” was 3.33 nM each of three different DsiRNA against *RHEBL1* and 10 nM non-targeting DsiRNA, and “siRHEB + siRHEBL1” was 10 nM DsiRNA targeting *RHEB* and 3.33 nM of the three siRNA against *RHEBL1*. After 26 hours, cells were trypsinized and reseeded in 12-well dishes with or without glass coverslips for immunofluorescence (described below) or

RNA and protein harvests, respectively. Cells were fixed or harvested 56 hours after siRNA treatment. DsiRNA sequences in Appendix.

#### RNA-sequencing and data processing

RNA integrity was verified by bioanalyzer (Agilent Technologies) (RIN 8.7-10.0, median = 9.7). Libraries were prepared from total RNA using the Illumina TruSeq Stranded mRNA Library Preparation kit (Illumina). Pooled libraries were sequenced as single 100 base pair reads on the HiSeq 2500 in rapid mode using V4 chemistry at the University of Pennsylvania Next Generation Sequencing Core. The RNA-seq raw reads (FASTQ files) were aligned to the reference genome hg38 (<https://genome.ucsc.edu/cgi-bin/hgGateway?db=hg38>) using Spliced Transcripts Alignment to a Reference (STAR) aligner (<https://github.com/alexdobin/STAR>) (Dobin et al., 2013). The GENCODE v22 (<https://www.gencodegenes.org/releases/22.html>) annotation was used as the guiding transcriptome annotation during STAR alignment. The aligned RNA-Seq reads (BAM files) were further processed through Cufflinks (<http://cole-trapnell-lab.github.io/cufflinks/>) (Trapnell et al., 2013) to assemble and quantify transcripts, using GENCODE v22 as the reference transcriptome annotation. The fragments per kilobase of transcript per million mapped reads (FPKM) calculation was used to normalize read count by dividing it by the gene length and the total number of reads mapped to genes. Analysis was limited to protein-coding genes (as defined by GENCODE v22 annotation) with mean FPKM expression over all time points and pH conditions greater than 2 (10,794 genes).

#### Global gene expression analyses

Circadian rhythmicity of the 10,794 protein-coding transcripts detected by RNA-sequencing was assessed by ARSER algorithm (Yang and Su, 2010). ARSER detrends

data and then detects rhythmic signals with a period between 20 and 28 hours through a combination of autoregressive spectral analysis (alternative to the classical fast Fourier transformation) and harmonic regression (sinusoidal fits) and then reports relevant parameters such as period, phase, and amplitude along with significance statistics. ARSER was run through the MetaCycle package implemented in R (Wu et al., 2016). ARSER has been shown to frequently perform better than other popular circadian gene identification algorithms when analyzing data collected over two days with 4-hour resolution (Wu et al., 2016; Yang and Su, 2010). Cutoffs of  $p < 0.05$  and Benjamini and Hochberg false-discovery rate (FDR)  $< 0.20$  were used to identify circadian transcripts. The Ensembl IDs of these genes with statistically significant circadian expression in pH 7.4 and pH 6.3 were then submitted to ToppFun (Chen et al., 2009) with default settings to determine significantly enriched Pathway ontologies ( $p < 0.05$ , Benjamini and Yekutieli (B&Y) FDR ( $q$ )  $< 0.05$ ). All significant Pathway ontologies and associated p-values are presented in corresponding figures.

Transcripts highly induced or suppressed in acid were defined as those for which the  $\log_2$  of the ratio of the mean expression over all 13 time points (4h-52h) in pH 6.3 to pH 7.4 ( $\log_2(\bar{X}_{pH6.3} / \bar{X}_{pH7.4})$ ) was greater than 1 or less than -1, respectively. The Ensembl IDs for these genes were then submitted to ToppFun (Chen et al., 2009) to determine significantly enriched GO:Biological Process ontologies ( $p < 0.05$ , Benjamini and Hochberg (B&H) FDR ( $q$ )  $< 0.05$ ). All significant Biologic Process ontologies and associated p-values are presented in figures for acid-suppressed genes. For induced genes, the top 10 are presented.

All heatmaps and to-scale Venn Diagrams were generated with ggplot2 and VennDiagram packages implemented in R Studio. For heatmaps in 3A and S3B,

expression in each pH condition was normalized separately for each gene, with each gene's maximum and minimum expression values across all 13 time points (52-hours) in that pH condition set to 1 (navy) and 0 (white), respectively, with linear scaling over the intervening expression range (i.e. 0.5 is midway between minimum and maximum expression). For heatmaps in 3F and 3G, the maximum and minimum expression values for each gene across all time points and pH conditions (i.e. regardless of pH) were set to 1 (navy) and 0 (white), respectively, with linear scaling over the intervening expression range (i.e. 0.5 is midway between minimum and maximum expression). Heatmaps in 3A and S3B are ranked by phase of transcript oscillation in pH 7.4 or 6.3, respectively. Heatmaps in 3F and 3G are ranked from top by most highly induced or suppressed gene, respectively.

#### Polysome profiling

2 million or 1 million U2OS *Arntl::dLUC* cells were seeded in normal DMEM and cultured in standard 5% CO<sub>2</sub> 37 °C humidified tissue culture incubators. The following day, media of the higher density plates was aspirated and replaced with media pH 6.3 (formulated as above). The plates seeded at 1 million cells per plate were changed to pH 7.4 media in parallel. Plates were moved to humidified 37 °C incubators with atmospheric CO<sub>2</sub> and allowed to grow for 37 hours prior to harvesting for polysome profiling as described (Brady et al., 2017; Johannes and Sarnow, 1998) using RNase-free conditions wherever possible.

One day prior to harvest, 10-50% sucrose gradients were poured. Briefly, a 75% sucrose (Fisher Scientific) solution was diluted in RNase free water to prepare 10%, 20%, 30%, 40%, and 50% sucrose solutions each with final concentrations of 0.3 M NaCl

(Invitrogen), 15 mM Tris-Cl pH 7.5 (Invitrogen), 15 mM MgCl<sub>2</sub> (Invitrogen), 1 mg/mL heparin (Sigma), and 0.1 mg/mL cycloheximide (prepared fresh from powder (Sigma C1988)). 2.1 mL of the 10% sucrose solution was added to the bottom of round bottom tubes. A glass pipette was used to layer the same volume of the 20% sucrose solution underneath the 10% layer with minimal disturbance of the layer interface, followed similarly by the 30% solution under the 20%, and so forth to form a layered gradient increasing in density with depth. Gradients were sealed with parafilm and stored at 4 °C overnight.

After 37 hours pH exposure, four plates each pH condition were harvested pairwise. (Counting of plates seeded in parallel indicated an expected thus total yield of 23 million cells for pH 7.4 and 25 million for pH 6.3.) Briefly, freshly prepared 10 mg/mL cycloheximide was spiked 1:100 (0.1 mg/mL final) into one pH 7.4 and one pH 6.3 plate. Plates were gently swirled and returned to 37°C for 3 min. Media was then aspirated and replaced with ice-cold PBS containing 0.1 mg/mL cycloheximide. Plates were placed on ice and washed once more with cold cycloheximide-containing PBS. Cells were lysed on plates by scraping in 300-400 uL cold polysome extraction buffer (PEB: 0.3 M NaCl, 15 mM MgCl<sub>2</sub>, 15 mM Tris-HCl pH 7.5, 1% Triton X-100 (Sigma), 0.1 mg/mL cycloheximide (added fresh), and 1 mg/mL heparin) and transferring lysate to tubes on ice. The next pair of plates was cycloheximide treated and washed in analogous fashion prior to scraping in the corresponding lysate of the first set of plates. Harvest continued for the remaining two pairs of plates similarly transferring lysate from plate to plate and thus pooling lysate from all 4 plates. Lysates were then brought up to 1000 uL with PEB. Lysates were left on ice for > 10 minutes following harvest of final plates and then spun down at 10K RPM at 4 °C.

Each cleared lysate was layered onto one gradient. Gradients were pre-balanced for weight as necessary with PEB and centrifuged for 3 hours and 10 min at 35K RPM in a SW41Ti rotor at 4 °C. 1 mL fractions were collected in Eppendorf tubes by pumping push solution (67.5% sucrose with bromophenol blue) into the bottom of the gradient and collecting from the top with a fraction collection system with concurrent monitoring of the absorbance of the passing gradient at 254 nm (OD 254). Fractions were transferred to round bottom tubes using 1 mL of nuclease free water as rinse. After addition of 3 mL of 8 M guanidine HCl (Thermo Scientific), samples were vortexed for 1-2 minutes. One volume (5 mL) of 100% ethanol was added and samples were vortexed again before incubating at -20 °C until further processing several days later.

Samples were centrifuged for 45 minutes at 4 °C in the outer tier of a SM24 rotor in the Thermo RC6+ centrifuge at 10K RPM (12.4 RCF). Supernatants were carefully removed. After addition of 4 mL of ice cold 75% ethanol, samples were vortexed and spun again for 30 minutes. Supernatants were carefully removed and pellets were allowed to dry for 10 minutes before resuspension in 400 uL of Tris-EDTA (TE) buffer, pH 7.4 (Sigma). RNA was precipitated by addition of 3 M sodium acetate, pH 5.2 (Thermo Scientific) to a final concentration of 0.3 M followed by addition of 2.5 volumes of 100% ethanol and incubation overnight at -20 °C.

Samples were then centrifuged for 20 min at room temperature at 13K RCF and supernatants were carefully removed. Pellets were washed with 400 uL of ice cold 75% ethanol, vortexed, and centrifuged again for 20 min at room temperature. After removing supernatant, pellets were dried for 10 minutes and resuspended in 50 uL of 0.1x TE buffer. RNA yield was then assessed by nanodrop. Additionally, RNA was subjected to Tape Station analysis to corroborate fraction identity inferred from OD 254 profiles.

Volumes of sample per each tape station run were variable, chosen based on nanodrop results to load Tape Station chips within their target quantitative range. The intensity of each “gel-like image” from each sample’s Tape Station run was scaled relative to loading volume to create *in-silico* an approximated multilane gel-like image analogous to a tradition RNA gel. The OD254 reading, 28S/18S ratio, and appearance of 28S and 18S bands were used to identify likely fraction compositions with consultation of published methods (Brady et al., 2017; Fromm-Dornieden et al., 2012; Johannes and Sarnow, 1998).

30 pg of b-galactosidase mRNA (CleanCap™ β-gal mRNA, TriLink) was spiked into 27 uL of each extracted RNA fraction. Lithium chloride (LiCl) (Invitrogen) was added to a final concentration of 2.5 M. Samples were vortexed and placed in -20 °C for 30 min. Samples were then spun for 30 minutes at 4 °C at 13K RCF. Supernatant was aspirated and discarded. Pellet was washed in 75% ethanol and spun again for 15 minutes at 13K RCF at room temperature. Supernatant was again carefully removed and discarded. LiCl precipitation was then performed once more again at -20 °C for 30 min with centrifugation at 16K RCF. After resuspension of pellets in 75% ethanol, samples were stored at -20 °C overnight. After carefully removing supernatants, pellets were dried, and resuspended in 100 uL water with the aid of heating to 55-60 °C for 10-15 minutes. RNA was then purified over a RNeasy column (Qiagen) using the manufacturer’s RNA cleanup protocol with elution in equal 50 uL volumes of water. Concentrations were then measured by nanodrop. Displayed nanodrop yields encompass (i.e. are corrected for) known sample usage (e.g. Tape Station analysis, nanodrop) and banking en route to final elution to straightforwardly reflect starting cell numbers.

Isolated RNA was reverse transcribed to complementary DNA (cDNA) using the iScript Reverse Transcription Supermix, a blend of oligo-dT and random hexamer primers (Bio-Rad). cDNA was then used as template for quantitative real-time PCR with specific validated primers as indicated (sequences in Appendix). Target expression was normalized to  $\beta$ -galactosidase spike-in using the following primers:

$\beta$ -galactosidase #4	Fwd:	Rev:
	CCACCAGCGAGATGGACTTC	CTTGTCGCCGATCCACATCT

Relative expression was calculated using the delta-delta CT method. Data are presented with normalization to respective pH 7.4 fraction #5 value. Presented qPCR results are limited to fractions 4-12 where efficient recovery and amplification of spike-in was achieved.

### Immunofluorescence

10,000-20,000 U2OS *Arntl*::dLUC cells were plated on 18mm glass coverslips in 12-well dishes and allowed to adhere and grow in normal DMEM in 5% CO<sub>2</sub> for 1-2 days. Media was then changed to experimental conditions (pH 7.4, pH 6.3, starvations medias, etc.) as described above and as indicated in figure legends. Where indicated, starvation was followed by “rescue” of pH/starvation by change of media (for pH conditions) or spike in of amino acids (as described above). Cells were then rinsed with PBS once and fixed for 15 min with fresh 4% paraformaldehyde in PBS at room temperature. Cells were then rinsed twice with PBS (1x quick, 1 x 5 min) before permeabilizing for 5 min in 0.05% Triton X-100 in PBS. Coverslips were then washed two times for 5 min each in PBS and then blocked for 30 min in filtered 5% goat serum (Sigma) in PBS. Coverslips were then incubated in primary antibody in blocking buffer for 2 hours at room temperature (rabbit

anti-mTOR, Cell Signaling, 1:40-1:320; mouse anti-LAMP2, Abcam 25631, 1:100) or overnight at 4 °C in a humidified chamber (rabbit anti-mTOR, 1:200; rabbit anti-LAMP1, Cell Signaling, 1:200; mouse anti-RHEB, Abnova, 1:1000), washed three times in PBS, and then incubated for 1 hour in secondary antibodies (goat anti-rabbit Alexa Fluor 488 and goat anti-mouse Alexa Fluor 594 (1:400-1:1000) or 555 (1:500-1:1000)) in blocking buffer at room temperature. Alexa Fluor 488-conjugated rabbit anti- $\alpha$ -tubulin (Cell Signaling, 1:100-1:200) was co-incubated with goat anti-mouse Alexa Fluor 594 when used. When combined with goat anti-mouse Alexa Fluor 555, tubulin staining was performed separately after this secondary antibody. Filamentous actin was stained with 330 nM Alexa Fluor 488 phalloidin (Cell Signaling) for 15 min in blocking buffer following other secondaries. When performed, a 140 - 860 nM solution of DAPI in PBS was applied to coverslips for 1-10 min after aspirating secondaries.

For four-color staining, coverslips seeded two days prior with 10,000 U2OS *Arntl::dLUC* cells or U2OS *Arntl::dLUC RHEB<sup>N153T</sup>* cells were treated and processed as above with overnight incubation with rabbit anti-mTOR and mouse anti-RHEB. After washing, coverslips were incubated with goat anti-rabbit Alexa Fluor 647 (Invitrogen, A32733, 1:1000) and goat anti-mouse Alexa Fluor 555 secondaries as above. Coverslips were then blocked for 30 minutes in filtered 5% rabbit serum (Sigma) in PBS, incubated overnight with sheep Alexa Fluor 488-conjugated anti-LAMP1 (1:200, R&D Systems) in blocking buffer (5% rabbit serum in PBS) at 4°C, and stained for DAPI.

After washing three times for 5 min each in PBS, coverslips were rinsed once in distilled water and mounted onto glass slides with Fluoromount-G (SouthernBiotech) and later sealed with covergrip coverslip sealant (Biotium). All immunofluorescence reflects unsynchronized cells (no dexamethasone). No primary, no secondary, and single-color

controls were performed to validate specificity of antibodies and confirm negligible bleed through across antibody-channel combinations.

For validation of the anti-RHEB antibody used for immunofluorescence, U2OS *Arntl::dLUC* cells were treated with siRNA as described above and 26 hours later reseeded onto glass coverslips in 12-well dishes at a density of 100K cells per well. The following day (56 hours after siRNA treatment), cells were fixed and processed as described above with overnight incubation with anti-RHEB (1:1000) and anti-LAMP1 (1:200) antibodies followed by goat anti-mouse Alexa Fluor 488 and goat anti-rabbit Alexa Fluor 594 (Invitrogen, 1:1000 each).

Following starvation and rescue as described above and in figure legends, previously activated OTI CD8<sup>+</sup> T were processed for immunofluorescence. Cells were fixed by resuspension in methanol free 4% PFA (Invitrogen) for 10 minutes at 37 °C, and then washed 3 times with PBS and stored in PBS at 4 °C. A hydrophobic barrier (PAP pen, 71310 Electron Microscopy Sciences) was used to demarcate a region on glass coverslips that was then coated with 1 mg/mL poly-D-lysine (Sigma) for 1 hour at room temperature before washing three times with water and once with PBS. Fixed cells resuspended in PBS were then allowed to settle onto the poly-D-lysine coating overnight humidified at 4° C. Coverslips were then washed twice with PBS before permeabilizing with 0.1% Triton X-100 in PBS for 15 minutes at room temperature. After washing four times with PBS, cells were blocked with 5% goat serum in PBS with 0.05% Tween-20 (PBST) for 30 minutes. Coverslips were then incubated with primary antibody (anti-mTOR 1:200; anti-LAMP2, Abcam 13524, 1:200) overnight humidified at 4 °C. Coverslips were then washed five times with PBST and incubated with Alexa Fluor goat secondary antibodies (anti-rabbit 488 and anti-rat 555, 1:500) for 90 minutes at room

temperature. Following five washes with PBST, cells were stained with DAPI as above. Coverslips were then washed three times with PBS and mounted in Fluoromount-G and sealed as above. See Appendix for product numbers of reagents.

### Live-cell imaging

#### *Transient transfection of LAMP1 fusion proteins*

200,000-215,000 U2OS *Arntl::dLUC* cells were plated in plastic or glass-bottom 35mm culture dishes in normal DMEM in 5% CO<sub>2</sub>. The following day, cells were transfected with 0.5-1.0 ug of LAMP1-FLAG(x2)-mRFP (gift from David Sabatini, Addgene plasmid #34611) or LAMP1-mGFP (gift from Esteban Dell'Angelica, Addgene plasmid #34831. mGFP is a non-dimerizing GFP variant that reduces aberrant aggregation of overexpressed protein). 48-96 hours later, media was exchanged for media of pH 7.4 or 6.3 and plates were moved to atmospheric CO<sub>2</sub>. After 2.5-4 hours incubation (as indicated in legends), cells were imaged as described below. For the timecourses of ciliobrevin D and nocodazole treatments (Figures 6N, S6I, S6L, S6M), the day following transfection cells were instead trypsinized and reseeded at lower density (75,000 cells/plate). Two days later, cells were treated with 60 uM ciliobrevin D or 2 uM nocodazole and imaged at intervals as indicated in figures.

#### *LysoTracker and TubulinTracker*

30 minutes prior to imaging, media was exchanged for fresh media with 50 nM LysoTracker Deep Red (Invitrogen) and 500 nM TubulinTracker Green (Oregon Green 488 Taxol bis-acetate, Invitrogen). Cells were then washed three times with media and then imaged in media. For cells treated with vehicle or inhibitor (nocodazole, ciliobrevin D), media both during the 30 min staining and during imaging contained vehicle or drug.

When only LysoTracker was used, media was changed after staining but washes were omitted.

#### Microscopy and image processing

Images of immunofluorescence staining of U2OS cells were acquired using Dapi, GFP, and DsRed filter sets as needed on an upright Nikon Eclipse Ni microscope equipped with 20x/0.5 PlanFluor, 40x/0.75 PlanFluor, and 60x/0.95 Plan Apo  $\lambda$  objectives and 12-bit QImaging QIClick CCD and DS-Fi2 Nikon cameras controlled by Nikon NIS-Elements Basic Research software or using Dapi, GFP, dsRed, mCherry/TxRed, and Cy5 filter sets as needed on a Nikon Eclipse 80i microscope using a 60x objective with a 0.63x c-mount and a QImaging camera controlled by Image-Pro Plus v 7.0 software. Live cell images were acquired with GFP, TxRed, Cy5 and phase contrast filter sets as needed on an Olympus IX81 inverted fluorescence microscope quipped with 10x, 20x, and 40x objectives (UPLFLN10X2PH, LUCPLFLN20XPH, LUCPLFLN40XPH) and a 12-bit CCD camera (Sensicam QE, PCO) controlled by SlideBook 6 software. All exposure times and other hardware settings were identical for all images captured in the same channel within an experiment. This includes Figure 7F where acquisition settings were identical for imaging of RHEB in both wild-type (U2OS *Arntl::dLUC*) and RHEB<sup>N153T</sup>-expressing cells. Scale bars are shown. Where not otherwise indicated, a scale bar shown in one image of a multi-image panel is applicable to all images.

Confocal microscopy images of immunofluorescence staining of CD8<sup>+</sup> T cells were acquired as 2048 x 2048 pixel images on a Zeiss LSM 880 using excitation wavelengths of 405, 488, and 561 nm and a Plan-apochromat 63x 1.40 0.1 DIC M27 objective with zoom factor 1.0 controlled by ZEN v2.3 software. Scale bars are shown.

Fiji software (Schindelin et al., 2012) was used for background subtraction (rolling ball method or subtraction of a constant as described below) and brightness (contrast) adjustment if needed. For immunofluorescence and LysoTracker and TubulinTracker live-cell imaging (i.e. methods labeling endogenous proteins and compartments), all processing (background subtraction, brightness adjustment) was uniform across all acquired images within that channel in that experiment. The only exception was DAPI staining which was occasionally independently contrasted for display purposes only (but quantified using raw or uniformly processed (background subtracted) images). For live-cell imaging of LAMP1-GFP and LAMP1-mRFP, images in the GFP and RFP channels, respectively, were contrasted individually owing to variability in transfection efficiency across the population of cells. For all microscopy, representative images of random fields acquired from at least three biological replicates are shown.

Microscopy for *in vivo* studies discussed below in description of that work.

#### Image quantification

mTOR enrichment on lysosomes as a function of amino acids and pH was quantified from 40x widefield images of U2OS cells coimmunostained for mTOR and LAMP2 using a quantification method modified from that previously described (Wolfson et al., 2017). mTOR and LAMP2 channels were background corrected in Fiji (Schindelin et al., 2012) by subtracting a constant equal to the mean of three regions of interest (ROIs) drawn within the image background of each channel. The borders of each cell or cell cluster were drawn by applying the Analyze Particle function to the thresholded mTOR channel image (settings: particles > 200 pixels<sup>2</sup>, exclude holes) and supplementing this with manual additions and subtractions as needed to define the “cell” ROI of each field. The

LAMP2 channel images were then thresholded (same threshold across all images) to define the “lysosome” ROI within each field. The “lysosome” ROI was subtracted from the “cell” ROI of a field to define the “cytoplasm” ROI of each field. LAMP2 and mTOR mean fluorescence intensity (MFI) were then measured in each compartment. To calculate the relative enrichment of mTOR in the lysosomal compartment over the cytoplasm in each field, the MFI of mTOR in the cytoplasm ROI was subtracted from the MFI of mTOR in the lysosome ROI. The lysosomal LAMP2 MFI was similarly corrected for the background cytoplasmic MFI of that channel. The mTOR difference was then divided by the LAMP2 difference to account for varying amounts and densities of lysosomes across fields. Hence, the reported mTOR lysosomal enrichment score for each field (image) was  $(L - C)_{\text{mTOR}} / (L - C)_{\text{LAMP2}}$  where L and C are the MFI of the respective channels in the lysosomal and cytoplasmic ROIs, respectively, as previously described (Wolfson et al., 2017). Prior to quantification, pixels containing rare obvious small processing artifacts were excluded across all channels when observed although post hoc analysis revealed near identical results had this step been skipped. Replicates and statistics as described in legends.

mTOR lysosomal enrichment in CD8<sup>+</sup> T cells was similarly quantified from 63x magnification confocal images. Background correction was omitted as background was confirmed negligible. Cells were outlined to define the “cell” ROI by using the analyze particle function on uniformly thresholded mTOR channel images (settings: particles >5  $\mu\text{m}^2$ , include holes). Because the nucleus takes up a significant portion of the volume in T cells, the “nucleus” ROI was defined by applying the analyze particle function to thresholded DAPI channel images. The union of “nucleus” ROI and “lysosome” ROI (determined as above) was then subtracted from the “cell” ROI to determine the

“cytoplasm” ROI for each field. The mTOR lysosomal enrichment score for each field was then calculated as  $(L - C)_{\text{mTOR}} / (L - C)_{\text{LAMP2}}$  as above, with replicates and statistics as described in legends.

Radial distributions of LAMP2, tubulin, and DAPI intensity were quantified in Fiji (Schindelin et al., 2012) from 3-channel background corrected (rolling ball method or subtraction of a constant as above) 40x images of immunostained U2OS cells. Radial distributions of mTOR, LAMP1, RHEB, and DAPI were similarly quantified from 4-channel 60x (+0.63x c-mount) images. For each cell analyzed, the outline of the cell was manually delineated and all pixels outside this area were cleared in all channels to define the “cell” ROI. The nucleus was then defined with the aid of the Analyze Particle function (default settings) applied to the thresholded DAPI channel. This “nucleus” ROI was then subtracted from the “cell” ROI to define the “cytoplasm” ROI. The tubulin and LAMP2 intensities as a function of radial distance from the nucleus center were calculated within the “cytoplasm” ROI with the Radial Profile plugin for a circle centered on the nucleus with a 500-pixel (80.5  $\mu\text{m}$  (40x) or 85  $\mu\text{m}$  (60x + 0.63x c-mount)) radius (i.e. a circle encompassing the entire cell area). This plugin returned the intensities as a function of the radius (r) in 1.33-pixel (0.215 or 0.226  $\mu\text{m}$ ) steps ( $r = 1.33, 2.66, 3.99, \dots 500$  pixels). Here, intensity is the integrated fluorescence around a circumference (defined by the radius) divided by that circumference. As these output intensities are not corrected for cell shape, the output intensities were multiplied by  $\pi 2r$  (the circumference, giving integrated fluorescence) and divided by the arc length through the “cytoplasm ROI” at that radius (calculated by running the plugin on a new image created with every background pixel 0 and every pixel within the “cytoplasm” ROI set to 1). DAPI radial distribution was similarly calculated over the “cell” ROI. For LAMP2, tubulin, and DAPI 3-

channel images, 15 cells were analyzed for each pH condition and the mean profile was calculated. For display purposes, calculated mean intensities were normalized to the maximum mean value within that channel (irrespective of pH). Unadjusted t-tests (i.e. no multiple testing correction) were performed at each r comparing the intensity of a given channel at each pH. For each r for which  $p < 0.05$ , an asterisk appears above the graph. For mTOR, LAMP1, RHEB, and DAPI 4-channel images, 10 cells were analyzed for each pH condition for U2OS *Arntl::dLUC* cells and 13 cells for each pH condition for U2OS *Arntl::dLUC RHEB<sup>N153T</sup>* cells. Mean profiles were calculated and normalized to the maximum mean value within that channel in U2OS *Arntl::dLUC* pH 7.4 cells.

Intensity profiles of RHEB, mTOR, LAMP1, and DAPI along a manually drawn reference line were obtained using the Plot Profile command in Fiji.

#### Flow cytometry

##### *T cell mTOR activity*

Primary splenocytes were derived as above and resuspended in RPMI media of the corresponding pH as indicated in figure legends and formulated as described above. Splenocytes from mice with TSC2  $-/-$  and TSC2  $+/+$  T cells were stimulated with 3  $\mu\text{g}/\text{mL}$  cross-linked anti-CD3 and 2  $\mu\text{g}/\text{mL}$  anti-CD28 (in-house hybridomas). After 1 hour, splenocytes were fixed with 2% PFA for 10 minutes at 37 °C then washed two times with PBS. Cells were then permeabilized with ice cold 90% methanol for 20 minutes at -20 °C, washed three times with 1% FBS/PBS (staining solution), and stained with brilliant violet 786-conjugated rat anti-CD4 (BD Bioscience, 1:500), brilliant violet 650-conjugated rat anti-CD8 (BD Bioscience, 1:500), and anti-phospho serine 240/244 S6 (1:1000) in staining solution for 45 minutes at room temperature. Cells were then washed two times

with staining solution before staining with goat anti-rabbit IgG Alexa Fluor 647 (Invitrogen A21244, 1:500) for 30 minutes at room temperature. Cells were then washed two times before analysis with a BD Celesta and FlowJo software. Gates were set appropriately with the aid of unstimulated and secondary-alone controls. See Appendix for product numbers of reagents.

### Cytomegalovirus infection

Human cytomegalovirus (HCMV) preparation and infection proceeded as previously described (Clippinger et al., 2011). The virus used was a derivative of the Towne strain of HCMV in which some nonessential genes have been replaced with GFP expressed by the SV40 promoter (Clippinger et al., 2011). 150,000 U2OS *Arntl::dLUC* cells were seeded in 35 mm dishes. Three days later, one plate was trypsinized to determine the number of cells. An aliquot of previously titered human cytomegalovirus was thawed, sonicated on low power, and added to standard culture media (DMEM, 5% CO<sub>2</sub>) that was then applied to cells at a multiplicity of infection of 3. Media without virus was similarly used to refresh plates of “mock infected” cells. After two hours, media was aspirated and replaced with fresh DMEM. This was considered time zero of infection. At 19 hours post infection (hpi), media of two virus- and two mock-infected plates was exchanged for low buffer media containing vehicle or 500 uM DMOG and moved to atmospheric CO<sub>2</sub>. At 26 hpi, media of an additional two virus- and two mock-infected plates was exchanged for media of pH 7.4 or pH 6.3 and moved to atmospheric conditions. Protein was then harvested from all 8 plates one hour later (at 27 hpi). These media exchanges were repeated once more for an additional time point, with vehicle/DMOG treatment beginning at 47 hpi, pH 7.4/6.3 at 58 hpi, and protein harvest at 59 hours. Consequently, the first immunoblot time point (27 hpi) reflects 8 hours of

vehicle/DMOG or 1 hour of neutral/acidic pH treatment, while the second time point (59 hpi) reflects 12 hours of vehicle/DMOG or 1 hour of neutral/acidic pH treatment. To confirm infection, two immediate-early viral proteins, immediate-early protein 72 (IE72) and immediate-early protein 86 (IE87), were probed with an antibody recognizing major immediate-early viral proteins containing viral exon 2 and 3 regions (Clippinger et al., 2011).

#### Bicarbonate treatment of tumors

Tumor tissue specimens were obtained from two previously conducted studies (Estrella et al., 2013; Ibrahim-Hashim et al., 2017) in which the drinking water of mice bearing xenograft tumors was either supplemented with bicarbonate to raise intratumoral pH or not supplemented ("tap" water). These tissues were then queried for the current study for the impact of bicarbonate therapy on tumor mTORC1 signaling. In detail:

#### *Cell Culture*

The human breast cancer cell lines MCF7 and MDA-MB-231 and the human colon cancer cell line HCT116 were acquired from the American Type Culture Collection (ATCC, Manassas, VA). MCF7 and MDA-MB-231 cell lines were maintained in RPMI medium 1640 (Gibco) supplemented with 10% FBS (Hyclone) and 1x penicillin/streptomycin. HCT116 cells were maintained in DMEM/F12 (Gibco) supplemented with 10% newborn calf serum and 1x penicillin/streptomycin. Medias were further supplemented with 0.75 mg/mL of G418 to maintain stable polyclonal expression of previously transfected pIRES2-EGFP (MCF7), pDsRed2-N1 (MDA-MB-231), and pcDNA3-GFP (HCT116) for *in vivo* tumor border demarcation. During *in vitro* HCT116 experiments, G418 selection was not maintained. All cells were maintained in standard

humidified tissue culture incubators at 37 °C with 5% CO<sub>2</sub> and manipulated under sterile conditions in a tissue culture hood. All three cell lines were authenticated by short tandem repeat analysis and confirmed to be free of mycoplasma.

#### *Tumor development and bicarbonate treatment*

All animals were maintained in accordance with the guidelines of the Institutional Animal Care and Use Committee (IACUC) at H. Lee Moffitt Cancer Center. Eight- to ten-week-old male and female (randomized) severe combined immunodeficient (SCID) mice (Charles River) were used to host HCT116 tumors. Eight- to ten-week-old female nu/nu mice (Envigo) were used to host MDA-MB-231 and MCF7 tumors.

HCT116 cells were implanted into a dorsal window chamber using the tumor droplet method as described previously (Estrella et al., 2013). Briefly, a dorsal window chamber was implanted into a host mouse. The following day, HCT116 cells were suspended in 0.8 mg/ml of type I collagen (BD Bioscience) and 1x DMEM at a final concentration of  $2.5 \times 10^6$  cells/mL. 15  $\mu$ L of the tumor suspension was then polymerized in the center of a well of a 48-well non-tissue culture-treated multiwall plate. After polymerizing for 20-30 min at 37 °C, the droplet was surrounded by a layer of 1.25 mg/mL type I collagen, which encouraged the tumor to maintain a circular shape with well-defined borders. After polymerizing for 20-30 min at 37°C, the construct was incubated with 200  $\mu$ L of DMEM with 10% FBS at 37°C. After 2 days of culture, the constructs were aseptically inoculated into the window chamber. Six days prior to the inoculation of tumor constructs into the dorsal window chamber, mice were randomly assigned to receive 200 mM sodium bicarbonate (n=4) (Fisher Scientific) or tap water (n=4) provided *ad libitum* for the

duration of the experiment. Treatment continued for up to three weeks with tumors harvested when they reached the capacity of the window chamber.

For MDA-MB-231 and MCF7 tumor formation, 10 million cells were injected into cleared mammary fat pads as described previously (Ibrahim-Hashim et al., 2017). One week prior to cell injection, an estrogen pellet (0.72 mg slow release, Innovative Research of America) was implanted to allow growth of ER-positive MCF7 tumors. Three days after tumor injection the mice were randomly assigned to drinking water supplemented with 400 mM sodium bicarbonate or tap water (n=5 each arm for MCF7; n=4 each arm for MDA-MB-231) provided *ad libitum* for the duration of the experiment. Five weeks later, tumors were harvested.

#### *Immunohistochemistry (IHC)*

At endpoints of the study, tumors were harvested, fixed in 10% neutral buffered formalin (Thermo Fisher Scientific), processed, embedded in paraffin, and sliced to 4-5  $\mu$ m sections. Slides were stained with hematoxylin and eosin (H&E) stain.

Immunohistochemistry for phospho-S6 was performed using the Leica BOND RX stainer as per the manufacturer's protocol with ancillary reagents. Briefly, slides were deparaffinized with Dewax solution and antigens heat-retrieved in the ER2 buffer. Rabbit primary antibody that reacts to pS6 (Ser240/Ser244, ThermoFisher Scientific) was used at a 1:200 concentration for 15 min. The Bond Polymer Refine Red Detection system with alkaline phosphatase-linked polymers and red chromagen (Fast Red) was used to detect primary antibody with subsequent hematoxylin counterstain. Slides were then dehydrated and coverslipped as per normal laboratory protocol. Histology slides were

scanned using the Aperio™ ScanScope XT (Leica) with a 20x/0.8NA objective lens (200x) at a rate of 2 minutes per slide via Basler tri-linear-array.

Carbonic anhydrase IX immunohistochemistry was performed using the a Ventana Discovery XT automated system (Ventana) as per the manufacturer's protocol with proprietary reagents. Briefly, slides were deparaffinized on the automated system with EZ Prep solution (Ventana). Heat-induced antigen retrieval method was carried out in RiboCC (Ventana). Rabbit primary antibody that reacts to CAIX (Abcam) was used at a 1:250 concentration in Dako antibody diluent (Agilent) and incubated for 32 min. The Discovery OmniMap Anti-Rabbit HRP Secondary Antibody (Ventana) was used for 20 min. The detection system used was the Ventana Discovery ChromoMap DAB kit (Ventana). Slides were then counterstained, coverslipped, and scanned as above.

#### *Image analysis*

An Aperio Positive Pixel Count® v9.0 algorithm with the following thresholds: [Hue Value = 0.1; Hue Width = 0.5; Color Saturation Threshold = 0.04; IWP(High) = 220; Iwp(Low) = Ip(High) = 175; Ip(low) = lsp(High) = 100; lsp(Low) = 0] was used to categorize inverted image pixels across the entire tumor cross section as negative (>220), weakly positive (175-220), positive (100-175), and strongly positive (0-100) which were then pseudocolored as displayed in figures (“positivity mask”). The percentage of positive pixels (number of weakly positive, positive, or strongly positive pixels divided by total pixels) in the applicable viable tumor area (designated by excluding necrotic volumes identified on H&E images) was then calculated. Scale bars are shown.

#### *In vitro corollary*

HCT116 GFP cells discussed above and MCF7 cells separately purchased from ATCC (not transfected with fluorescent reporter and maintained in DMEM with 10% FBS and 1x penicillin/streptomycin) were used for *in vitro* experiments paralleling the above *in vivo* queries. 450,000 HCT116 cells were seeded in 35 mm dishes and allowed to expand for 3 days in normal culture conditions (DMEM/F12 supplemented with 10% newborn calf serum in standard 5% CO<sub>2</sub> incubators). Media was then changed to DMEM medias as used for U2OS experiments (defined in detail above): low buffer with DMSO (vehicle), low buffer with 1 mM DMOG, high buffer with DMSO, high buffer with 1 mM DMOG, or PIPES/HEPES buffered DMEM pre-adjusted to six different pH values (pH 7.4, 7.0, 6.8, 6.6, 6.5, and 6.3). Plates with highly buffered media continued in 5% CO<sub>2</sub> incubators. All other plates were moved to humidified incubators with atmospheric CO<sub>2</sub>. Protein was harvested for western blots and media pH was assessed at the indicated time points. MCF7 cells were split into 35 mm dishes, allowed to expand for several days until confluent, and then treated with the same media and DMOG conditions as with HCT116 cells with time points as indicated.

#### P493 xenografts

##### *Tumor formation*

P493 cells were cultured in standard RPMI 1640 media with 10% FBS and antibiotics in standard 37 °C humidified incubators in 5% CO<sub>2</sub> as described above. All animals were maintained in accordance with the guidelines of the Institutional Animal Care and Use Committee (IACUC) at The Wistar Institute. Xenografts were formed in 6- to 8-week old athymic female nude mice (Charles River) through subcutaneous flank injection of 20 million P493 cells collected from culture.

The rapamycin-treated mouse received one dose of rapamycin (8 mg/kg) administered intraperitoneally in a vehicle of 5% PEG-400 (Sigma) and 5% Tween 80 (Sigma) (Bitto et al., 2016; Huang et al., 2012) one hour before sacrifice and xenograft harvest.

At study endpoints, mice were sacrificed by cervical dislocation. Tumor volumes were approximated by caliper measurement as  $\text{length} \times \text{width} \times \text{width} \times 0.52$  (where  $\text{width} < \text{length}$ ).

#### *Immunofluorescence and immunohistochemical staining*

Immunofluorescence staining was performed on 5  $\mu\text{m}$  formalin-fixed, paraffin-embedded sections. The sections were deparaffinized in Xylene Substitute (Surgipath) and then iteratively rehydrated with 100%, 95%, and 70% ethanol followed by Millipore water. Antigen retrieval was performed in a digital decloaking chamber (Biocare Medical) using citric acid-based antigen unmasking solution (Vector Laboratories). Sections were blocked with avidin/biotin blocking kit (Vector Laboratories) followed by 4% BSA (Sigma) at room temperature for 30 minutes. Sections were then incubated overnight at 4 °C with rabbit anti-phospho S6 (Ser235/236) (Cell Signaling, Cat#4858) diluted 1:100 in blocking buffer. Sections were then washed three times with 0.1% PBST prior to incubation with Alexa Fluor 488 conjugate anti-rabbit secondary antibody (Invitrogen, A11034) for 45 minutes at room temperature. After three washes, incubation with DAPI (ThermoFisher, D3571) for 5 minutes, and another three washes, sections were mounted with VECTASHIELD (Vector Laboratories).

For immunohistochemistry staining of pS6 and Ki67, sections were prepared as above with the addition of an additional incubation in 1%  $\text{H}_2\text{O}_2$  at room temperature for 15 minutes to block endogenous peroxidase activity prior to proceeding with the above

blocking. Primary antibodies included anti-phospho-S6 as above and anti-Ki67 (Thermo Scientific) diluted 1:100. For dual-target staining, staining was performed on adjacent sections. After overnight incubation and washes as above, sections were incubated for 40 minutes at room temperature with biotinylated goat anti-rabbit secondary antibody (Vector Laboratories) diluted 1:250. Sections were then washed three times, treated for 40 minutes with ABC-HRP (Vector Laboratories), and then washed another three times for 5 minutes each. Colorimetric detection then proceeded with DAB (Vector Laboratories) with diluted Harris Hematoxylin (Fisher Chemical) to counterstain nuclei. Product numbers of reagents in Appendix.

#### *Image acquisition and processing*

Confocal images of pS6 immunofluorescence staining across the entire tumor cross-sectional area were obtained using a Leica TCS SP8 confocal scanning microscope through a semi-automated stitching protocol. Data were analyzed using Nikon microscope image software NIS. Necrotic areas identified via comparison to hematoxylin and eosin stained adjacent slices were excluded from analysis. Tumor edge was demarcated and the percent of pixels positive for pS6 was calculated for the entire viable tumor cross sectional area as well as for concentric regions of interest (shells) of 1 mm width. Positivity threshold was determined by measurement of non-cytoplasmic (background) signal in a representative region.

Images of immunohistochemical staining of pS6 and Ki67 were obtained on a Nikon Eclipse 80i microscope equipped with 2x and 10x objectives using Nikon NIS-Elements Basic Research software or on an Epson Perfection V39 scanner at 2400-4800 dpi resolution. Scale bars as shown.

### *In vitro corollary*

2.1 million cells were resuspended in 7 mL of PIPES/HEPES buffered DMEM media (as above) preadjusted to pH 7.4, 7.0, 6.8, 6.6, 6.5, and 6.3 and flasks were moved to a humidified incubator with atmospheric CO<sub>2</sub>. After 24 hours culture, cells were spun down at 300 RCF for 5 min, washed once with cold PBS, spun down again for 5 min at 4°C, and then lysed in lysis buffer and subjected to western blot analysis as above.

### PANC02 tumors

Formalin-fixed, paraffin-embedded tissue blocks of the murine orthotopic pancreatic tumor model PANC02 were generously provided by Dr. Robert Gillies. Immunohistochemistry staining for carbonic anhydrase IX (Novus Biologicals, 1:500) and phospho-S6 was performed on adjacent 5 µm sections as for P493 immunohistochemistry described above. Product numbers of reagents in Appendix.

Images were then acquired using an Epson Perfection V39 scanner at 4800 dpi resolution. Scale bars are shown.

### **Quantification and Statistical Analysis**

Statistical details of experiments, including the number of biological replicates, are as described in legends and above. Pooled data are presented as the mean plus and minus the standard error of the mean (SEM) or standard deviation (SD) of biological replicates as indicated in legends and calculated by Microsoft Excel or GraphPad Prism. In rare instances of error bars representing variation among technical replicates (Figures S1E, S1K, S7F), this is indicated in legend. For continuous luminometer readings of cells expressing luciferase-based reporters presented as the mean of biological replicates

(e.g. Figure 1J), most error bars have been removed to enhance readability of figures; however, to give a sense of the typical variation among replicates with this technique, SEM error bars have been retained for randomly selected figures (Figures S1G, S1J, S2B, 4I, and S4N). For analysis of the RNA-sequencing timecourses, statistical criteria for designation as circadian and enriched ontology calls are described above. Other tests for statistical significance, including t-tests, ANOVA, and post-hoc tests are described in figure legends. When tests that correct for multiple comparisons are employed, adjusted p-values are presented. Referenced biological replicates in some instances encompass experiments with minor alterations of procedure (e.g. modified drug concentrations, modified timings of exposures and sampling, immunoblot assessment of alternate proteins within the pathway or network, etc.) intended to verify robustness of result and independence from technical artifacts.

### **Data and Software Availability**

Raw and processed RNA-seq data from this study have been submitted to NCBI Gene Expression Omnibus (GEO; <http://www.ncbi.nlm.nih.gov/geo/>) under accession number GSE101988.

## APPENDIX

**Table 1 - Regents and Resources**

REAGENT or RESOURCE	SOURCE	IDENTIFIER
Antibodies		
Rabbit polyclonal anti-HIF1 $\alpha$	Cayman Chemical	Cat#:10006421; RRID:AB_10099184
Mouse monoclonal anti- $\alpha$ -tubulin (clone DM1A)	Calbiochem	Cat#:CP06; RRID:AB_212802
Rabbit polyclonal anti-PER2	Proteintech	Cat#:20359-1-AP; RRID:AB_10733224
Rabbit monoclonal anti-BMAL1 (clone D2L7G)	Cell Signaling	Cat#:14020; RRID:AB_2728705
Rabbit monoclonal anti-CLOCK (clone D45B10)	Cell Signaling	Cat#:5157; RRID:AB_10695411
Rabbit polyclonal anti-CRY2	Epitomics	Cat#:T1225; RRID:AB_10706277
Rabbit monoclonal anti-phospho-mTOR (Ser2448) (clone D9C2)	Cell Signaling	Cat#:5536; RRID:AB_10691552
Rabbit monoclonal anti-mTOR (clone 7C10)	Cell Signaling	Cat#:2983; RRID:AB_2105622
Rabbit monoclonal anti-phospho-p70 S6 Kinase (Thr389) (clone108D2)	Cell Signaling	Cat#:9234; RRID:AB_2269803
Rabbit polyclonal anti-p70 S6 kinase	Cell Signaling	Cat#:9202; RRID:AB_331676
Rabbit monoclonal anti-phospho-S6 ribosomal protein (Ser235/236) (clone D57.2.2E)	Cell Signaling	Cat#:4858; RRID:AB_916156
Rabbit monoclonal anti-phospho-S6 ribosomal protein (Ser235/236) (clone2F9)	Cell Signaling	Cat#:4856; RRID:AB_2181037
Mouse monoclonal anti-S6 ribosomal protein (clone 54D2)	Cell Signaling	Cat#:2317; RRID:AB_2238583
Rabbit monoclonal anti-phospho-4E-BP1 (Thr37/46) (clone 236B4)	Cell Signaling	Cat#:2855; RRID:AB_560835
Rabbit monoclonal anti-4E-BP1 (clone 53H11)	Cell Signaling	Cat#:9644; RRID:AB_2097841

Rabbit polyclonal anti-4EBP2	Cell Signaling	Cat#:2845; RRID:AB_10699019
Rabbit polyclonal anti-phospho-eIF4E (Ser209)	Cell Signaling	Cat#:9741; RRID:AB_331677
Rabbit monoclonal anti-eIF4E (clone C46H6)	Cell Signaling	Cat#:2067; RRID:AB_10828612
Rabbit polyclonal anti-phospho-eEF2 (Thr56)	Cell Signaling	Cat#:2331; RRID:AB_10015204
Rabbit polyclonal anti-eEF2	Cell Signaling	Cat#:2332; RRID:AB_10015206
Rabbit polyclonal anti-Sestrin-2 (clone D1B6)	Cell Signaling	Cat#:8487; RRID:AB_11178663
Rabbit monoclonal anti-DYKDDDDK (FLAG) tag (clone D6W5B)	Cell Signaling	Cat#:14793; RRID:AB_2572291
Rabbit monoclonal anti-Tuberin/TSC2 (clone D93F12)	Cell Signaling	Cat#:4308; RRID:AB_10547134
Rabbit monoclonal anti-phospho-AMPK $\alpha$ (Thr172) (clone 40H9)	Cell Signaling	Cat#:2535; RRID:AB_331250
Rabbit monoclonal anti-AMPK $\alpha$ (clone 23A3)	Cell Signaling	Cat#:2603; RRID:AB_490795
Rabbit monoclonal anti-AMPK $\alpha$ (clone D5A2)	Cell Signaling	Cat#:5831; RRID:AB_10622186
Rabbit monoclonal anti-phospho-c-Raf (Ser338) (clone 56A6)	Cell Signaling	Cat#:9427; RRID:AB_2067317
Mouse monoclonal anti-c-Raf (clone D5X6R)	Cell Signaling	Cat#:12552; RRID:AB_2728706
Rabbit monoclonal anti-phospho-p44/42 MAPK (Erk1/2) (Thr202/Tyr204) (clone D13.14.4E)	Cell Signaling	Cat#:4370; RRID:AB_2315112
Rabbit monoclonal anti-p44/42 MAPK (Erk1/2) (clone 137F5)	Cell Signaling	Cat#:4695; RRID:AB_390779
Rabbit monoclonal anti-phospho-GSK-3 $\beta$ (Ser9) (clone D85E12)	Cell Signaling	Cat#:5558; RRID:AB_10013750
Rabbit polyclonal anti-REDD1	Proteintech	Cat#:10638-1-AP; RRID:AB_2245711
Mouse monoclonal anti-LAMP2 (clone H4B4)	Abcam	Cat#:ab25631; RRID:AB_470709

Rat monoclonal anti-LAMP2 (clone GL2A7)	Abcam	Cat#:ab13524; RRID:AB_2134736
Rabbit monoclonal anti- $\alpha$ -tubulin (clone 11H10) Alexa Fluor 488 conjugate	Cell signaling	Cat#:5063; RRID:AB_10694858
Alexa Fluor 488 phalloidin	Cell signaling	Cat#:8878
Rabbit monoclonal anti-EX2/3	Clippinger et al., 2011.	
Rabbit polyclonal anti-kinesin-1 heavy chain	Santa Cruz	Cat#:28538; RRID:AB_2280915
Rabbit monoclonal anti-RHEB (clone E1G1R)	Cell Signaling	Cat#:13879; RRID:AB_2721022
Rabbit anti phospho-PERK (Thr 982)	Laboratory of Constantinos Koumenis	
Rabbit monoclonal anti-PERK (clone C33E10)	Cell Signaling	Cat#:3192; RRID:AB_2095847
Rabbit monoclonal anti-ATF4 (clone D4B8)	Cell Signaling	Cat#:11815; RRID:AB_2616025
Mouse monoclonal anti-CHOP (clone L63F7)	Cell Signaling	Cat#: 2895; RRID:AB_2089254
Rabbit monoclonal anti-phospho-eIF2 $\alpha$ (Ser51) (clone D9G8)	Cell Signaling	Cat#:3398; RRID:AB_2096481
Rabbit monoclonal anti-eIF2 $\alpha$ (clone D7D3)	Cell Signaling	Cat#:5324; RRID:AB_10692650
Rabbit monoclonal anti-phospho-S6 ribosomal protein (Ser240/244) (clone D68F8)	Cell signaling	Cat#: 5364; RRID:AB_10694233
Brilliant violet 650 rat monoclonal anti-mouse CD8a (clone 53-6.7)	Biolegend	Cat#: 100742; RRID:AB_2563056
Brilliant violet 786 rat monoclonal anti-mouse CD4 (clone RM4-5)	BD Bioscience	Cat#: 563727; RRID:AB_2728707
Mouse monoclonal anti-RHEB (clone 2C11)	Abnova	Cat#: H00006009-M01; RRID:AB_1112097
Sheep polyclonal anti-LAMP1 Alexa Fluor 488 conjugate	R&D Systems	Cat#: IC7985G
Rabbit monoclonal anti-LAMP1 (cloneD2D11)	Cell Signaling	Cat#:9091; RRID:AB_2687579

Rabbit polyclonal anti-phospho-S6 (Ser240/244)	Thermo Fisher Scientific	Cat#: PA1-39503; RRID:AB_10977292
Rabbit polyclonal anti-carbonic anhydrase IX (CAIX)	Abcam	Cat#:ab15086
Rabbit monoclonal anti-TXNIP (cloneEPR14774)	Abcam	Cat#:ab188865
Mouse polyclonal anti-PER2	Sigma	Cat#: HPA060510
Rabbit monoclonal anti-Ki-67 (clone SP6)	Thermo Fisher	Cat#: RM-9106
Rabbit polyclonal anti-carbonic anhydrase IX	Novus Biologicals	Cat#: NB100-417
Alexa Fluor 647 goat anti-rabbit IgG (H+L) cross-adsorbed	Invitrogen	Cat#: A21244; RRID:AB_141663
Alexa Fluor plus 647 goat anti-rabbit IgG (H+L) highly cross-adsorbed	Invitrogen	Cat#:A32733; RRID:AB_2633282
Alexa Fluor 790 goat anti-mouse IgG (H+L) highly cross-adsorbed	Invitrogen	Cat#: A11357; RRID:AB_2534140
Alexa Fluor 680 goat anti-rabbit IgG (H+L) highly cross-adsorbed	Invitrogen	Cat#: A-21109; RRID:AB_2535758
Alexa Fluor 488, goat anti-rabbit IgG (H+L) highly cross-adsorbed	Invitrogen	Cat#: A-11034; RRID:AB_2576217
Alexa Fluor 594 goat anti-mouse IgG (H+L) highly cross-adsorbed	Invitrogen	Cat#: A-11032; RRID:AB_141672
Alexa Fluor Plus 555 goat anti-mouse IgG (H+L) highly cross-adsorbed	Invitrogen	Cat#: A-32727; RRID:AB_2633276
Alexa Fluor 555 goat anti-rat IgG (H+L) cross-adsorbed	Invitrogen	Cat#: A-21434; RRID:AB_141733
Alexa Fluor 488, goat anti-mouse IgG (H+L) cross-adsorbed	Invitrogen	Cat#: A-11001; RRID:AB_2534069
Alexa Fluor 594 goat anti-rabbit IgG (H+L) highly cross-adsorbed	Invitrogen	Cat#: A-11037; RRID:AB_2534095
Biotinylated Goat Anti-Rabbit IgG Antibody	Vector Laboratories	Cat#: BA-1000
Hamster monoclonal anti-CD3 (clone 145-2c11)	In-house hybridoma (Laboratory of Jonathan Powell)	

Hamster monoclonal anti-CD28 (clone 37.51)	In-house hybridoma (Laboratory of Jonathan Powell)	
Mouse monoclonal anti-Hamster IgG1 (clone HIG-632)	BD Biosciences	Cat#: 550637; RRID:AB_393797
Bacterial and Virus Strains		
Human cytomegalovirus (Towne strain variant)	Clippinger et al., 2011.	
Biological Samples		
Formalin-fixed, paraffin-embedded tissue blocks of the murine orthotopic pancreatic tumor model PANC02	Robert Gillies Lab	
Chemicals, Peptides, and Recombinant Proteins		
Beetle luciferin, potassium salt	Promega	E1602;
Dexamethasone	Sigma	D4902; CAS 50-02-2
Dulbecco's MEM (DMEM) high glucose	Corning	MT10-013-CV
DMEM high glucose w/o L-glutamine, phenol red, and sodium bicarbonate (powder)	USBiological	D9812-05
DMEM low glucose w/o L-glutamine, leucine, phenol red, and sodium bicarbonate (powder)	USBiological	D9806-05
DMEM low glucose, w/o amino acids, pyruvic acid, and sodium bicarbonate (powder)	USBiological	D9800-13
DMEM/F12 (Ham)	Gibco	11320-033
RPMI-1640	Corning	10-040
RPMI-1640 without glucose and sodium bicarbonate (powder)	Sigma	R1383
RPMI-1640	Gibco	11875-093
Sodium bicarbonate 7.5% solution	Gibco	25080094
Sodium bicarbonate	Fisher Scientific	S233-3; CAS 144-55-8

HEPES solution	Sigma, Corning	H0887, 25-060-CI; CAS 7365-45-9
HEPES	Sigma	H4034; CAS 7365-45-9
PIPES	Sigma	P1851; CAS 5625-37-6
L-arginine monohydrochloride	Sigma	A6969; CAS 1119-34-2
L-cystine dihydrochloride	Sigma	C6727; CAS 30925-07-6
L-glutamine	Sigma	G3126; CAS 56-85-9
Glycine	Sigma	G8790; CAS 56-40-6
L-histidine	Sigma	H6034; CAS 71-00-1
L-isoleucine	Sigma	I7403; CAS 73-32-5
L-leucine	Sigma	L8912; CAS 61-90-5
L-Lysine monohydrochloride	Sigma	L8662; CAS 657-27-2
L-methionine	Sigma	M5308; CAS 63-68-3
L-phenylalanine	Sigma	P5482; CAS 63-91-2
L-serine	Sigma	S4311; CAS 56-45-1
L-threonine	Sigma	T8441; CAS 72-19-5
L-tryptophan	Sigma	T8941; CAS 73-22-3
L-tyrosine	Sigma	T8566; CAS 60-18-4
L-valine	Sigma	V0513; CAS 72-18-4
Glutamine (solution)	Lonza, Corning	17-605E; 25-005
Pyruvate	Gibco	11360070
D-(+)-glucose powder	Sigma	G7021; CAS 50-99-7
Fetal bovine serum	HyClone, Gemini Bioproducts	SH30910.03
Fetal Bovine Serum, dialyzed	Gibco	26400044
Newborn Calf Serum	HyClone GE Healthcare	SH30118.02
Penicillin-Streptomycin Solution (100x)	Corning	MT30002CI
Penicillin-Streptomycin Solution (100x)	Gibco	15140122

MEM non-essential amino acids solution (100x)	Gibco	11140050
B-27 Supplement (50x), serum free	Gibco	17504044
High-vacuum silicone grease	Dow Corning/Sigma	Z273554
Bovine Serum Albumin	Sigma	A7906
Restore Western blot stripping buffer	Thermo Scientific	21059
2-Mercaptoethanol	Sigma	M3148; CAS 60-24-2
Gentamycin	Quality Biological	120-098-661
G418 sulfate	Corning	MT30-234-CR
Hygromycin B solution	Corning	30-240-CR
Puromycin dihydrochloride	Gibco	A1113803
DMOG (dimethyloxalylglycine)	Sigma	D3695; CAS 89464-63-1
Desferrioxamine mesylate	Calbiochem	252750; CAS 138-14-7
GNE-140	Matt Hall, National Center for Advanced Translational Sciences (NCATS) Chemical Genomics Center, NIH	CAS:1802977-61-2
TRIzol reagent	Invitrogen	15596018
TaqMan Reverse transcription kit	Invitrogen	N8080234
iScript reverse transcription supermix	Bio-Rad	1708841
Valinomycin	Invitrogen	P35379; CAS 2001-95-8
Nigericin, free acid	Invitrogen	P35379; CAS 28380-24-7
Amiloride hydrochloride hydrate	Sigma	A7410; CAS 2016-88-8
$\alpha$ -cyano-4-hydroxycinnamic acid	Sigma	C2020; CAS 28166-41-8
Mammalian protein extraction reagent (M-PER)	Thermo Scientific	PI78501
A-484954	Sigma	SML0861; CAS 142557-61-7

Torin1	Cayman chemical	10997; CAS 222998-36-8
Torin2	Cayman chemical	14185; CAS 1223001-51-1
Rapamycin	Sigma	R0395; CAS 53123-88-9
n-butanol	Sigma	537993; CAS 71-36-3
tert-butanol (t-butanol)	Sigma	B85927; CAS 75-65-0
Anti-FLAG M2 affinity gel	Sigma	A2220
$\beta$ -glycerophosphate disodium salt hydrate	Sigma	G9422; CAS 154804-51-0
Sodium pyrophosphate dibasic	Sigma	71501; CAS 7758-16-9
cOmplete, Mini, EDTA-free Protease Inhibitor Cocktail	Roche	4693159001
Magnesium chloride	Sigma	M8266; CAS 7786-30-3
Cilobrevin D	Calbiochem	250401; CAS
Nocodazole	Cayman chemical	13857; CAS 31430-18-9
Polybrene	Millipore	TR-1003-G
Paraformaldehyde	Electron Microscopy Sciences	19208; CAS 30525-89-4
Methanol free 4% paraformaldehyde	Invitrogen	FB002
10% neutral buffered formalin	Thermo Fisher Scientific	5705
Poly-D-lysine hydrobromide (mol wt 70,000-150,000)	Sigma	P0899; CAS 27964-99-4
Type I collagen, rat tail	Corning	354249
Goat serum	Sigma	G9023
Rabbit serum	Sigma	R9133
DAPI	Invitrogen	D21490; CAS 28718-90-3
Fluoromount-G	SouthernBiotech/Fisher	OB10001

Covergrip coverslip sealant	Biotium	23005
Lipofectamine LTX reagent with PLUS reagent	Invitrogen	15338100
Lipofectamine 3000 transfection reagent	Invitrogen	L3000008
Lipofectamine RNAiMAX transfection reagent	Invitrogen	13778150
ACK lysing buffer	Quality Biological	118-156-101
Recombinant Murine IL-2	Peprtech	212-12
Recombinant <i>SIINFEKL (ovalbumin) peptide</i>	Anaspec	AS-60193
Cycloheximide solution	Sigma	C4859; CAS 66-81-9
Cycloheximide	Sigma	C1988; CAS 66-81-9
Sucrose	Fisher scientific	S25590B; CAS 57-50-1
NaCl, 5M solution	Invitrogen	AM9759; CAS 7647-14-5
Tris-HCl, 1M solution, pH 7.5	Invitrogen	15567-027
MgCl <sub>2</sub> , 1M solution	Invitrogen	AM9530G; CAS 7786-30-3
Heparin sodium salt	Sigma	H3149; CAS 9041-08-1
Triton X-100	Sigma	T8787; CAS 9002-93-1
Guanidine-HCl, 8M solution	Thermo Scientific	24115
Tris-EDTA	Sigma	93302
Sodium acetate, 3M, pH 5.2	Thermo Scientific	R1181
LiCl Solution, pH 7.5	Invitrogen	AM9480
Tween 80	Sigma	P4780
Poly(ethylene glycol), 400	Sigma	91893; CAS 25322-68-3
17 $\beta$ -ESTRADIOL pellet, 0.72 mg, 60-day release	Innovative Research of America	SE-121
Bond dewax solution	Leica	AR9222
Bond TM Epitope Retrieval 2 (ER2) solution	Leica	AR9640
Bond Polymer Refine Red Detection	Leica	DS9390
EZ Prep solution (10x)	Ventana	950-102

RiboCC	Ventana	760-107
Dako antibody diluent	Agilent	S080983-2
DISCOVERY OmniMap anti-Rb HRP (RUO)	Ventana	760-4311
DISCOVERY ChromoMap DAB Kit (RUO)	Ventana	760-159
SUB-X CLEARING AGENT (Xylene substitute)	Leica/Surgipath	3803672
Antigen Unmasking Solution, Citric Acid Based	Vector Laboratories	H-3300
Avidin/Biotin Blocking Kit	Vector Laboratories	SP-2001
DAPI	Thermo Fisher	D3571
VECTASHIELD Antifade Mounting Medium	Vector Laboratories	H-1000
VECTASTAIN Elite ABC HRP Kit (Peroxidase, Standard)	Vector Laboratories	PK-6100
DAB Peroxidase (HRP) Substrate Kit (with Nickel), 3,3'-diaminobenzidine	Vector Laboratories	SK-4100
Harris Modified Method Hematoxylin Stain with Acetic Acid	Fisher Chemical	SH26-500D
Critical Commercial Assays		
RNeasy plus mini kit	Qiagen	74134
DC protein assay kit II	Bio-Rad	5000112
Luciferase assay system	Promega	E1501
TaqMan universal PCR master mix	Thermo Fisher	4304437
Power SYBR™ Green PCR Master Mix	Thermo Fisher	4368708
Illumina TruSeq Stranded mRNA Library Preparation kit	Illumina	RS-122-2101
LysoTracker Deep Red	Invitrogen	L12492
TubulinTracker Green (Oregon Green™ 488 Taxol, Bis-Acetate)	Invitrogen	T34075
Deposited Data		

Raw and processed RNA-sequencing	This study	GEO: GSE101988
Experimental Models: Cell Lines		
Human: U2OS	Laboratory of Roger Greenberg	ATCC HTB-96
Human: U2OS <i>Arntl</i> ::dLUC	Laboratory of John Hogenesch	
Human: U2OS <i>Per2</i> ::dLUC	Laboratory of John Hogenesch	
Human: U2OS <i>PGK1-HRE</i> ::dLUC	This study	
Human: U2OS <i>VEGF-HRE</i> ::dLUC	This study	
Human: U2OS mCherry-SEpHluorin	This study	
Human: U2OS <i>EIF4EBP1</i> <i>-/-</i> (4EBP1 <i>-/-</i> )	This study	
Human: U2OS <i>TSC2</i> <i>-/-</i>	This study	
Human: U2OS PX458 empty vector ("no gRNA") clone #EV1_16	This study	
Human: U2OS PX458 empty vector ("no gRNA") clone #EV2_6	This study	
Human: U2OS RAP2A	This study	
Human: U2OS RaGB99L	This study	
Human: U2OS RHEB <sup>N153T</sup>	This study	
Human: 293T	Laboratory of Celeste Simon	ATCC CRL-3216
Human: 293T Flag-WRD24	This study	
Human: 293T Flag-RAP2A	This study	
Human: 293T SESTRIN TKO	Laboratory of David Sabatini	
Mouse: <i>Tp53</i> <i>-/-</i> MEFs	Laboratory of David Kwiatkowski via laboratory of Celeste Simon	

Mouse: <i>Tp53</i> -/- <i>TSC2</i> -/- MEFs	Laboratory of David Kwiatkowski via laboratory of Celeste Simon	
Human: MDA-MB-231	Laboratory of Donald E. Ayer ( <i>in vitro</i> work)	ATCC HTB-26
Human: MDA-MB-231 DsRed	Ibrahim-Hashim et al., 2017	ATCC HTB-26
Human: MCF7 eGFP	Ibrahim-Hashim et al., 2017	ATCC HTB-22
Human: MCF7	ATCC	ATCC HTB-22
Human: HCT-116 GFP	Estrella et al., 2013	ATCC CCL-247
Mouse: <i>Tsc2</i> <sup>fl/fl</sup> <i>Cd4-Cre</i> ( <i>TSC2</i> -/-) T cells	Laboratory of Jonathan Powell	
Mouse: <i>Tsc2</i> <sup>fl/fl</sup> ( <i>TSC2</i> +/+) T cells	Laboratory of Jonathan Powell	
Mouse: OT-1 (OVA-specific CD8 <sup>+</sup> T cells)	Laboratory of Jonathan Powell	
Experimental Models: Organisms/Strains		
Mouse: <i>TSC2</i> -/-: C57BL/6 <i>Tsc2</i> <sup>fl/fl</sup> <i>Cd4-Cre</i>	Pollizzi et al., 2015	CD4 Cre: JAX: 017336; <i>Tsc2</i> <sup>fl/fl</sup> : Laboratory of Michael Gambello
Mouse: <i>TSC2</i> +/+: C57BL/6 <i>Tsc2</i> <sup>fl/fl</sup>	Pollizzi et al., 2015	<i>Tsc2</i> <sup>fl/fl</sup> : Laboratory of Michael Gambello
Mouse: OT-1 (OVA-specific CD8 <sup>+</sup> T cells): C57BL/6-Tg(TcraTcrb)1100Mjb/J	Pollizzi et al., 2015	JAX: 003831
Mouse: SCID (Fox Chase SCID Beige): SCB17.Cg-PrkdcscidLystbg-J/Crl	Charles River	Charles River: strain code 250
Mouse: nu/nu: <i>Foxn1</i> <sup>nu/nu</sup>	Envigo	Envigo: 069
Oligonucleotides		

For qPCR primers, see Appendix Table 2		
For DsiRNA oligos, See Appendix Table 2		
sgRNA targeting <i>EIF4EBP1</i> : TGAAGAGTCACAGTTTGAGA	GeCKO library; Shalem et al., 2014	CCDS ID: CCDS6100.1
sgRNA targeting <i>TSC2</i> : TCTGCTGAAGGCCATCGTGC	GeCKO library; Shalem et al., 2014	CCDS ID: CCDS10458.1
CleanCap™ β-gal mRNA (capped and poly-A tailed codon optimized beta galactosidase mRNA)	Trilink	L-7608
Recombinant DNA		
pGL4.22	Promega	E6771
HRE-pGL2-TK	Li et al., 2014	N/A
HRE/GFP	Laboratory of Martin Brown and Thomas Foster	Addgene plasmid #46926
pGL4.22-PGK1-HRE::dLUC	This study	N/A
pGL4.22-VEGF-HRE::dLUC	This study	N/A
mCherry-SEpHluorin	Koivusalo et al., 2010	Addgene plasmid #32001
pSpCas9(BB)-2A-GFP (PX458)	Laboratory of Feng Zhang	Addgene plasmid #48138
PX458-sgEIF4EBP1 (sgRNA against <i>EIF4EBP1</i> )	This study	N/A
PX458-sgTSC2 (sgRNA against <i>TSC2</i> )	This study	N/A
Flag-pLJM1-RAP2A	Sancak et al., 2008	Addgene plasmid #19311
Flag-pLJM1-RAGB99L	Sancak et al., 2008	Addgene plasmid #19315
pcDNA3.1+	Invitrogen	V79020
pcDNA3.1+ Flag-RAP2A	This study	N/A
pcDNA3.1+ Flag-RAGB99L	This study	N/A

Flag-pLJM1-WDR24	Laboratory of David Sabatini	Addgene plasmid #46337
LAMP1-mGFP	Laboratory of Esteban Dell-Angelica	Addgene plasmid #34831
LAMP1-mRFP-FLAG	Laboratory of David Sabatini	Addgene plasmid #34611
pcDNA3-FLAG-RHEB-N153T	Laboratory of Fuyuhiko Tamanoi	Addgene plasmid #19997
psPAX2	Laboratory of Didier Trono	Addgene plasmid #12260
pMD2.G	Laboratory of Didier Trono	Addgene plasmid #12259
Software and Algorithms		
LumiCycle Analysis software, v. 2.56	ActiMetrics	<a href="http://actimetrics.com/products/lumicycle/">http://actimetrics.com/products/lumicycle/</a>
R Studio, v. 0.99.491	RStudio	<a href="https://www.rstudio.com/">https://www.rstudio.com/</a>
Spliced Transcripts Alignment to a Reference (STAR) aligner	Dobin et al., 2013.	<a href="https://github.com/alexdobin/STAR">https://github.com/alexdobin/STAR</a>
Cufflinks	Trapnell et al., 2013	<a href="http://cole-trapnell-lab.github.io/cufflinks/">http://cole-trapnell-lab.github.io/cufflinks/</a>
MetaCycle (includes ARSER), v. 1.1.0	Wu et al., 2016.	<a href="https://cran.r-project.org/web/packages/MetaCycle/index.html">https://cran.r-project.org/web/packages/MetaCycle/index.html</a>
ToppFun, version accessed 01/17/18	Chen et al., 2009.	<a href="https://toppgene.cchmc.org/enrichment.jsp">https://toppgene.cchmc.org/enrichment.jsp</a>
VennDiagram package, v. 1.6.17	Hanbo Chen	<a href="https://CRAN.R-project.org/package=VennDiagram">https://CRAN.R-project.org/package=VennDiagram</a>
ggplot2	Hadley Wickham, Winston Chang	<a href="http://ggplot2.org/">http://ggplot2.org/</a>
Image Studio software, version 2.0	LI-COR	<a href="https://www.licor.com/bio/products/software/image_studio_lite/">https://www.licor.com/bio/products/software/image_studio_lite/</a>

SlideBook 6	3i Intelligent Imaging Innovations	
NIS-Elements Basic Research software, v. 4.13	Nikon	
Zeiss ZEN, v2.3	Zeiss	
Fiji (image J2 version)	Schindelin et al., 2012.	<a href="https://fiji.sc/">https://fiji.sc/</a>
Radial Profile plugin for Fiji	Paul Baggethun	<a href="https://imagej.nih.gov/ij/plugins/radial-profile.html">https://imagej.nih.gov/ij/plugins/radial-profile.html</a>
FlowJo	FlowJo	
Prism, v. 7.03	GraphPad	
Excel, 2010	Microsoft	
MetaMorph	Molecular Devices	
Aperio Positive Pixel Count Algorithm, v. 9.0	Leica	
Image-Pro Plus, v. 7.0	Media Cybernetics	
Other		
Polymer oxygen control glove box (hypoxia chamber)	Coy Labs	Custom size
LumiCycle 32	ActiMetrics	N/A
LumiCycle 96	ActiMetrics	N/A
SevenGo pH meter SG2 with InLab 413 SG/2m pH probe	Mettler Toledo	51302522
InLab micro pH probe	Mettler Toledo	51343160

**Table 2 – qPCR primers and DsiRNA oligos**

qPCR primers and DsiRNA oligos		
qPCR primers targeting <i>B2M</i> ; GGCCGAGATGTCTCGCTCCG, TGGAGTACGCTGGATAGCCTCC	Primer-BLAST	
qPCR primer targeting <i>HIF1A</i> ; AAGTTCTTCTGGCTCATATCCC, ACCCATTCTCACCCATCA	IDT	Hs.PT.58.20233486
qPCR primer targeting <i>EPAS1</i> ; CTTTGCGAGCATCCGGTA, AGCCTATGAATTCTACCATGCG	IDT	Hs.PT.58.2273374
qPCR primer targeting <i>PGK1</i> ; AGAACCTCCGCTTTCATGTG, CATTGA CATAGACATCCCCTAGC	IDT	Hs.PT.39a.1406561
qPCR primer targeting <i>VEGF</i> ; GTTCCCGAAACCCTGAGG, GACGTGTAAATGTTCTGCAAA	IDT	Hs.PT.56a.19704989
qPCR primer targeting <i>PDK1</i> ; CAAGAAGCTCCTGAAGACTCTG, CAAGAGTTGCCTGTCAGACTG	IDT	Hs.PT.58.19794808
qPCR primer targeting <i>SLC2A1</i> (GLUT1); GTGCCATACTCATGACCATCG, GGCCACAAAGCCAAAGAT	IDT	Hs.PT.56a.25872862
qPCR primer targeting <i>ARNTL</i> ;	Taqman Gene Expression Assay	Hs00154147_m1
qPCR primer targeting <i>PER2</i> ; GGATGCCCCGCCAGAGTCCAGAT, TGTCCACTTTCGAAGACTGGTCGC	Primer-BLAST	
qPCR primer targeting <i>CRY1</i> ;	Taqman Gene Expression Assay	Hs01565974_m1
qPCR primer targeting <i>NR1D1</i> ; TGGACTCCAACAACAACACAG, GATGGTGGGAAGTAGGTGGG	PrimerBank	ID#300116298c1

qPCR primer targeting <i>NR1D2</i> ; AGTGTCTGTCTGTTGGAATGTC, TCATGGTCTTCATTGCACTTTG	IDT	Hs.PT.51.14785042
qPCR primer targeting <i>RORA</i> ;	Taqman Gene Expression Assay	Hs00536545_m1
qPCR primer targeting <i>BHLHE40</i> (DEC1); CTGTTTCGACATTTCTCCCTGA, CTTGAACCTTACCTTGAAGCATGT	IDT	Hs.PT.58.40041848
qPCR primer targeting <i>EIF4EBP1</i> (4EBP1); GCAATAGCCCAGAAGATAAGCG, CCTTGGTAGTGCTCCACAC	IDT	Hs.PT.58.21283123
qPCR primer targeting <i>EIF4EBP2</i> (4EBP2); CCCAATATCCCAGGAGTCACT, CTTGCAGGAGAGTCAGATGTC	IDT	Hs.PT.58.20248205
qPCR primer targeting <i>TSC2</i>	Taqman Gene Expression Assay	Hs01020387_m1
qPCR primer targeting <i>SESN</i> ; ATGACGAGATACAGCTCTTGC, GGAATGTGCGAGATGAAGAAGAGG	IDT	Hs.PT.58.15586412
qPCR primer targeting <i>SESN2</i> ; CAGGAGCTGGTTACCTC, CCTCACCTACAATACCATCGC	IDT	Hs.PT.58.19441147
qPCR primer targeting <i>SESN3</i> ; AAGTTCAGCTTGCAATTCGTG, AGTGACCTGCTATCCTGAGA	IDT	Hs.PT.58.26332673
qPCR primer targeting <i>KIF5B</i> ; GCTCTTGAGATGTGCTTGACT; TCAACGAGTCTGAAGTGAACC	IDT	Hs.PT.58.25460225
qPCR primer targeting <i>RHEB</i> ; CCACCATATCCAACAATTTGCC, TCTATCTTTCCTCAGACATACTCCA	IDT	Hs.PT.58.26919255
qPCR primer targeting <i>RHEBL1</i> ;  TTCCTTCAACTGCCTGTACC; CTGCATAGCTTCCAAGTCATTG	IDT	Hs.PT.58.1282208

qPCR primer targeting <i>TXNIP</i>	Taqman Gene Expression Assay	Hs01006900_g1
qPCR primer targeting $\beta$ -galactosidase; CCACCAGCGAGATGGACTTC; CTTGTCGCCGATCCACATCT	Primer-BLAST	
DsiRNA targeting <i>HIF1A</i> ; rArCrArArUrArCrCrUrArUrGrUrArGrUrUrGrUrGr GrAAG; rCrUrUrCrCrArCrArArCrUrArCrArUrArGrGrUrAr UrUrGrUrUrU	IDT	HSC.RNAI.N001530. 12.2
DsiRNA targeting <i>EPAS1</i> ( <i>HIF2<math>\alpha</math></i> ) rGrCrArGrUrArCrCrCrArGrArCrGrGrArUrUrCrAr ArUGA; rUrCrArUrUrGrArArArUrCrCrGrUrCrUrGrGrUrA rCrUrGrCrArU	IDT	HSC.RNAI.N001430. 12.2
DsiRNA targeting <i>EIF4EBP1</i> #1; rCrCrUrUrCrCrGrArArUrGrArUrCrArGrCrArGrUrUr CrCAG; rCrUrGrGrArArCrUrGrCrUrGrArUrCrArUrUrCrGrG rArArGrGrArA	IDT	HSC.RNAI.N004095. 12.1
DsiRNA targeting <i>EIF4EBP1</i> #2; rGrGrCrCrUrUrArUrGrArArGrUrGrArUrCrArUrAr CrUGG; rCrCrArGrUrArUrGrArUrCrArCrUrUrUrCrArUrArAr GrGrCrCrUrG (used in western)	IDT	HSC.RNAI.N004095. 12.2
DsiRNA targeting <i>EIF4EBP2</i> ; rGrGrUrCrCrArUrArCrCrArArGrUrArArUrArGrArGr GrCAC; rGrUrGrCrCrUrCrUrArUrUrArCrUrUrGrGrUrArUrG rGrArCrCrUrG	IDT	HSC.RNAI.N004096. 12.1
DsiRNA targeting <i>KIF5B</i> #1; rGrUrArUrCrArArGrCrArGrUrCrArUrUrCrArArUrGr ArCTA; rUrArGrUrCrArUrUrGrArArUrGrArCrUrGrCrUrUrG rArUrArCrCrA	IDT	hs.Ri.KIF5B.13.1
DsiRNA targeting <i>KIF5B</i> #2; rCrCrArArGrArArUrArGrUrGrCrArArGrArUrArUrUr UrUTA; rUrArArArArUrArUrCrUrUrGrCrArCrUrArUrUrCr UrUrGrGrArA	IDT	hs.Ri.KIF5B.13.2

DsiRNA targeting <i>KIF5B</i> #3; rArArGrUrCrArUrUrGrArCrUrGrArArUrArCrCrUrUr CrAAA; rUrUrUrGrArArGrGrUrArUrUrCrArGrUrCrArArUrGr ArCrUrUrGrA	IDT	hs.Ri.KIF5B.13.3
DsiRNA targeting <i>SESN1</i> ; rGrGrArArUrGrUrCrGrArGrArUrGrArArGrArGrAr GrGCA; rUrGrCrCrUrCrUrUrCrUrUrCrArUrCrUrCrGrArCrAr UrUrCrCrUrG1	IDT	HSC.RNAI.N014454. 12.1
DsiRNA targeting <i>SESN2</i> ; rCrCrArCrCrGrArArGrArArUrGrUrArCrArArCrCr UrCTT; rArArGrArGrUrUrGrUrArCrArUrUrCrUrUrCrGrG rGrUrGrGrUrC	IDT	HSC.RNAI.N031459. 12.3
DsiRNA targeting <i>SESN3</i> ; rGrCrUrArArUrArUrCrArGrUrCrArArCrArArUrUrUr CrUGC; rGrCrArGrArArArUrUrGrUrUrGrArCrUrGrArUrArUr UrArGrCrCrU	IDT	HSC.RNAI.N144665. 12.2
DsiRNA targeting <i>TSC2</i> ; rCrCrArArGrUrUrUrArArUrCrArGrUrArCrArUrCrGr UrGTG;  rCrArCrArCrGrArUrGrUrArCrUrGrArUrUrArArArCr UrUrGrGrArG	IDT	HSC.RNAI.N0011143 82.12.2
DsiRNA targeting <i>RHEB</i> ;  rArCrArArArGrUrUrGrArUrCrArCrArGrUrArArArUr GrGAC; rGrUrCrCrArUrUrUrArCrUrGrUrGrArUrCrArArCrUr UrUrGrUrArA	IDT	hs.Ri.RHEB.13.1
DsiRNA targeting <i>RHEBL1</i> #1;  rCrUrUrArCrArGrCrArArGrArUrArGrUrGrArCrUrCr UrUGG; rCrCrArArGrArGrUrCrArCrUrArUrCrUrUrGrCrUrGr UrArArGrUrA	IDT	hs.Ri.RHEBL1.13.1
DsiRNA targeting <i>RHEBL1</i> #2;  rCrCrArArGrUrCrArUrUrGrArGrArGrUrCrUrGr UrArCrCAA; rUrUrGrGrUrArCrArGrArCrUrCrUrCrArArUrGr ArCrUrUrGrGrArA	IDT	hs.Ri.RHEBL1.13.2

DsiRNA targeting <i>RHEBL1</i> #3;  rUrGrArUrGrArArUrUrCrUrGrUrUrArUrArArCr CrUrArUGG; rCrCrArUrArGrGrUrUrArUrArArCrArGrArArUr UrCrArUrCrArArA	IDT	hs.Ri.RHEBL1.13.3
DsiRNA targeting <i>TXNIP</i> #2;  rGrCrArArCrArUrCrCrUrUrCrGrArGrUrUrGrArArUr ArUTC; rGrArArUrArUrUrCrArArCrUrCrGrArArGrGrArUrGr UrUrGrCrArG	IDT	hs.Ri.TXNIP.13.2
Control non-targeting DsiRNA: rCrGrUrUrArArUrCrGrCrGrUrArUrArArUrArCrGrCr GrUrArT; rArUrArCrGrCrGrUrArUrUrArUrArCrGrCrGrArUrUr ArArCrGrArC	IDT	NC1 control duplex

## BIBLIOGRAPHY

- Adamovich, Y., Ladeuix, B., Golik, M., Koeners, M.P., and Asher, G. (2017). Rhythmic Oxygen Levels Reset Circadian Clocks through HIF1 $\alpha$ . *Cell Metab* 25, 93-101.
- Altman, B.J., Hsieh, A.L., Sengupta, A., Krishnanaiah, S.Y., Stine, Z.E., Walton, Z.E., Gouw, A.M., Venkataraman, A., Li, B., Goraksha-Hicks, P., *et al.* (2015). MYC Disrupts the Circadian Clock and Metabolism in Cancer Cells. *Cell Metab* 22, 1009-1019.
- Balgi, A.D., Diering, G.H., Donohue, E., Lam, K.K., Fonseca, B.D., Zimmerman, C., Numata, M., and Roberge, M. (2011). Regulation of mTORC1 signaling by pH. *PLoS One* 6, e21549.
- Balsalobre, A., Brown, S.A., Marcacci, L., Tronche, F., Kellendonk, C., Reichardt, H.M., Schutz, G., and Schibler, U. (2000). Resetting of circadian time in peripheral tissues by glucocorticoid signaling. *Science* 289, 2344-2347.
- Bass, J. (2012). Circadian topology of metabolism. *Nature* 491, 348-356.
- Bass, J., and Takahashi, J.S. (2010). Circadian integration of metabolism and energetics. *Science* 330, 1349-1354.
- Bersten, D.C., Sullivan, A.E., Peet, D.J., and Whitelaw, M.L. (2013). bHLH-PAS proteins in cancer. *Nat Rev Cancer* 13, 827-841.
- Bitto, A., Ito, T.K., Pineda, V.V., LeTexier, N.J., Huang, H.Z., Sutlief, E., Tung, H., Vizzini, N., Chen, B., Smith, K., *et al.* (2016). Transient rapamycin treatment can increase lifespan and healthspan in middle-aged mice. *Elife* 5, e16351.

Bobak, N., Feliciangeli, S., Chen, C.-C., Ben Soussia, I., Bittner, S., Pagnotta, S., Ruck, T., Biel, M., Wahl-Schott, C., Grimm, C., *et al.* (2017). Recombinant tandem of pore-domains in a Weakly Inward rectifying K<sup>+</sup> channel 2 (TWIK2) forms active lysosomal channels. *Scientific Reports* 7, 649.

Bosco, G., Ionadi, A., Panico, S., Faralli, F., Gagliardi, R., Data, P., and Mortola, J.P. (2003). Effects of hypoxia on the circadian patterns in men. *High Alt Med Biol* 4, 305-318.

Boudreau, A., Purkey, H.E., Hitz, A., Robarge, K., Peterson, D., Labadie, S., Kwong, M., Hong, R., Gao, M., Del Nagro, C., *et al.* (2016). Metabolic plasticity underpins innate and acquired resistance to LDHA inhibition. *Nat Chem Biol* 12, 779-786.

Brady, L.K., Wang, H., Radens, C.M., Bi, Y., Radovich, M., Maity, A., Ivan, C., Ivan, M., Barash, Y., and Koumenis, C. (2017). Transcriptome analysis of hypoxic cancer cells uncovers intron retention in EIF2B5 as a mechanism to inhibit translation. *PLoS Biol* 15, e2002623.

Brand, A., Singer, K., Koehl, G.E., Kolitzus, M., Schoenhammer, G., Thiel, A., Matos, C., Bruss, C., Klobuch, S., Peter, K., *et al.* (2016). LDHA-Associated Lactic Acid Production Blunts Tumor Immunosurveillance by T and NK Cells. *Cell Metab* 24, 657-671.

Brugarolas, J.B., Vazquez, F., Reddy, A., Sellers, W.R., and Kaelin, W.G., Jr. (2003). TSC2 regulates VEGF through mTOR-dependent and -independent pathways. *Cancer Cell* 4, 147-158.

Buerger, C., DeVries, B., and Stambolic, V. (2006). Localization of Rheb to the endomembrane is critical for its signaling function. *Biochem Biophys Res Commun* 344, 869-880.

Calcinotto, A., Filipazzi, P., Grioni, M., Iero, M., De Mito, A., Ricupito, A., Cova, A., Canese, R., Jachetti, E., Rossetti, M., *et al.* (2012). Modulation of microenvironment acidity reverses anergy in human and murine tumor-infiltrating T lymphocytes. *Cancer Res* 72, 2746-2756.

Cao, R., Gkogkas, C.G., de Zavalia, N., Blum, I.D., Yanagiya, A., Tsukumo, Y., Xu, H., Lee, C., Storch, K.F., Liu, A.C., *et al.* (2015). Light-regulated translational control of circadian behavior by eIF4E phosphorylation. *Nat Neurosci* 18, 855-862.

Cao, R., Li, A., Cho, H.Y., Lee, B., and Obrietan, K. (2010). Mammalian target of rapamycin signaling modulates photic entrainment of the suprachiasmatic circadian clock. *J Neurosci* 30, 6302-6314.

Cao, R., Robinson, B., Xu, H., Gkogkas, C., Khoutorsky, A., Alain, T., Yanagiya, A., Nevarko, T., Liu, A.C., Amir, S., *et al.* (2013). Translational control of entrainment and synchrony of the suprachiasmatic circadian clock by mTOR/4E-BP1 signaling. *Neuron* 79, 712-724.

Carmeliet, P., and Jain, R.K. (2011). Principles and mechanisms of vessel normalization for cancer and other angiogenic diseases. *Nat Rev Drug Discov* 10, 417-427.

Chambard, J.C., and Pouyssegur, J. (1986). Intracellular pH controls growth factor-induced ribosomal protein S6 phosphorylation and protein synthesis in the G0----G1 transition of fibroblasts. *Exp Cell Res* 164, 282-294.

Chauvet, C., Bois-Joyeux, B., Berra, E., Pouyssegur, J., and Danan, J.L. (2004). The gene encoding human retinoic acid-receptor-related orphan receptor alpha is a target for hypoxia-inducible factor 1. *Biochem J* 384, 79-85.

Chen, J., Bardes, E.E., Aronow, B.J., and Jegga, A.G. (2009). ToppGene Suite for gene list enrichment analysis and candidate gene prioritization. *Nucleic Acids Res* 37, W305-311.

Chen, J.L., Merl, D., Peterson, C.W., Wu, J., Liu, P.Y., Yin, H., Muoio, D.M., Ayer, D.E., West, M., and Chi, J.T. (2010). Lactic acidosis triggers starvation response with paradoxical induction of TXNIP through MondoA. *PLoS Genet* 6, e1001093.

Clippinger, A.J., and Alwine, J.C. (2012). Dynein mediates the localization and activation of mTOR in normal and human cytomegalovirus-infected cells. *Genes Dev* 26, 2015-2026.

Clippinger, A.J., Maguire, T.G., and Alwine, J.C. (2011). Human cytomegalovirus infection maintains mTOR activity and its perinuclear localization during amino acid deprivation. *J Virol* 85, 9369-9376.

Damiola, F., Le Minh, N., Preitner, N., Kornmann, B., Fleury-Olela, F., and Schibler, U. (2000). Restricted feeding uncouples circadian oscillators in peripheral tissues from the central pacemaker in the suprachiasmatic nucleus. *Genes Dev* 14, 2950-2961.

de la Roche, M., Asano, Y., and Griffiths, G.M. (2016). Origins of the cytolytic synapse. *Nat Rev Immunol* 16, 421-432.

Delgoffe, G.M., Pollizzi, K.N., Waickman, A.T., Heikamp, E., Meyers, D.J., Horton, M.R., Xiao, B., Worley, P.F., and Powell, J.D. (2011). The kinase mTOR regulates the differentiation of helper T cells through the selective activation of signaling by mTORC1 and mTORC2. *Nat Immunol* 12, 295-303.

Dibble, C.C., and Manning, B.D. (2013). Signal integration by mTORC1 coordinates nutrient input with biosynthetic output. *Nat Cell Biol* 15, 555-564.

Dibner, C., and Schibler, U. (2015). Circadian timing of metabolism in animal models and humans. *J Intern Med* 277, 513-527.

Dibner, C., Schibler, U., and Albrecht, U. (2010). The mammalian circadian timing system: organization and coordination of central and peripheral clocks. *Annu Rev Physiol* 72, 517-549.

Divakaruni, A.S., Paradyse, A., Ferrick, D.A., Murphy, A.N., and Jastroch, M. (2014). Analysis and interpretation of microplate-based oxygen consumption and pH data. *Methods Enzymol* 547, 309-354.

Dmitriev, A.V., and Mangel, S.C. (2001). Circadian clock regulation of pH in the rabbit retina. *J Neurosci* 21, 2897-2902.

Dobin, A., Davis, C.A., Schlesinger, F., Drenkow, J., Zaleski, C., Jha, S., Batut, P., Chaisson, M., and Gingeras, T.R. (2013). STAR: ultrafast universal RNA-seq aligner. *Bioinformatics* 29, 15-21.

Duvel, K., Yecies, J.L., Menon, S., Raman, P., Lipovsky, A.I., Souza, A.L., Triantafellow, E., Ma, Q., Gorski, R., Cleaver, S., *et al.* (2010). Activation of a metabolic gene regulatory network downstream of mTOR complex 1. *Mol Cell* 39, 171-183.

Eckel-Mahan, K., and Sassone-Corsi, P. (2013). Metabolism and the circadian clock converge. *Physiological reviews* 93, 107-135.

Estrella, V., Chen, T., Lloyd, M., Wojtkowiak, J., Cornnell, H.H., Ibrahim-Hashim, A., Bailey, K., Balagurunathan, Y., Rothberg, J.M., Sloane, B.F., *et al.* (2013). Acidity

generated by the tumor microenvironment drives local invasion. *Cancer Res* 73, 1524-1535.

Feng, D., and Lazar, M.A. (2012). Clocks, metabolism, and the epigenome. *Molecular cell* 47, 158-167.

Fischer, K., Hoffmann, P., Voelkl, S., Meidenbauer, N., Ammer, J., Edinger, M., Gottfried, E., Schwarz, S., Rothe, G., Hoves, S., *et al.* (2007). Inhibitory effect of tumor cell-derived lactic acid on human T cells. *Blood* 109, 3812-3819.

Fonseca, B.D., Diering, G.H., Bidinosti, M.A., Dalal, K., Alain, T., Balgi, A.D., Forestieri, R., Nodwell, M., Rajadurai, C.V., Gunaratnam, C., *et al.* (2012). Structure-activity analysis of niclosamide reveals potential role for cytoplasmic pH in control of mammalian target of rapamycin complex 1 (mTORC1) signaling. *J Biol Chem* 287, 17530-17545.

Fromm-Dornieden, C., von der Heyde, S., Lytovchenko, O., Salinas-Riester, G., Brenig, B., Beissbarth, T., and Baumgartner, B.G. (2012). Novel polysome messages and changes in translational activity appear after induction of adipogenesis in 3T3-L1 cells. *BMC Mol Biol* 13, 9.

Gallagher, F.A., Kettunen, M.I., Day, S.E., Hu, D.E., Ardenkjaer-Larsen, J.H., Zandt, R., Jensen, P.R., Karlsson, M., Golman, K., Lerche, M.H., *et al.* (2008). Magnetic resonance imaging of pH in vivo using hyperpolarized <sup>13</sup>C-labelled bicarbonate. *Nature* 453, 940-943.

Gerson, D.F., Kiefer, H., and Eufe, W. (1982). Intracellular pH of mitogen-stimulated lymphocytes. *Science* 216, 1009-1010.

Gillies, R.J., Raghunand, N., Karczmar, G.S., and Bhujwalla, Z.M. (2002). MRI of the tumor microenvironment. *J Magn Reson Imaging* 16, 430-450.

Gu, X., Orozco, J.M., Saxton, R.A., Condon, K.J., Liu, G.Y., Krawczyk, P.A., Scaria, S.M., Harper, J.W., Gygi, S.P., and Sabatini, D.M. (2017). SAMTOR is an S-adenosylmethionine sensor for the mTORC1 pathway. *Science* 358, 813-818.

Hanker, A.B., Mitin, N., Wilder, R.S., Henske, E.P., Tamanoi, F., Cox, A.D., and Der, C.J. (2010). Differential requirement of CAAX-mediated posttranslational processing for Rheb localization and signaling. *Oncogene* 29, 380-391.

He, H., Yang, Y., Xiang, Z., Yu, L., Chouitar, J., Yu, J., D'Amore, N.R., Li, P., Li, Z., Bowman, D., *et al.* (2016). A Sensitive IHC Method for Monitoring Autophagy-Specific Markers in Human Tumor Xenografts. *J Biomark* 2016, 1274603.

Heuser, J. (1989). Changes in lysosome shape and distribution correlated with changes in cytoplasmic pH. *J Cell Biol* 108, 855-864.

Hogenesch, J.B., Gu, Y.Z., Jain, S., and Bradfield, C.A. (1998). The basic-helix-loop-helix-PAS orphan MOP3 forms transcriptionally active complexes with circadian and hypoxia factors. *Proceedings of the National Academy of Sciences of the United States of America* 95, 5474-5479.

Hogenesch, J.B., Gu, Y.Z., Moran, S.M., Shimomura, K., Radcliffe, L.A., Takahashi, J.S., and Bradfield, C.A. (2000). The basic helix-loop-helix-PAS protein MOP9 is a brain-specific heterodimeric partner of circadian and hypoxia factors. *The Journal of neuroscience : the official journal of the Society for Neuroscience* 20, Rc83.

Huang, J., Nguyen-McCarty, M., Hexner, E.O., Danet-Desnoyers, G., and Klein, P.S. (2012). Maintenance of hematopoietic stem cells through regulation of Wnt and mTOR pathways. *Nat Med* 18, 1778-1785.

Huang, W., Ramsey, K.M., Marcheva, B., and Bass, J. (2011). Circadian rhythms, sleep, and metabolism. *The Journal of clinical investigation* 121, 2133-2141.

Ibrahim-Hashim, A., Robertson-Tessi, M., Enriquez-Navas, P.M., Damaghi, M., Balagurunathan, Y., Wojtkowiak, J.W., Russell, S., Yoonseok, K., Lloyd, M.C., Bui, M.M., *et al.* (2017). Defining Cancer Subpopulations by Adaptive Strategies Rather Than Molecular Properties Provides Novel Insights into Intratumoral Evolution. *Cancer Res* 77, 2242-2254.

Janich, P., Arpat, A.B., Castelo-Szekely, V., Lopes, M., and Gatfield, D. (2015). Ribosome profiling reveals the rhythmic liver translome and circadian clock regulation by upstream open reading frames. *Genome Res* 25, 1848-1859.

Johannes, G., and Sarnow, P. (1998). Cap-independent polysomal association of natural mRNAs encoding c-myc, BiP, and eIF4G conferred by internal ribosome entry sites. *RNA* 4, 1500-1513.

Johnson, D.E., Ostrowski, P., Jaumouille, V., and Grinstein, S. (2016). The position of lysosomes within the cell determines their luminal pH. *J Cell Biol* 212, 677-692.

Jongsma, M.L., Berlin, I., Wijdeven, R.H., Janssen, L., Janssen, G.M., Garstka, M.A., Janssen, H., Mensink, M., van Veelen, P.A., Spaapen, R.M., *et al.* (2016). An ER-Associated Pathway Defines Endosomal Architecture for Controlled Cargo Transport. *Cell* 166, 152-166.

Jouffe, C., Cretenet, G., Symul, L., Martin, E., Atger, F., Naef, F., and Gachon, F. (2013). The circadian clock coordinates ribosome biogenesis. *PLoS Biol* *11*, e1001455.

Keith, B., Johnson, R.S., and Simon, M.C. (2011). HIF1alpha and HIF2alpha: sibling rivalry in hypoxic tumour growth and progression. *Nat Rev Cancer* *12*, 9-22.

Kettner, N.M., Voicu, H., Finegold, M.J., Coarfa, C., Sreekumar, A., Putluri, N., Katchy, C.A., Lee, C., Moore, D.D., and Fu, L. (2016). Circadian Homeostasis of Liver Metabolism Suppresses Hepatocarcinogenesis. *Cancer Cell* *30*, 909-924.

Khalsa, S.B., Ralph, M.R., and Block, G.D. (1991). Does low intracellular pH stop the motion of the Bulla circadian pacemaker? *J Neurosci* *11*, 2672-2679.

Kim, J.W., Tchernyshyov, I., Semenza, G.L., and Dang, C.V. (2006). HIF-1-mediated expression of pyruvate dehydrogenase kinase: a metabolic switch required for cellular adaptation to hypoxia. *Cell Metab* *3*, 177-185.

Kim, Y.C., and Guan, K.L. (2015). mTOR: a pharmacologic target for autophagy regulation. *J Clin Invest* *125*, 25-32.

Koike, N., Yoo, S.H., Huang, H.C., Kumar, V., Lee, C., Kim, T.K., and Takahashi, J.S. (2012). Transcriptional architecture and chromatin landscape of the core circadian clock in mammals. *Science* *338*, 349-354.

Koivusalo, M., Welch, C., Hayashi, H., Scott, C.C., Kim, M., Alexander, T., Touret, N., Hahn, K.M., and Grinstein, S. (2010). Amiloride inhibits macropinocytosis by lowering submembranous pH and preventing Rac1 and Cdc42 signaling. *J Cell Biol* *188*, 547-563.

Kon, N., Hirota, T., Kawamoto, T., Kato, Y., Tsubota, T., and Fukada, Y. (2008).

Activation of TGF-beta/activin signalling resets the circadian clock through rapid induction of Dec1 transcripts. *Nat Cell Biol* 10, 1463-1469.

Koritzinsky, M., Magagnin, M.G., van den Beucken, T., Seigneuric, R., Savelkoul, K., Dostie, J., Pyronnet, S., Kaufman, R.J., Weppler, S.A., Voncken, J.W., *et al.* (2006).

Gene expression during acute and prolonged hypoxia is regulated by distinct mechanisms of translational control. *EMBO J* 25, 1114-1125.

Korolchuk, V.I., Saiki, S., Lichtenberg, M., Siddiqi, F.H., Roberts, E.A., Imarisio, S., Jahreiss, L., Sarkar, S., Futter, M., Menzies, F.M., *et al.* (2011). Lysosomal positioning coordinates cellular nutrient responses. *Nat Cell Biol* 13, 453-460.

Krishnaiah, S.Y., Wu, G., Altman, B.J., Growe, J., Rhoades, S.D., Coldren, F., Venkataraman, A., Olarerin-George, A.O., Francey, L.J., Mukherjee, S., *et al.* (2017). Clock Regulation of Metabolites Reveals Coupling between Transcription and Metabolism. *Cell Metab* 25, 961-974 e964.

Lee, S.K., Achieng, E., Maddox, C., Chen, S.C., Iuvone, P.M., and Fukuhara, C. (2011). Extracellular low pH affects circadian rhythm expression in human primary fibroblasts. *Biochem Biophys Res Commun* 416, 337-342.

Li, B., Qiu, B., Lee, D.S., Walton, Z.E., Ochocki, J.D., Mathew, L.K., Mancuso, A., Gade, T.P., Keith, B., Nissim, I., *et al.* (2014). Fructose-1,6-bisphosphatase opposes renal carcinoma progression. *Nature* 513, 251-255.

Li, X., Rydzewski, N., Hider, A., Zhang, X., Yang, J., Wang, W., Gao, Q., Cheng, X., and Xu, H. (2016). A molecular mechanism to regulate lysosome motility for lysosome positioning and tubulation. *Nat Cell Biol* 18, 404-417.

Lipton, J.O., Yuan, E.D., Boyle, L.M., Ebrahimi-Fakhari, D., Kwiatkowski, E., Nathan, A., Guttler, T., Davis, F., Asara, J.M., and Sahin, M. (2015). The Circadian Protein BMAL1 Regulates Translation in Response to S6K1-Mediated Phosphorylation. *Cell* **161**, 1138-1151.

Majmundar, A.J., Wong, W.J., and Simon, M.C. (2010). Hypoxia-inducible factors and the response to hypoxic stress. *Molecular cell* **40**, 294-309.

Manifava, M., Smith, M., Rotondo, S., Walker, S., Niewczas, I., Zoncu, R., Clark, J., and Ktistakis, N.T. (2016). Dynamics of mTORC1 activation in response to amino acids. *Elife* **5**.

Manzoor, A.A., Schroeder, T., and Dewhirst, M.W. (2008). One-stop-shop tumor imaging: buy hypoxia, get lactate free. *J Clin Invest* **118**, 1616-1619.

Martins, R.M., Alves, R.M., Macedo, S., and Yoshida, N. (2011). Starvation and rapamycin differentially regulate host cell lysosome exocytosis and invasion by *Trypanosoma cruzi* metacyclic forms. *Cell Microbiol* **13**, 943-954.

Matsumoto, C.S., Almeida, L.O., Guimaraes, D.M., Martins, M.D., Papagerakis, P., Papagerakis, S., Leopoldino, A.M., Castilho, R.M., and Squarize, C.H. (2016). PI3K-PTEN dysregulation leads to mTOR-driven upregulation of the core clock gene BMAL1 in normal and malignant epithelial cells. *Oncotarget* **7**, 42393-42407.

McBrian, M.A., Behbahan, I.S., Ferrari, R., Su, T., Huang, T.W., Li, K., Hong, C.S., Christofk, H.R., Vogelauer, M., Seligson, D.B., *et al.* (2013). Histone acetylation regulates intracellular pH. *Mol Cell* **49**, 310-321.

Menon, S., Dibble, C.C., Talbott, G., Hoxhaj, G., Valvezan, A.J., Takahashi, H., Cantley, L.C., and Manning, B.D. (2014). Spatial control of the TSC complex integrates insulin and nutrient regulation of mTORC1 at the lysosome. *Cell* 156, 771-785.

Meyuhas, O. (2015). Ribosomal Protein S6 Phosphorylation: Four Decades of Research. *Int Rev Cell Mol Biol* 320, 41-73.

Miki, N., Ikuta, M., and Matsui, T. (2004). Hypoxia-induced activation of the retinoic acid receptor-related orphan receptor alpha4 gene by an interaction between hypoxia-inducible factor-1 and Sp1. *J Biol Chem* 279, 15025-15031.

Mindell, J.A. (2012). Lysosomal acidification mechanisms. *Annu Rev Physiol* 74, 69-86.

Miyazaki, K., Kawamoto, T., Tanimoto, K., Nishiyama, M., Honda, H., and Kato, Y. (2002). Identification of functional hypoxia response elements in the promoter region of the DEC1 and DEC2 genes. *J Biol Chem* 277, 47014-47021.

Mohan, P.M., Barve, M., Chatterjee, A., and Hosur, R.V. (2006). pH driven conformational dynamics and dimer-to-monomer transition in DLC8. *Protein Sci* 15, 335-342.

Moolenaar, W.H. (1986). Effects of growth factors on intracellular pH regulation. *Annu Rev Physiol* 48, 363-376.

Moorman, N.J., Cristea, I.M., Terhune, S.S., Rout, M.P., Chait, B.T., and Shenk, T. (2008). Human cytomegalovirus protein UL38 inhibits host cell stress responses by antagonizing the tuberous sclerosis protein complex. *Cell Host Microbe* 3, 253-262.

Mortola, J.P., and Seifert, E.L. (2000). Hypoxic depression of circadian rhythms in adult rats. *J Appl Physiol* (1985) 88, 365-368.

- Nakazawa, M.S., Keith, B., and Simon, M.C. (2016). Oxygen availability and metabolic adaptations. *Nat Rev Cancer* 16, 663-673.
- Nandagopal, N., and Roux, P.P. (2015). Regulation of global and specific mRNA translation by the mTOR signaling pathway. *Translation (Austin)* 3, e983402.
- Nishigaki, T., Jose, O., Gonzalez-Cota, A.L., Romero, F., Trevino, C.L., and Darszon, A. (2014). Intracellular pH in sperm physiology. *Biochem Biophys Res Commun* 450, 1149-1158.
- Ohman, H., and Vahlquist, A. (1994). In vivo studies concerning a pH gradient in human stratum corneum and upper epidermis. *Acta Derm Venereol* 74, 375-379.
- Palm, W., Park, Y., Wright, K., Pavlova, N.N., Tuveson, D.A., and Thompson, C.B. (2015). The Utilization of Extracellular Proteins as Nutrients Is Suppressed by mTORC1. *Cell* 162, 259-270.
- Panda, S. (2016). Circadian physiology of metabolism. *Science* 354, 1008-1015.
- Papagiannakopoulos, T., Bauer, M.R., Davidson, S.M., Heimann, M., Subbaraj, L., Bhutkar, A., Bartlebaugh, J., Vander Heiden, M.G., and Jacks, T. (2016). Circadian Rhythm Disruption Promotes Lung Tumorigenesis. *Cell Metab* 24, 324-331.
- Partch, C.L., Green, C.B., and Takahashi, J.S. (2014). Molecular architecture of the mammalian circadian clock. *Trends Cell Biol* 24, 90-99.
- Peek, C.B., Levine, D.C., Cedernaes, J., Taguchi, A., Kobayashi, Y., Tsai, S.J., Bonar, N.A., McNulty, M.R., Ramsey, K.M., and Bass, J. (2017). Circadian Clock Interaction with HIF1 $\alpha$  Mediates Oxygenic Metabolism and Anaerobic Glycolysis in Skeletal Muscle. *Cell Metab* 25, 86-92.

Pelster, B., and Egg, M. (2015). Multiplicity of hypoxia-inducible transcription factors and their connection to the circadian clock in the zebrafish. *Physiol Biochem Zool* 88, 146-157.

Pilon-Thomas, S., Kodumudi, K.N., El-Kenawi, A.E., Russell, S., Weber, A.M., Luddy, K., Damaghi, M., Wojtkowiak, J.W., Mule, J.J., Ibrahim-Hashim, A., *et al.* (2016).

Neutralization of Tumor Acidity Improves Antitumor Responses to Immunotherapy. *Cancer Res* 76, 1381-1390.

Pizarro, A., Hayer, K., Lahens, N.F., and Hogenesch, J.B. (2013). CircaDB: a database of mammalian circadian gene expression profiles. *Nucleic Acids Res* 41, D1009-1013.

Pollizzi, K.N., Patel, C.H., Sun, I.H., Oh, M.H., Waickman, A.T., Wen, J., Delgoffe, G.M., and Powell, J.D. (2015). mTORC1 and mTORC2 selectively regulate CD8(+) T cell differentiation. *J Clin Invest* 125, 2090-2108.

Pollizzi, K.N., Sun, I.H., Patel, C.H., Lo, Y.C., Oh, M.H., Waickman, A.T., Tam, A.J., Blosser, R.L., Wen, J., Delgoffe, G.M., *et al.* (2016). Asymmetric inheritance of mTORC1 kinase activity during division dictates CD8(+) T cell differentiation. *Nat Immunol* 17, 704-711.

Pouyssegur, J., Chambard, J.C., Franchi, A., Paris, S., and Van Obberghen-Schilling, E. (1982). Growth factor activation of an amiloride-sensitive Na<sup>+</sup>/H<sup>+</sup> exchange system in quiescent fibroblasts: coupling to ribosomal protein S6 phosphorylation. *Proc Natl Acad Sci U S A* 79, 3935-3939.

Pouyssegur, J., Franchi, A., L'Allemain, G., and Paris, S. (1985). Cytoplasmic pH, a key determinant of growth factor-induced DNA synthesis in quiescent fibroblasts. *FEBS Lett* 190, 115-119.

Powell, J.D., Pollizzi, K.N., Heikamp, E.B., and Horton, M.R. (2012). Regulation of immune responses by mTOR. *Annu Rev Immunol* 30, 39-68.

Pu, J., Schindler, C., Jia, R., Jarnik, M., Backlund, P., and Bonifacio, J.S. (2015). BORC, a multisubunit complex that regulates lysosome positioning. *Dev Cell* 33, 176-188.

Raghunand, N., He, X., van Sluis, R., Mahoney, B., Baggett, B., Taylor, C.W., Paine-Murrieta, G., Roe, D., Bhujwala, Z.M., and Gillies, R.J. (1999). Enhancement of chemotherapy by manipulation of tumour pH. *British journal of cancer* 80, 1005-1011.

Rainero, E., Howe, Jonathan D., Caswell, Patrick T., Jamieson, Nigel B., Anderson, K., Critchley, David R., Machesky, L., and Norman, Jim C. (2015). Ligand-Occupied Integrin Internalization Links Nutrient Signaling to Invasive Migration. *Cell Reports* 10, 398-413.

Rao, R.R., Li, Q., Odunsi, K., and Shrikant, P.A. (2010). The mTOR kinase determines effector versus memory CD8<sup>+</sup> T cell fate by regulating the expression of transcription factors T-bet and Eomesodermin. *Immunity* 32, 67-78.

Rosbash, M. (2009). The implications of multiple circadian clock origins. *PLoS Biol* 7, e62.

Saci, A., Cantley, L.C., and Carpenter, C.L. (2011). Rac1 regulates the activity of mTORC1 and mTORC2 and controls cellular size. *Mol Cell* 42, 50-61.

Saito, K., Araki, Y., Kontani, K., Nishina, H., and Katada, T. (2005). Novel role of the small GTPase Rheb: its implication in endocytic pathway independent of the activation of mammalian target of rapamycin. *J Biochem* 137, 423-430.

- Sancak, Y., Bar-Peled, L., Zoncu, R., Markhard, A.L., Nada, S., and Sabatini, D.M. (2010). Ragulator-Rag complex targets mTORC1 to the lysosomal surface and is necessary for its activation by amino acids. *Cell* 141, 290-303.
- Sancak, Y., Peterson, T.R., Shaul, Y.D., Lindquist, R.A., Thoreen, C.C., Bar-Peled, L., and Sabatini, D.M. (2008). The Rag GTPases bind raptor and mediate amino acid signaling to mTORC1. *Science* 320, 1496-1501.
- Sattler, U.G., Walenta, S., and Mueller-Klieser, W. (2007). A bioluminescence technique for quantitative and structure-associated imaging of pyruvate. *Lab Invest* 87, 84-92.
- Saxton, R.A., Knockenhauer, K.E., Wolfson, R.L., Chantranupong, L., Pacold, M.E., Wang, T., Schwartz, T.U., and Sabatini, D.M. (2016). Structural basis for leucine sensing by the Sestrin2-mTORC1 pathway. *Science* 351, 53-58.
- Saxton, R.A., and Sabatini, D.M. (2017). mTOR Signaling in Growth, Metabolism, and Disease. *Cell* 168, 960-976.
- Schindelin, J., Arganda-Carreras, I., Frise, E., Kaynig, V., Longair, M., Pietzsch, T., Preibisch, S., Rueden, C., Saalfeld, S., Schmid, B., *et al.* (2012). Fiji: an open-source platform for biological-image analysis. *Nat Methods* 9, 676-682.
- Schofield, C.J., and Ratcliffe, P.J. (2004). Oxygen sensing by HIF hydroxylases. *Nat Rev Mol Cell Biol* 5, 343-354.
- Semenza, G.L. (2007). Hypoxia-inducible factor 1 (HIF-1) pathway. *Science's STKE : signal transduction knowledge environment* 2007, cm8.
- Semenza, G.L. (2013). HIF-1 mediates metabolic responses to intratumoral hypoxia and oncogenic mutations. *J Clin Invest* 123, 3664-3671.

Shalem, O., Sanjana, N.E., Hartenian, E., Shi, X., Scott, D.A., Mikkelsen, T.S., Heckl, D., Ebert, B.L., Root, D.E., Doench, J.G., *et al.* (2014). Genome-scale CRISPR-Cas9 knockout screening in human cells. *Science* **343**, 84-87.

Shostak, A. (2017). Circadian Clock, Cell Division, and Cancer: From Molecules to Organism. *Int J Mol Sci* **18**.

Sonenberg, N., and Hinnebusch, A.G. (2009). Regulation of translation initiation in eukaryotes: mechanisms and biological targets. *Cell* **136**, 731-745.

Song C.W., G.R., Park H.J. (2006). Influence of Tumor pH on Therapeutic Response. In *Cancer Drug Discovery and Development: Cancer Drug Resistance* T. B.A., ed. (Totowa, NJ: Humana Press).

Takahashi, J.S. (2017). Transcriptional architecture of the mammalian circadian clock. *Nat Rev Genet* **18**, 164-179.

Takahata, S., Sogawa, K., Kobayashi, A., Ema, M., Mimura, J., Ozaki, N., and Fujii-Kuriyama, Y. (1998). Transcriptionally active heterodimer formation of an Arnt-like PAS protein, Arnt3, with HIF-1a, HLF, and clock. *Biochem Biophys Res Commun* **248**, 789-794.

Thoreen, C.C., Chantranupong, L., Keys, H.R., Wang, T., Gray, N.S., and Sabatini, D.M. (2012). A unifying model for mTORC1-mediated regulation of mRNA translation. *Nature* **485**, 109-113.

Toschi, A., Lee, E., Xu, L., Garcia, A., Gadir, N., and Foster, D.A. (2009). Regulation of mTORC1 and mTORC2 complex assembly by phosphatidic acid: competition with rapamycin. *Mol Cell Biol* **29**, 1411-1420.

Trapnell, C., Hendrickson, D.G., Sauvageau, M., Goff, L., Rinn, J.L., and Pachter, L. (2013). Differential analysis of gene regulation at transcript resolution with RNA-seq. *Nat Biotechnol* **31**, 46-53.

Urano, J., Comiso, M.J., Guo, L., Aspuria, P.J., Deniskin, R., Tabancay, A.P., Jr., Kato-Stankiewicz, J., and Tamanoi, F. (2005). Identification of novel single amino acid changes that result in hyperactivation of the unique GTPase, Rheb, in fission yeast. *Mol Microbiol* **58**, 1074-1086.

Verhey, K.J., Lizotte, D.L., Abramson, T., Barenboim, L., Schnapp, B.J., and Rapoport, T.A. (1998). Light chain-dependent regulation of Kinesin's interaction with microtubules. *J Cell Biol* **143**, 1053-1066.

Walton, Z.E., Altman, B.J., Brooks, R.C., and Dang, C.V. (2018a). Circadian Clock's Cancer Connections. *Annual Review of Cancer Biology* **2**, 133-153.

Walton, Z.E., Patel, C.H., Brooks, R.C., Yu, Y., Ibrahim-Hashim, A., Riddle, M., Porcu, A., Jiang, T., Ecker, B.L., Tameire, F., *et al.* (2018b). Acid Suspends the Circadian Clock in Hypoxia through Inhibition of mTOR. *Cell* **174**, 72-87 e32.

Wang, A., Carraro-Lacroix, L.R., Owen, C., Gao, B., Corey, P.N., Tyrrell, P., Brumell, J.H., and Voronov, I. (2017). Activity-independent targeting of mTOR to lysosomes in primary osteoclasts. *Sci Rep* **7**, 3005.

Wang, S., Tsun, Z.Y., Wolfson, R.L., Shen, K., Wyant, G.A., Plovanich, M.E., Yuan, E.D., Jones, T.D., Chantranupong, L., Comb, W., *et al.* (2015). Metabolism. Lysosomal amino acid transporter SLC38A9 signals arginine sufficiency to mTORC1. *Science* **347**, 188-194.

Welsh, D.K., Imaizumi, T., and Kay, S.A. (2005). Real-time reporting of circadian-regulated gene expression by luciferase imaging in plants and mammalian cells. *Methods Enzymol* 393, 269-288.

Welsh, D.K., Yoo, S.H., Liu, A.C., Takahashi, J.S., and Kay, S.A. (2004). Bioluminescence imaging of individual fibroblasts reveals persistent, independently phased circadian rhythms of clock gene expression. *Curr Biol* 14, 2289-2295.

Woelfle, M.A., Ouyang, Y., Phanvijhitsiri, K., and Johnson, C.H. (2004). The adaptive value of circadian clocks: an experimental assessment in cyanobacteria. *Curr Biol* 14, 1481-1486.

Wolfson, R.L., Chantranupong, L., Saxton, R.A., Shen, K., Scaria, S.M., Cantor, J.R., and Sabatini, D.M. (2016). Sestrin2 is a leucine sensor for the mTORC1 pathway. *Science* 351, 43-48.

Wolfson, R.L., Chantranupong, L., Wyant, G.A., Gu, X., Orozco, J.M., Shen, K., Condon, K.J., Petri, S., Kedir, J., Scaria, S.M., *et al.* (2017). KICSTOR recruits GATOR1 to the lysosome and is necessary for nutrients to regulate mTORC1. *Nature* 543, 438-442.

Wolfson, R.L., and Sabatini, D.M. (2017). The Dawn of the Age of Amino Acid Sensors for the mTORC1 Pathway. *Cell Metab* 26, 301-309.

Wouters, B.G., van den Beucken, T., Magagnin, M.G., Koritzinsky, M., Fels, D., and Koumenis, C. (2005). Control of the hypoxic response through regulation of mRNA translation. *Semin Cell Dev Biol* 16, 487-501.

- Wu, G., Anafi, R.C., Hughes, M.E., Kornacker, K., and Hogenesch, J.B. (2016). MetaCycle: an integrated R package to evaluate periodicity in large scale data. *Bioinformatics* 32, 3351-3353.
- Wu, Y., Tang, D., Liu, N., Xiong, W., Huang, H., Li, Y., Ma, Z., Zhao, H., Chen, P., Qi, X., *et al.* (2017). Reciprocal Regulation between the Circadian Clock and Hypoxia Signaling at the Genome Level in Mammals. *Cell Metab* 25, 73-85.
- Xie, H., and Simon, M.C. (2017). Oxygen availability and metabolic reprogramming in cancer. *J Biol Chem* 292, 16825-16832.
- Xie, J., Mikolajek, H., Pigott, C.R., Hooper, K.J., Mellows, T., Moore, C.E., Mohammed, H., Werner, J.M., Thomas, G.J., and Proud, C.G. (2015). Molecular Mechanism for the Control of Eukaryotic Elongation Factor 2 Kinase by pH: Role in Cancer Cell Survival. *Mol Cell Biol* 35, 1805-1824.
- Xu, Y., Ma, P., Shah, P., Rokas, A., Liu, Y., and Johnson, C.H. (2013). Non-optimal codon usage is a mechanism to achieve circadian clock conditionality. *Nature* 495, 116-120.
- Yamazaki, S., and Takahashi, J.S. (2005). Real-time luminescence reporting of circadian gene expression in mammals. *Methods Enzymol* 393, 288-301.
- Yang, R., and Su, Z. (2010). Analyzing circadian expression data by harmonic regression based on autoregressive spectral estimation. *Bioinformatics* 26, i168-174.
- Zaganjor, E., Weil, L.M., Gonzales, J.X., Minna, J.D., and Cobb, M.H. (2014). Ras transformation uncouples the kinesin-coordinated cellular nutrient response. *Proc Natl Acad Sci U S A* 111, 10568-10573.

Zhang, E.E., Liu, A.C., Hirota, T., Miraglia, L.J., Welch, G., Pongsawakul, P.Y., Liu, X., Atwood, A., Huss, J.W., 3rd, Janes, J., *et al.* (2009). A genome-wide RNAi screen for modifiers of the circadian clock in human cells. *Cell* 139, 199-210.

Zhang, H., Cicchetti, G., Onda, H., Koon, H.B., Asrican, K., Bajraszewski, N., Vazquez, F., Carpenter, C.L., and Kwiatkowski, D.J. (2003). Loss of Tsc1/Tsc2 activates mTOR and disrupts PI3K-Akt signaling through downregulation of PDGFR. *J Clin Invest* 112, 1223-1233.

Zhang, R., Lahens, N.F., Ballance, H.I., Hughes, M.E., and Hogenesch, J.B. (2014). A circadian gene expression atlas in mammals: implications for biology and medicine. *Proc Natl Acad Sci U S A* 111, 16219-16224.

Zheng, X., and Sehgal, A. (2010). AKT and TOR signaling set the pace of the circadian pacemaker. *Curr Biol* 20, 1203-1208.

Zoncu, R., Bar-Peled, L., Efeyan, A., Wang, S., Sancak, Y., and Sabatini, D.M. (2011). mTORC1 senses lysosomal amino acids through an inside-out mechanism that requires the vacuolar H(+)-ATPase. *Science* 334, 678-683.